



Manufacturing and characterization of flax fiber reinforced thermoset composites

Anurag Pisupati

► To cite this version:

Anurag Pisupati. Manufacturing and characterization of flax fiber reinforced thermoset composites. Mechanics of materials [physics.class-ph]. Ecole nationale supérieure Mines-Télécom Lille Douai, 2019. English. NNT : 2019MTLD0014 . tel-03030243

HAL Id: tel-03030243

<https://theses.hal.science/tel-03030243>

Submitted on 30 Nov 2020

HAL is a multi-disciplinary open access archive for the deposit and dissemination of scientific research documents, whether they are published or not. The documents may come from teaching and research institutions in France or abroad, or from public or private research centers.

L'archive ouverte pluridisciplinaire **HAL**, est destinée au dépôt et à la diffusion de documents scientifiques de niveau recherche, publiés ou non, émanant des établissements d'enseignement et de recherche français ou étrangers, des laboratoires publics ou privés.



THÈSE

présentée en vue d'obtenir le grade de

DOCTEUR

en

Mécanique des solides, des matériaux, des structures et des surfaces

par

Anurag PISUPATI

DOCTORAT DE L'UNIVERSITÉ DE LILLE DELIVRÉ PAR IMT LILLE DOUAI

MANUFACTURING AND CHARACTERIZATION OF FLAX FIBER REINFORCED THERMOSET COMPOSITES

Soutenance le 29 Novembre 2019 devant le jury d'examen

President	Prof. Frédéric JACQUEMIN	Université de Nantes
Rapporteur	Prof. Pierre OUAGNE	ENI Tarbes
Rapporteur	Dr. HdR. Alain BOURMAUD	Université Bretagne Sud
Examineur	Dr. HdR. Peter DAVIES	IFREMER
Directeur	Prof. Chung Hae PARK	IMT Lille Douai
Encadrant	Dr. Mylène LAGARDÈRE	IMT Lille Douai
Membre Invité	Dr. Leïla BONNAUD	MateriaNova

Laboratoire d'accueil

Département Technologie des Polymères et Composites & Ingénierie Mécanique de IMT Lille Douai

Ecole Doctorale SMRE 104 (U. Lille, U. Artois, ULCO, UPHF, Centrale Lille, Chimie Lille, IMT Lille Douai)

When ideas fail, words come in very handy.

Johann Wolfgang von Goethe

Acknowledgements

Wow, the past three years were heavy, adventurous, and painful. And yet, here I am, standing under a temporary spotlight, looking at this manuscript which has faced one hundred revisions and has witnessed my dark side. As this manuscript will only be read of a handful of people (experts) and it will slowly be driven into the world of archives, I would like to grab that short moment to steal the limelight and thank all who made this work possible. So, let me start by thanking some important people who were part of my struggle or were present during my struggle in the past three years and also 26 years. [Drum-roll please!]

First, my thesis directors, Prof. Chung Hae Park, and Dr. Mylène Lagardère. Thank you both for your constant constructive criticism of my work. It did help me become better at what I was. It was a great opportunity to work along with you. You were always there with constant support, comments, and compliments. Dr.Lagardere, thank you for those discussions and brainstorming sessions, which were supposed to be only for 5 minutes but ended up much longer. I don't think this thesis would've made it through without that support.

Prof. Krawczak, thank you for welcoming into your lab. I would also like to thank the INTERREG program and project BIOCOMPAL, for funding this work. I would like to thank the project members of BIOCOMPAL, Leila Bonnaud, Frederik Goethlas, Lies Willaert, Baptiste Herlin, who sat through my presentations and listened to me patiently. I learned many interesting things from our meeting in a short period. I hope one day, I get a chance to collaborate with you again.

My deepest gratitude to my jury panel; Prof. Ouagne, Prof. Jacquemin, Dr. Davies, Dr. Bourmaud, and Dr. Bonnaud for taking their time off to read this manuscript and showing interest in this work.

I would like to thank my comrades, both doctors and non-doctors. First of all, Yang, Claire, and Pierre. Thank you for all those happy moments that we shared together. Dmytro and Benoit, thank you for your help in the coding part. Even with our least amount of interaction, I have learned a lot from you both and I hope one day we can work together. Keerthi, I will look forward to our collaborations. Amulya and Prashanth,

thank you for improving my knowledge on polymers. Aniket, thank you for your evening parties and helping me in mastering the upper cut. And finally, Christophe, "thumbs up" to you!

I would also like to thank Jean Pierre and Pierre for helping me with mechanical tests and Xavier, for continuous "mockery" and also for helping me in the preparation of molds and fabrics. Patrice or I should rather say "the magician", thanks for helping me out during the time of crisis. Ayadi, it was a great experience working along with you. I should have taken your motto "Publish or Perish" more seriously. Dominique, a huge thank you for answering all my questions regarding french administrative procedures and also french language itself. Mme Delsert, thank you for patiently waiting for me to finish my french sentences and taking the time to answer them.

Also also, this couldn't have been done without the support I got from my parents, family and friends, especially, Ildar, Sherley, and Tshering. You were always there when needed, just a message away, with all the cheering. And finally, the most important things: Coffee, YouTube, Netflix. You made sure that the stress mounted up till it burst my head into a thousand pieces. Without you, I definitely would have done better, but who knew that I would be learning many things from you.

Contents

Acknowledgements	I
List of Figures	VI
List of Tables	1
1 Introduction	2
1.1 Motivation	2
1.1.1 Project BIOCOMPAL	3
1.2 Subjects	3
1.3 Organisation of dissertation	4
2 Flax fibers and their composites	6
2.1 Flax fibers	6
2.1.1 Morphology and constituents	7
2.1.2 Characteristics of flax fibers	7
2.2 Matrix	10
2.3 Manufacturing process	13
2.3.1 Liquid composite moulding	13
2.4 Void formation in composite materials	17
2.5 Void characterization techniques	19
2.6 Flax fiber composites	21
2.7 Conclusion	25
3 Tensile characterization of flax fibers	27
3.1 Introduction	27
3.2 Materials	31
3.3 Manufacturing of UD composites	31
3.4 Characterization	32
3.4.1 Differential Scanning Calorimetry analysis	32
3.4.2 Laminate quality assessment	33

3.4.3	Tensile tests	34
3.4.4	Back-calculation of the tensile properties of fibers	34
3.5	Effect of curing temperature on physicochemical properties	35
3.6	Qualitative and quantitative assessment of residual voids	37
3.7	Variation of tensile properties of composites with cure cycle	40
3.8	Conclusion	47
4	Wettability characterization of flax fibers	48
4.1	Background	48
4.1.1	Mathematical modelling	48
4.2	Model development for capillary rise	56
4.3	Experimental Setup	58
4.3.1	In-house experimental setup	58
4.3.2	Tensiometer	58
4.4	Experimental results	60
4.4.1	Validation of experimental set-up	60
4.4.2	Capillary rise results for glass and flax fibers	61
4.4.3	Identification of model constants	65
4.5	Validation of proposed model	67
4.6	Conclusion	70
5	Influence of process parameters on composite quality	71
5.1	Tow Permeability	72
5.1.1	Methodology	74
5.1.2	RVE generation	75
5.1.3	Validation of RVE size	75
5.1.4	Inter fiber distances	77
5.1.5	Numerical results and experimental validation	78
5.2	Void formation in flax fiber preforms	85
5.2.1	Experimental procedure	85
5.2.2	Modeling of void formation in flax fiber preforms	87
5.3	Results	90
5.3.1	Permeability of flax fiber preforms	90
5.3.2	Effect of local variability on void formation	92
5.3.3	Model comparison	94
5.4	Conclusions	100

6	In-service behaviour of flax fiber composites	101
6.1	Introduction	101
6.2	Kinetics of diffusion	102
6.2.1	Fick's law of diffusion	103
6.3	Manufacturing of composite specimens	105
6.4	Hygrothermal aging	105
6.5	Mechanical tests	108
6.6	Water absorption of pure resin samples	109
6.7	Influence of operating temperature	114
6.8	Conclusions	117
7	Conclusions and Perspectives	118
	Bibliography	i

List of Figures

2.1	Illustration of micro structure of flax fiber	7
2.2	Illustration of irregular cross-section of natural fiber	9
2.3	Stress strain curve of an elementary flax fiber	9
2.4	Dispersed values of Young's modulus of flax fibers	9
2.5	Surface morphology of flax fibers	11
2.6	Residual porosity map of a phenolic resin	14
2.7	General representation of variation of void content with modified capillary number	19
2.8	Image processing steps for micrographs of a carbon/epoxy composite [75] .	21
2.9	Scan images of a Carbon/Epoxy fabric specimen: (a) planar section; (b) thickness section; and (c) thickness section with detected voids	21
2.10	Schematic of different types of porosities in natural fiber composites	23
3.1	Flow chart depicting the production chain of flax fiber	28
3.2	Schematic of a liquid drop wetting a solid substrate with	29
3.3	Schematic of manufacturing steps	32
3.4	Isothermal DSC measurements: heat flow evolution of resin for each cycle .	35
3.5	Time dependent evolution of degree of cure	36
3.6	Micro structure of UD composites	39
3.7	Stress-strain curves of UD composite samples	41
3.8	Tensile modulus of UD composites and neat matrix	42
3.9	Tensile strength of UD composites and neat matrix	43
3.10	SEM images of fractured surfaces of composite samples	44
3.11	Back calculated tensile modulus of flax fibers	45
3.12	Back calculated tensile strength of flax fibers	46
3.13	Comparison of composite strength and back-calculated fiber strength be- tween literature and this work	46
4.1	Schematic representing surface energies and contact angle	49
4.2	Representation of contact angle	50

4.3	Observing contact angles using drop shape method on (A) Untreated Kraft fibers (B) Treated Kraft fibers	50
4.4	Meniscus on single fiber	51
4.5	Illustration of advancing, static and receding contact angle measurements with Tensiometer	52
4.6	Schematic of the capillary wicking mechanism in swelling fibrous medium .	53
4.7	Wicking height with different values of b	55
4.8	In-house experimental setup for capillary wicking	59
4.9	Sample setup for capillary wicking test	59
4.10	Repeatability of capillary experiments with 50mm capillary tube	61
4.11	Repeatability of capillary rise experiments with 100mm capillary tube . .	62
4.12	Capillary rise tests for glass and flax fibers at $V_f = 40\%$ exhibiting different zones	62
4.13	Capillary rise in flax flax fibers with n-hexane: complete duration (top) and initial stage (below)	63
4.14	Capillary rise in flax fibers with water: 30% V_f (top), 35% V_f (middle) & 40% V_f (bottom)	64
4.15	Capillary rise of flax fibers with water as test liquid (Experiment time: 14000s)	65
4.16	K/R_h determination using n-hexane and flax fibers	66
4.17	Comparison between proposed model and experimental results in the initial viscous stage	67
4.18	Evolution of K/R_h ratio with time for different fiber volume fractions . . .	68
4.19	Parametric analysis of capillary wicking model with different fiber swell and liquid absorption ratios	69
5.1	Evolution of RVE in case of 40% fiber volume fraction	75
5.2	Illustration of a square domain used for numerical simulations	76
5.3	Comparison of different sizes of RVE at $V_f=40\%$	77
5.4	Inter fiber distances (μm) in RVEs with constant fiber diameter	79
5.5	Inter fiber distances(μm) in RVEs with irregular fiber diameters	80
5.6	Permeability versus Fiber volume fraction: numerical results	81
5.7	Distribution of fiber diameter in a RVE with 30% V_f	82
5.8	Schematic of permeability bench	83
5.9	Variation of areal weight of UD flax tape	84
5.10	Comparison between experimental and numerical results for transverse permeability of UD flax tow	85

5.11 Permeability prediction with different analytical models with different fiber radii	86
5.12 Schematic of specimen extraction points from manufactured plate	87
5.13 Applied boundary conditions on the numerical model	88
5.14 Saturated permeability vs fiber volume fraction: experimental results and model	91
5.15 Ratio of unsaturated permeability to saturated permeability vs Fiber volume fraction	91
5.16 Variability of void content with tow fill time	92
5.17 Contour plot of a random flax fiber preform with mean $V_f = 42\%$	93
5.18 Influence of variation in local porosities on fill time	94
5.19 Effect of local variations in porosity of flax fiber preform on void formation	95
5.20 Comparison between expected and experimental void content	96
5.21 Tow voids near the inlet of the plate manufactured with 2 bar injection pressure	97
5.22 Tow voids near the inlet of the plate manufactured with 1.5 bar injection pressure	97
5.23 Channel voids observed at the central section of plate manufactured with 1.5 bar injection pressure	98
5.24 Channel and tow voids observed at the central section of plate manufactured with 1 bar injection pressure in weft direction	98
5.25 Channel voids observed at the central section of plate manufactured with 1bar injection pressure	99
5.26 Large voids near the vent	99
5.27 Voids near the inlet	100
6.1 Typical diffusion behaviours of non fickian weight gain absorption	104
6.2 Manufacturing cycle for two composites: flax/epoxy and flax/benzaoxazine	106
6.3 Aging chamber	107
6.4 Imposed hygrothermal cycle on composite coupons	107
6.5 Experimental set up for high temperature tests	108
6.6 Moisture uptake for epoxy and benzaoxazine resin blocks	109
6.7 Evolution of thickness of resin blocks with time	110
6.8 Moisture absorption of composite specimens	111
6.9 Evolution of flexural modulus of flax/epoxy composites during aging	112
6.10 Evolution of flexural strength of flax/epoxy composites during aging	113
6.11 Schematic of effects of water absorpction on natural fiber-matrix interface .	113
6.12 Normalized flexural properties of flax/benzaoxazine composites during aging	114

6.13	Micrographs of flax/benzaoxazine interface	115
6.14	Force displacement curves of flax/epoxy composites at different temperatures	116
6.15	Force-displacement curves of flax/benzaoxazine composites at different tem- peratures	116
6.16	Flexural strength of composites at different operating temperatures	117

List of Tables

2.1	Chemical composition of flax fibers	8
2.2	Tensile properties of elementary flax fibers	10
2.3	Advantages and disadvantages of thermoset and thermoplastic matrices for composite applications	12
2.4	Comparision between Epoxy and Benzaoxazine resin	13
2.5	Process induced porosity content in flax fiber composites	24
3.1	Isothermal cure parameters	32
3.2	Glass transition temperatures of neat epoxy and composites	37
3.3	Fiber mass, fiber volume fraction and residual void content of composite plates	38
3.4	ANOVA result for tensile properties of UD composites and matrix	45
4.1	Properties of test liquids	60
4.2	Capillary rise results for flax fibers with n-hexane at different fiber volume fractions	64
4.3	Capillary rise results for flax fibers with water at different fiber volume fractions	65
4.4	Coefficients of K/R_h empirical model	66
4.5	Estimated contact angle for different V_f	67
4.6	Values of fiber swell ratio and maximum liquid absorption ratio used for parametric study	68
4.7	Maximum fiber swell ratio and corresponding fiber volume fraction ob- tained from experimental data	70
5.1	Model constants identified using curve fitting	81
5.2	Model constants for sink terms	89
5.3	Preform properties used for void formation and compaction modeling	96
6.1	Inter laminar shear strengths of composites at different operating temper- atures	117

Chapter 1

Introduction

1.1 Motivation

The pollution caused by petroleum resources and our over-dependency on them raised several issues of preservation of the environment calling for eco-friendly materials and methods. In these dire straits, COP 21 and resolution by EU on end-of-life vehicle directive stood as an eye-opener event to the world. COP 21 brought 192 countries to agree and work on the single-point agenda to reduce the CO₂ emissions to limit global warming and its damage. EU made new stringent rules on recycling and re-use of automobile components by 85% in weight. Given the scenario, the use of synthetic fiber-reinforced composites in automobiles decreases the ease of recycling as it requires relatively high energy. Moreover, the polymer matrices used in those composites are petroleum-based products whose sources are pollutive and non-recyclable.

Since the past decade, the implementation of natural fibers as reinforcements in composite materials has become an emerging trend, initially in research and later in full-scale industrial applications. The reason behind this growing interest is that the fibers are sustainable and eco-friendly. They also have interesting properties like good thermal insulation, high specific stiffness, and good acoustic insulation. Moreover, with the implementation of these fibers, there is no need for the existing composite processing technology to adapt. Concerning resin systems, bio-mass from agricultural wastes stands as an excellent alternative source for the synthesis of thermoset resins. Currently, many research efforts are being made, both academic and industrial fields, to improve the mechanical performance of these composites for high-performance applications. In order to achieve performance levels compatible with structural applications, the mechanical properties, along with the quality of the composite, must be optimized by adjusting the processing parameters like cure temperature, resin injection pressure, and compaction pressure. Nevertheless, the efforts to investigate the processing conditions of natural fiber composites

are sparsely addressed in the literature. Thus the objective of this dissertation is to propose and contribute to the development of bio-sourced composites reinforced with plant fibers for high-performance applications.

1.1.1 Project BIOCOMPAL

The research presented in this thesis is carried out as a part of an INTERREG project BIOCOMPAL, which is funded by the EU (European Region Development Fund). The main objective of this project is to develop a new low-carbon and high-performance bio-based lightweight materials for structural applications in the transport sector like aeronautics, railways, etc. This project addresses the performance of flax fiber composites from the point of origin. Currently, the market is lacking in the areas of bio-based composites, which are fire-resistant. Thus, this project addresses the performance of these bio-based composites starting from the point of origin to the final composite part. This project is handled by five partners who are responsible for a specific objective, as summarized below:

1. Production of innovative high-performance thermoset resins based on renewable natural phenols, which is handled by MateriaNova, Belgium.
2. Development of new designs for high-performance textile reinforcements based on natural technical fibers from regional flax crops is handled by CentexBel, Belgium and Inagro, Belgium.
3. Manufacturing and characterization of flax fiber composites using the developed fabrics and bio-sourced resin are carried out by IMT Lille Douai, France and ARMINES, France.

1.2 Subjects

The subjects of this dissertation can be mainly classified into two categories. The first is the manufacturing of composite plates and the second one deals with the mechanical characterization of composite plates, as further described below:

1. Manufacturing of composite laminates

The first subject is to study the influence of processing parameters of flax fiber-reinforced composites to produce high quality composite laminates. This concerns the in-depth understanding of the formation of voids during the Liquid Composite Molding (LCM) process and possibilities in reducing them i.e., process optimization.

This is carried out in two steps; one being the experimental characterization, and the other, mathematical modeling by incorporating the flow model proposed by Nguyen et al. [1]. The second subject would be to understand the capillary wicking of flax fibers considering liquid absorption and fiber swelling by both experimental techniques and mathematical modeling. The third subject will be to manufacture composite laminates with very low void content using compression molding. These laminates would be used to characterize the material properties to understand the influence of liquid absorption during manufacturing.

2. Characterization of instantaneous & in-service behaviours of flax fiber composites

Mechanical characterization of composite plates is carried out to gain knowledge of their behavior and failure mechanisms. Hygrothermal aging of composite specimens will be studied to understand their real-time behavior in humid environments. Further, the influence of operating temperature on the mechanical properties of composites is studied. In both these studies, a comparison will be made between a commercial grade epoxy and a bio-based thermoset resin.

1.3 Organisation of dissertation

According to the research subjects, the chapters in this dissertation are arranged in the following sequence.

In **Chapter 2**, a background of the use of natural fibers and fiber characterization methods for tensile properties of flax fibers is presented. A brief review of different types of matrices is provided to highlight the need for bio-based resins. Finally, this chapter is ended with a short summary of manufacturing techniques and preform permeability characterization techniques.

In **Chapter 5**, an investigation of the influence of the curing cycle on the flax fiber composites is discussed. This part mostly concentrates on linking the fiber-matrix interface and the improvement in tensile behavior of composites.

Chapter 4 is devoted to the experimental characterization and mathematical modeling of capillary wicking phenomena of flax fibers. A comprehensive description of existing techniques and models to characterize and understand the wicking phenomenon is presented. Based on the experimental results, the empirical constants of the permeability model are determined and then implemented in the proposed model to predict the mass of test liquid uptake by the flax fibers.

In **Chapter 5**, the influence of the Resin Transfer Molding (RTM) process parameters,

especially resin injection pressure, on the quality of the composite part is investigated. The void content in the composite part is experimentally determined using micrographs. In order to predict the void formation in natural fiber preforms during RTM, a mathematical model is proposed to estimate the void content. Later, the influence of the fiber distribution inside a tow on the tow permeability is presented to understand the differences between classical fibers like glass or carbon and natural fibers.

Chapter 6 highlights the uniqueness of the flax fiber composites with bio-based resin under extreme conditions. These composites are subjected to high temperatures and hygrothermal aging to identify their performance under such extreme loads.

Finally, in the last chapter, the results are recapitulated to redraw the conclusions of this dissertation and also, in addition, recommendations for future works are presented.

Chapter 2

Flax fibers and their composites

Natural fibers and their composites are considered as good alternatives to conventional glass fiber composites (notably in the transport sectors) by virtue of their low ecological footprint. They are lightweight ($\rho = 1.5g/cm^3$) materials, relatively inexpensive, and structurally stiff materials, which can thereby form low weight structures without compromising the structural performance [2, 3]. According to a survey, the production rate of bast fibers like jute, flax, hemp, and sisal is higher than that of any other natural fibers [4]. Extracted from the bast of plants, these fibers are of cellulose polymeric content with more of a crystalline structure [5]. In Europe, flax and hemp fibers are the most used as reinforcements for composite applications because their cultivation is abundant whereas, the research on jute and sisal fiber-reinforced composites is carried out at large in tropical and sub-tropical regions. The following sections will present flax fiber's properties, characterization methods, and their composites.

2.1 Flax fibers

Flax fibers are abundantly cultivated in Europe, where France and Belgium are the leading producers with nearly 130 Mton of annual production [6]. In France, the cultivation of flax fibers is mostly prevailing in the regions of North, Picardy, and Normandy. Flax plants are annual plants with a relatively short growing cycle, about 100-120 days between sowing (March-April) and harvesting (July-August) depending on the plant variety. The production of flax fibers includes three main steps. Firstly, fibers are harvested at the time of their maturity and are subjected to retting (either dew retted or wet retted), a process where the microorganisms present in the atmosphere attack the cortical tissues of the flax plant under warm and moist environment enabling easier decortification [7]. Then the retted stems are passed through a scutching machine to separate the fibers from stem. During this process, along with the long fibers, by-products like seeds and shives

can be obtained, which can be used to produce edible oils and insulation materials or non-structural composite parts [8]. Scutched fibers are hackled to remove any other pertaining impurities and are either spun into tows or yarns depending on the final application.

2.1.1 Morphology and constituents

Flax fibers, similar to wood fibers, have a complex microstructure. The elementary fibers have a polygonal cross-section, which varies along the length of fiber [9]. At the micro-scale, the flax fiber cell is a concentric cylindrical structure comprising several layers. These layers are called cell walls. There are two significant cell walls, primary and secondary cell walls. Primary cell walls are usually thin and are mainly composed of lignin, whereas secondary cell walls can be further divided into three sub-divisions (S1, S2, S3), which are enclosing the lumen (the hollow part of the fiber). Of these three sub-walls, the S2 wall is the thickest and contains the microfibrils, which represent about 70-75% of the weight and are the major contributors to mechanical properties of fibers [10]. The primary chemical constituents of a flax fiber are cellulose, wax, lignin, hemicellulose, and pectin. Cellulose is the stiffest of all the components and is highly hydrophilic due to open hydroxyl groups in its chain. This is the usual reason why the interface is bad between a flax fiber and a hydrophobic polymer matrix [11]. Lignin and pectin are only the bonding agents in cell walls (see Table 2.1)

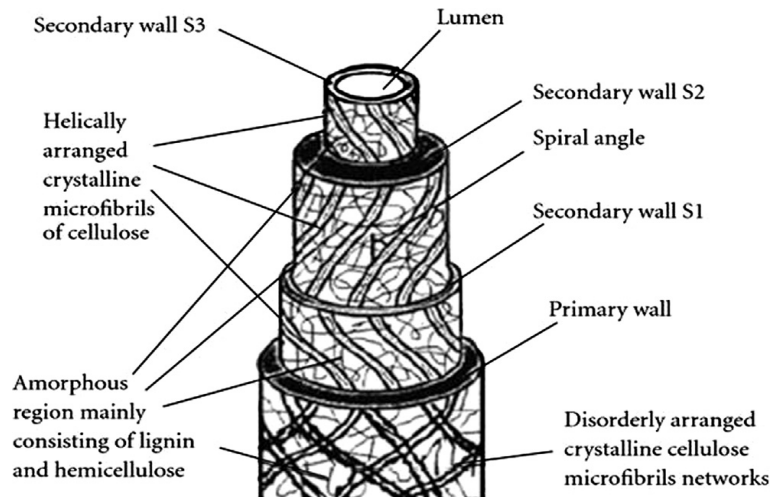


Figure 2.1: Illustration of micro structure of flax fiber [5]

2.1.2 Characteristics of flax fibers

For flax fibers, determining the physical properties like density and fiber cross-section is not as straight forward as for other fibers like glass and carbon. The presence of lumen

Constituent	% content	reference
Cellulose	62-75	[12]
Hemicellulose	11-20.6	[12]
Pectin	1.5-2.3	[12]
Lignin	2-3	[13]
Wax	1.5-1.7	[12]

Table 2.1: Chemical composition of flax fibers

inside of these fibers makes the measurements difficult and inaccurate. Also, because these two parameters are highly dependent on the maturity of the plant. Hence, it is necessary to characterize the values by isolating the plausible influencing factors like extraction position from stem and period of harvest [14]. Recently, two separate studies made an effort to establish a standard method for density measurement of natural fibers [15, 16]. Both studies presented a comparative study on different density measuring techniques and concluded that helium pycnometer and Archimedes principle to be more suitable methods for natural fibers. For flax fibers, a density of $1.5gm/cm^3$ was determined using gas pycnometer and Archimedes principle [16].

The methods to measure the cross-section of flax fibers or any natural fibers are of current research interest. It can be seen in Table 2.2 that the diameter of the flax fibers is highly varied (about 20% of the mean value). This variability is caused because every fiber is different from one another as their growth rates are different. Also, as stated in the previous section, their physical structure is not homogeneous (see Figure 2.2). Hence, advanced imaging techniques are required to characterize the actual fiber cross-section [17]. In order to overcome those difficulties, researchers suggested the calculation of apparent fiber cross-section by considering that the fiber has a circular cross-section, which causes issues while characterizing the strength of fibers [18].

As explained in the previous section, because of their multi-cell and multi-component structure, flax fibers exhibit particular mechanical behaviors. When these fibers are subjected to tensile loading along the axial direction, the stress-strain curve shows a non-linear trend. Two different slopes can be identified on the tensile curve (for example, see Figure 2.3) with a point of inflection. This point of inflection is referred to as "Knee point". It is supposed that the initial nonlinearity is caused by the initiation of the reorientation of cellulose fibrils in the secondary wall (S2) [10, 13, 19]. This occurs between strains of 0%-0.1% and 0.1-0.3%. The response is visco-elastic. The second slope is much related to a typical characteristic elastic curve, which is usually observed between 0.3% strain and the strain at rupture.

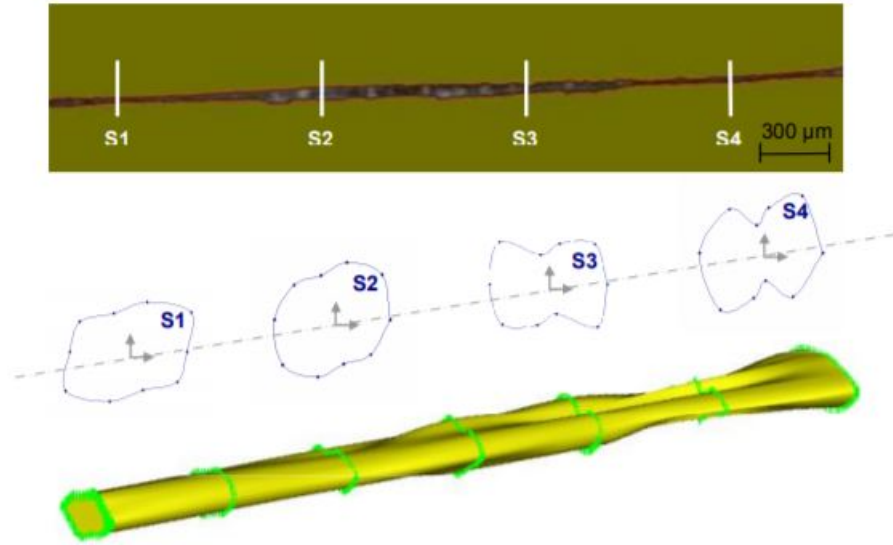


Figure 2.2: Illustration of irregular cross-section of natural fiber[17]

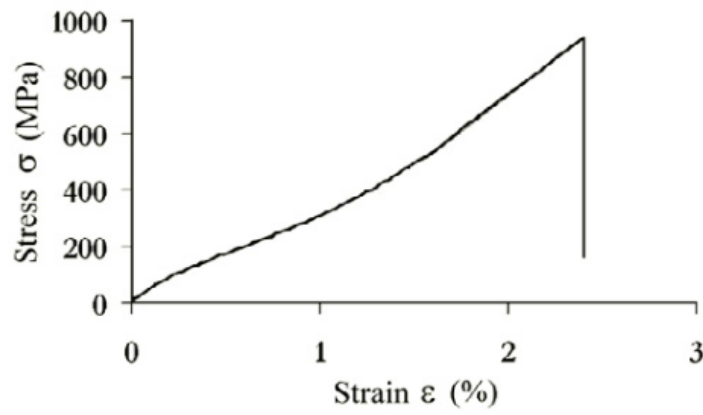


Figure 2.3: Stress strain curve of an elementary flax fiber [9]

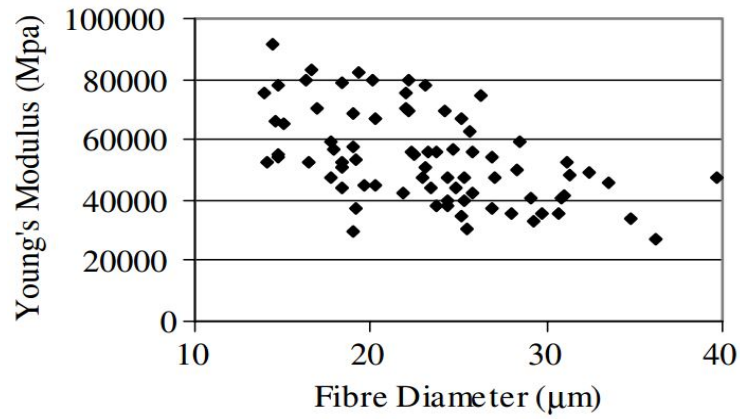


Figure 2.4: Dispersed values of Young's modulus and diameter of flax fibers[9]

Flax variety	Modulus (GPa)	Stress at break (MPa)	Strain at break (%)	Diameter (μm)	Ref
Hermes	48.9 ± 12.0	1066 ± 342	2.8 ± 0.8	18.6 ± 3.9	[20]
Andrea	48.3 ± 13.8	841 ± 300	2.2 ± 0.8	18.1 ± 3.9	[20]
Marylin	57.1 ± 15.5	1765 ± 432	2.1 ± 0.6	13.9 ± 2.7	[20]
Hermes-up	59.1 ± 17.5	1129 ± 390	1.9 ± 0.4	19.0 ± 3.5	[9]
Hermes-middle	68.2 ± 35.8	1454 ± 835	2.3 ± 0.6	19.6 ± 6.7	[9]
Hermes-bottom	46.9 ± 15.8	755 ± 384	1.6 ± 0.5	20.1 ± 4.1	[9]
Agatha-up	51 ± 22	753 ± 353	1.8 ± 0.7	21.65 ± 5.3	[21]
Agatha-middle	57 ± 29	865 ± 413	1.8 ± 0.6	21.3 ± 6.3	[21]
Agatha-bottom	51 ± 26	783 ± 347	2.0 ± 0.9	23.5 ± 7.9	[21]

Table 2.2: Tensile properties of elementary flax fibers

Table 2.2 and Figure 2.4 show examples of the dispersion of mechanical properties of flax fibers. Charlet et al. [9, 21] characterized the fibers extracted from the same bast but at different positions. A well-distinguished difference was observed in the mechanical properties. Haag et al. [22] conducted a study to observe the variation of mechanical properties of the same type of fiber over different years. It has been concluded that the harvest time, weather conditions, and retting methods influence the fiber properties.

Since flax fibers are not continuous, unlike glass or carbon fibers, the mechanical characterization becomes an issue. On the one hand, an elementary fiber can be considered as a long fiber with a fixed length, whereas a technical fiber can be considered as a bundle with many elementary fibers glued together by pectin. The average length of an elementary fiber is around 20-35mm with an average diameter of 20 μm . Due to this irregularity in length, the technical fibers also have an irregular length with a varied number of fibers. In general, flax fibers, both technical and elementary fibers, are tested using the paper frame method, as suggested by NF T25-501 standard [23]. Even with these standards, the standard deviation of experimental results is high (25-30% in strength and 40-45% in modulus). It is also observed in the literature that the fiber surface has a striated structure consisting of macro fibrils arranged parallel and oriented in the longitudinal fiber direction (see Figure 2.5).

2.2 Matrix

The polymer matrix is the second constituent of composite material and is equally important as the reinforcement because it binds the reinforcements together, holds the shape

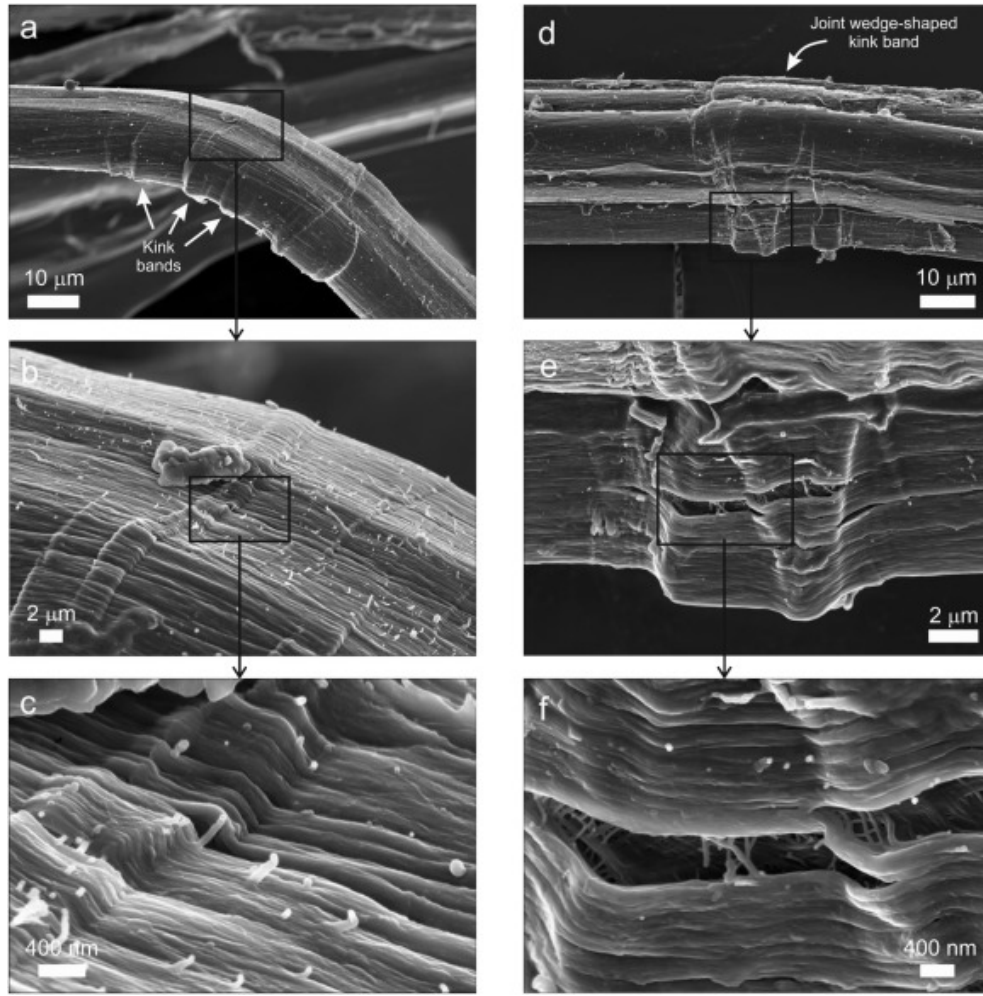


Figure 2.5: Surface morphology of flax fibers [24]

and transfers stress to the fibers. Based on the thermo-mechanical behavior, polymer matrices can be broadly divided into two categories: thermoplastics and thermosets. Even though the principle of binding fibers together is the same, the chemistry and the processing parameters are quite different during manufacturing. The selection of the matrix type not only defines the manufacturing process that should be used but also determines the mechanical behavior of the final part. Usually, thermoset resins are relatively brittle with strain at the break being 4-5% whereas thermoplastics are ductile and rarely brittle with strain at break around 100%-200%. Some thermoplastics (e.g., elastomers) also exhibit rubbery nature. Thermoset polymer matrices are generally operated below their glass transition temperature (T_g) because they become quite rubbery above their T_g whereas thermoplastic polymers are mostly operated above their T_g . Depending on the chosen polymer matrix, there are several advantages and disadvantages, as shown in Table 2.3.

Thermosets play an important role in the polymer industry owing to their high flexibility, good chemical resistance, and high modulus and strength. Due to their high cross-linking density, the thermoset resins cannot be reshaped after cure and possess low

Thermoset	Thermoplastic
Advantages	
Low viscosity	Shorter processing time
Good thermal resistance	Good chemical resistance
High strength and stiffness	Higher impact resistance
Creep resistance	Post formability
Disadvantages	
No reshaping after cure	Complex flow behaviour
Residual stresses	Residual stresses
Toxic	Low thermal stability
Strict cure kinetics	Poor fiber-matrix interface

Table 2.3: Advantages and disadvantages of thermoset and thermoplastic matrices for composite applications

impact resistance. Compared to the thermoplastic resins, thermosets have lower molecular mass and lower viscosity, which allows easier processability of composites. These resins are polymerized either by initiating the cross-linking of monomers with an addition of a catalyst or by increasing the temperature. The degree of cure is defined to determine the amount of cross-linkages. The degree of cure greatly depends on the processing conditions, and its value lies between 0 to 1, where 1 indicates a complete cure.

Benzoxazine resins belonging to a class of phenolic resins are gaining great interest in the field of thermoset materials. This resin group was first popularized by Ning and Ishida [25] in the late 90s. These new resins offer an excellent balance of material properties, combining both the specific advantages of traditional epoxy and phenolic resins like easy thermal curing without the need of hardeners or catalysts, limited shrinkage, low coefficient of thermal expansion, high glass transition temperature (T_g), low moisture absorption, and low dielectric properties. These advantages make these resins a good competitor in the field of high-performance materials. The synthesis of these benzoxazine resins is quite versatile, i.e., there are wide varieties of monomers of which the current research is pertaining to renewable and sustainable sources of these monomers. The monomers for benzoxazine resin are generated from commercially available and inexpensive phenols, amines, and formaldehyde, offering an extraordinary monomer design flexibility. Phenolics groups are broadly distributed in the plant kingdom and are the most abundant secondary metabolites in plants [26–28]. The fact that natural phenols exist in abundance within plant sources or wastes generated from agro-sources makes them potential substitutes for phenolic petrochemicals. Even though they are abundant,

Property	Benzaoxazine resin	Epoxy resin
Tensile modulus (GPa)	5.3	3.4
Tensile strength (MPa)	31	73.3
Flexural modulus (GPa)	4.6	10
Flexural strength (MPa)	132	112
Fracture toughness K_{IC} ($\text{Pa}\sqrt{m}$)	0.94	1.04
Fracture energy G_{IC} (J/m^2)	352	168
T_g ($^{\circ}\text{C}$)	130-200	60-150

Table 2.4: Comparison between Epoxy and Benzaoxazine resin

the cost of extraction and synthesis should be taken into consideration. Cardanol which is extracted from cashew nut shell liquid (CSNL), has become one of the few primary and economic sources of naturally occurring phenols. This CNLS is directly extracted from the shell of the cashew nut, fruit of the cashew tree, which is mostly grown in India, East Africa, and Brazil. This aromatic renewable source represents a promising natural alternative to petroleum-derived phenols.

In the case of volatile resins like Phenols, however, air bubbles are entrapped during the curing of resin due to the presence of solvents or air in the resin. Although it can be avoided by proper degassing of resin in many cases, if the polymerization occurs only at high temperatures, degassing may be an issue. Concerning the voids induced by the volatility of the resin, there are studies dedicated to prepregs and to the case of injected resin during resin transfer molding [29–31]. Pupin et al.[30] investigated the effect of water content on the formation of voids in a resol based phenolic resin and suggested that a consolidation pressure higher than water vapor pressure should be applied before gelation period to prevent the entrapment of water vapor leading to residual voids and provided a void map for that particular resin system (see Figure 2.6).

2.3 Manufacturing process

2.3.1 Liquid composite moulding

Nowadays high-performance composite parts are often manufactured by the consolidation of impregnated textile reinforcements (prepregs) in an autoclave. This method is often used by the aerospace industry to produce parts with high quality with low void content, usually less than 1%. However, due to the high investment costs, Out of Autoclave(OoA) methods are being developed to overcome the cost issues and reduce energy consumption. Liquid Composite Moulding processes are one among such processes which can

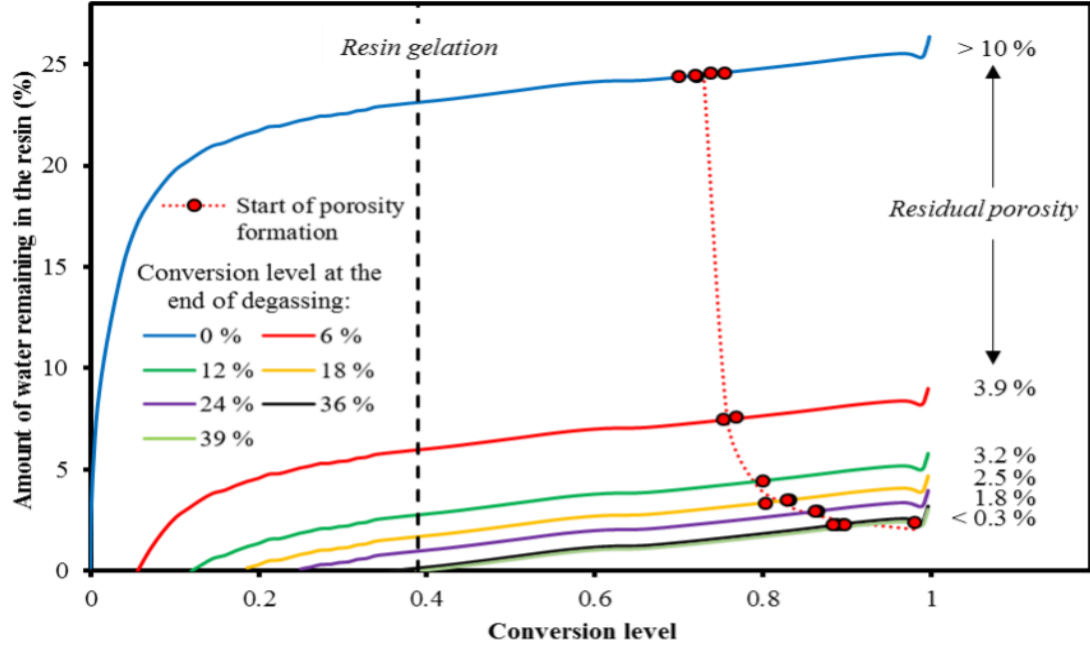


Figure 2.6: Residual porosity map of a phenolic resin [30]

be relatively flexible in comparison to autoclave. Liquid composite molding is a global term which encompasses many major processes, namely Vacuum infusion, Resin Transfer Moulding (RTM) and Compression RTM (C-RTM). The processing parameters like injection pressure and temperature are limited by tooling. If the tooling is completely rigid, the fiber volume fraction can be controlled, which leads to the production of high-performance parts.

During an LCM process, liquid resin is forced through a fibrous porous medium during the injection. The mathematical model for the flow in a porous medium was first proposed by Henri Darcy [32] in 1856. In his experiments, he analyzed the water flow through a porous bed made of sand and proposed an empirical model relating the volumetric flow rate Q , the viscosity of fluid μ , the pressure drop ΔP over length l of the sand bed and cross-sectional area of sand bed A as:

$$Q = \frac{\tilde{C}A}{l}\Delta P \quad (2.1)$$

Where \tilde{C} is the ratio of permeability (K) and viscosity. This equation can be modified by dividing the cross-sectional area of both sides to obtain the volumetric flow rate resulting in the velocity of fluid \vec{v} in porous media. The pressure gradient (∇P) is usually assumed to be linear, and the K is defined as the permeability of fluid which in simple terms can be explained as a number defining the ease of fluid flow through a given porous media. By considering the flow over a distance x , the Equation 2.1 can be rewritten as:

$$\vec{v} = \frac{-K}{\mu}\nabla P \quad (2.2)$$

Darcy's law represented by Equation 2.2 can only be used in the case of homogeneous materials. If the permeability is expressed in a tensor form and in three-dimensional space, pressure gradient, the law can be applied to any porous medium as long as \mathbf{K} is known. It should also be noted that Darcy's law can only be used in case of laminar flows, i.e., where the fluid motion is characterized by smooth streamlines. For textiles with anisotropic properties, the permeability tensor can be reduced just to the principal permeability values.

$$K = \begin{bmatrix} K_{11} & 0 & 0 \\ 0 & K_{22} & 0 \\ 0 & 0 & K_{33} \end{bmatrix} \quad (2.3)$$

where K_{11} , K_{22} , K_{33} are the principal permeabilities.

The permeability measurement is usually carried out in two ways: unsaturated and saturated flows. Unsaturated permeability (K_{unsat}) is measured while the resin is infiltrating the porous medium. Here the term 'unsaturated' is used as the porous bed is not completely filled with resin (in the vicinity of flow-front). The evolution of flow front (x) is monitored and is plotted against time(t) to calculate unsaturated permeability as follows:

$$x^2 = \frac{2K_{unsat}\Delta Pt}{\mu\phi} \quad (2.4)$$

where ϕ is the preform porosity which is expressed as $\phi = (1 - V_f)$. Once the preform is completely saturated, the mass flow rate (Q) is used to calculate the saturated permeability K_{sat} .

$$K_{sat} = \frac{Q\mu L}{A\Delta P} \quad (2.5)$$

Although permeability is a material property, a huge discrepancy in values can be observed for the same material [33]. It can be speculated that these differences can be caused due to the test conditions and test fluids. In the second permeability benchmark exercise conducted by various laboratories worldwide, all the research teams employed the same measurement technique to measure the permeability, however, obtained a relatively small scatter in value [34]. Nonetheless, the change in injection pressure or fluid viscosity leads to high scatter of values. It was noted that the ratio of unsaturated to saturated permeability could be between 0.25 to 4 and in many cases less than one [35–37]. It is supposed that this difference between unsaturated and saturated permeability is due to the air entrapment during impregnation [38]. Park and Krawczack [39] stated that these differences could be due to the change in viscosity during impregnation, uncertainty in flow front tracking, nesting of fabrics, deviation of fabric direction from principal flow direction, and role of capillary pressure, etc. They suggested that in order to obtain accurate unsaturated permeability values, it is necessary to obtain exact pressure gradient at flow front by using pressure transducers and air void migration should be taken into account because it may

affect the mass conservation conditions. Air bubble position and migration speed should also be taken into account because it significantly influences the local pressure gradient [40].

Once the permeability of a preform is experimentally characterized, for different values of fiber volume fraction, it is convenient to represent the permeability as a function of fiber volume fraction. One such widely used model for estimation of permeability is given by Kozney and Carman [41].

$$K = \frac{D_f^2}{k} \frac{(1 - V_f)^3}{V_f} \quad (2.6)$$

where D_f is the diameter of the fiber, and k is the Kozney constant representing tortuosity of the porous medium [41]. It is well known that natural fibers absorb liquid and swell [42, 43]. Hence, during the impregnation process, the resin is absorbed into the natural fibers, and the cross-section of natural fibers is increased. As a result, the fiber swell decreases the size of flow channel which is a key to the permeability. In fact, fiber swell is dependent on the type of liquid [44]. Hence in the case of natural fiber preforms, the size of the flow channel will highly vary because the fiber cross-section is dependent on the fiber swell. Hence, the permeability shows a strong dependency on the liquid used to characterize the preform. Even though the permeability is a material property, a study by Nguyen et al. [43] found that the permeability value has been affected by fiber swell due to liquid absorption. They tested a flax preform with two different liquids and suggested a modified Kozney equation for estimation of permeability value considering the swelling coefficient.

$$K = \frac{1}{A} \frac{(1 - f_{sw}^2 V_f)^{(n+1)}}{(f_{sw}^2 V_f)^n} \quad (2.7)$$

where V_f is the fiber volume fraction of the preform, n, A are the empirical model constants and f_{sw} is the fiber swell ratio which is the ratio of wet fiber diameter to the initial fiber diameter.

Using the mass conservation principle for the incompressible fluid, the fluid flow through a porous medium is written as:

$$\nabla \cdot u = 0 \quad (2.8)$$

$$\nabla \cdot \left(-\frac{K}{\mu} \nabla P \right) = 0 \quad (2.9)$$

However, in reality, because of the dual scale porous structure of the fiber preform, the Equation 2.9 is incorporated with a sink term which represents the fluid sink into the tows during impregnation. This was first suggested by Pillai et al. [37] and was later adopted by many other works [45–47]. Similar to that of synthetic fibers like glass or carbon, even the Equation 2.9 (without the sink term) was applied to the natural fiber composite processing [48, 49]. These models can predict the flow front advancement reasonably well

at lower fiber volume fractions, but due to the assumptions made, the models deviate from experimental results at high fiber volume fractions. Masoodi et al.[49] suggested the first flow model for natural fiber preforms with the help of wicking tests.

$$\nabla \cdot \left(-\frac{K_{eq}(t)}{\mu} \nabla P \right) = (b-1) \frac{\partial \epsilon_{f,t}}{\partial t} \quad (2.10)$$

where, $\epsilon_{f,t}$ is the porosity of fibers at time t , $K_{eq}(t)$ is the equivalent permeability at time t and b is the ratio of absorption to swelling rate. In the above equation 2.10, the absorption rate of fibers was assumed to be directly proportional to the swelling rate of fibers. A study by Schuchardtl et al. [50] showed that $b = 1$ whereas Javadi et al. [51] experimentally found the value of b to be between 0.991-0.995 indicating that the even though the contribution of right-hand side term is less, but should be considered. Francucci et al. [48] tried to predict the flow front advancement using two different methods, one where the preform permeability was constant and other where the permeability of the preform varies heterogeneously with respect to fiber swell as the immersion time of fibers is different along the injection length causing in different swell ratios. The suggested model was similar to Equation 2.10 but without the sink term.

$$\nabla \cdot \left(-\frac{K(t,x)}{\mu} \nabla P \right) = 0 \quad (2.11)$$

In reality, it was shown that the liquid absorption and fiber swelling of flax fibers affect the mass conversation of control volume forcing to consider both micro sink and source in the Equation 2.11 because during the liquid impregnation into natural fiber preforms, both fiber swelling and liquid absorption are functions of time and position of flow front leading to a change in permeability of preform. Nguyen et al. [1] suggested a model with aforementioned terms and experimentally validated it.

$$\nabla \cdot \left(-\frac{K(t,x)}{\mu} \nabla P \right) = S_{micro}(t,x) \quad (2.12)$$

where S_{micro} is the sink and source term at distance x for a given time t . The contribution to the sink term was from the phenomenon of liquid absorption of flax fibers, whereas the source term is linked to the phenomenon of fiber swell. It was found that the model holds good at both lower and higher fiber volume fractions, unlike the other models (Equations 2.10, 2.11).

2.4 Void formation in composite materials

Regarding the sources of the voids in composites, in this work, the mechanical entrapment of the air bubble will be focused on. It is the primary mechanism that leads to higher

void content in the final composite part manufactured using the LCM process [38, 52, 53]. Air entrapment is caused by the dual scale structure of fabrics leading to the non-uniform flow at the flow front. For the sake of easy understanding, the voids inside the fiber tow are referred to as "tow voids", and voids that are observed in the channel are referred to as "channel voids". Bréard [38] described the three main stages of resin flow through a dual scale porous media, (a) filling of inter-tow spaces, (b) filling of intra-tow spaces and (c) two-phase flow. In the LCM processes, during impregnation, the channel flow (flow between tows) is dominated by viscous effects, and in the local regions with high fiber content, i.e., tows, the flow is dominated by capillary forces. At high flow velocities, flow between the tows is faster than flow inside the tows resulting in higher chances of air entrapment inside the tows. Similarly, when the flow is dominated by capillary flow, the air is entrapped in the channels leading to the formation of channel voids.

In the late 90s, researchers started to investigate the formation of microvoids during liquid composite molding. Lundstrom et al. [54] studied the influence of process parameters on void formation in Resin Transfer Molding. They observed that the void content increases along the length of injection, and the process parameters like injection pressure, cure pressure, post-filling, and others have a significant effect on the final void content. Also, they modeled air bubble compression during LCM using ideal gas law [55]. Following the work, the research group of James Lee investigated the air bubble formation in random mat [56–58]. Patel et al. [57] suggested a void formation model that considered the modeling of the formation of air bubbles during impregnation and related it to their experimental results by suggesting the use of modified capillary number which is the ratio of viscous to capillary forces during impregnation.

$$Ca^* = \frac{\mu v}{\gamma \cos \theta_c} \quad (2.13)$$

where μ is the viscosity of the liquid, v is Darcy's velocity, γ is the surface tension of the liquid, and θ_c is the contact angle between the fibers and liquid. The macroscopic resin flow can occur in two directions relative to the fiber direction. Through analytical modeling, it has been shown that when the flow is perpendicular to the fiber direction, i.e., transverse flow, the voids are distributed throughout the composite, whereas in case of flow parallel to the fiber direction, i.e., longitudinal flow, void formation is localized to the flow front region [52]. For the parallel flow, void localization at the flow front was also experimentally observed as significantly higher void content was found to be closer to the vent side of the laminate. Previously, it has been shown that there exists an intermediate velocity that results in low void content. This velocity is specific to a particular reinforcement. Studies have found an optimal capillary number based on local residual porosity for a given reinforcement type [52, 59–61]. Some studies even suggested

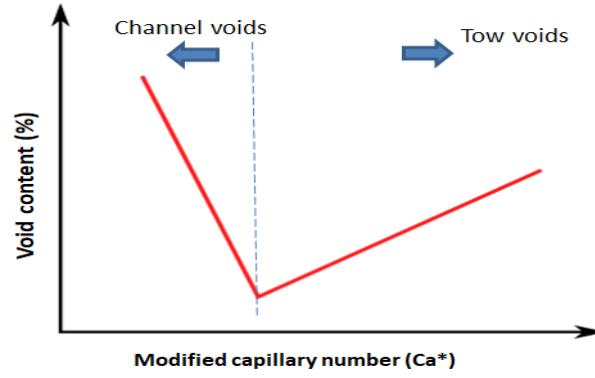


Figure 2.7: General representation of variation of void content with modified capillary number

that it can be investigated from capillary rise experiments [60, 62–64]. Several researchers also studied the void formation mechanisms during RTM using analytical and numerical models. Kang et al. [65] suggested a mathematical model that predicts the void formation based on the competition between tow and channel flow fronts, which laid the path to the void modeling during resin impregnation in LCM. A detailed review of modeling schemes and approaches was presented in [35].

Void formation models are usually meant to predict the voids created at the flow front for a particular instantaneous flow front velocity v at a particular point in time and space. The overall concept of channel and tow void formation as a function of modified capillary number is commonly represented, as shown in Figure 2.7. Gourichon et al. [61] showed that for woven fabrics, there exists a transition plateau where a low void content can be achieved for a relatively larger process window when compared to unidirectional fabrics for which the process window is relatively smaller. The main reason for this transition plateau for woven fabrics is that the capillary flow inside the weft and warp tows, and the channel flow can reach the same value because of dual scale phenomena. Several researchers pointed out that the optimum capillary number lies in the range of $10^{-2} - 10^{-3}$ [52]. Ruiz et al. [59, 66], in their works pointed out that Ca^* lies in the range of 0.008-0.01. Similar results were presented by Zingraff et al. [67]. Nevertheless, the argument of optimum injection velocity holds, but the range of those values is highly susceptible to fabric architecture.

2.5 Void characterization techniques

Even though the concept of an optimum injection velocity for high-quality composite parts exists, a great hindrance in the implementation of the method can be noted from the industrial point of view. The main issue is the characterization of 'optimum velocity.'

As stated previously, this velocity is highly dependent on the fabric type and the resin system. Thus, even with a slight change in their properties, the value of optimal velocity will be significantly varied. Hence, this calls for an extensive experimental investigation to understand the particularities involving in determining this velocity. Nevertheless, the void formation models can be used, but the existing models in the literature are either simplified for ease of estimation [64, 66, 68] or some do not take into account the specificity of the actual flow inside the mold. Also, only a handful of models exist which can completely simulate the void formation, compaction, and transport [52, 69, 70]. Therefore, in practice, even if these models are utilized to estimate the void content, they are always used in tandem with experimental characterization. Experimentally, void content can be characterized either during the mold filling (in-situ) or after the part has been cured (ex-situ). In situ methods are mostly used in the research field and dedicated to the study of void formation [68, 71, 72]. These methods include the usage of molds fitted with dielectric sensors for detection of air bubble volume [68], thermal conductivity measurements [71], or by measuring the air bubble volume using optical techniques [64]. These techniques are feasible only when the part is thin, as the detection of an air bubble in thick parts is difficult. Recently, X-ray tomography was also implemented to study the bubble formation, but it was limited to smaller samples such as a single tow, and not a part scale [73, 74].

Ex-situ measurements are conducted on a cured composite part. This characterization gives in-depth information about the shape of the void and their quantity at a low cost yet laborious tasks. Of all techniques, microscopy is quite frequently used to characterize the void content and morphology [75, 76]. The micrographs are treated to obtain black and white images. The pixels are counted to obtain information regarding the voids by using open-source software like ImageJ. The void content of composites is estimated by extracting samples along the cross-section (see Figure 2.8). The preparation of such samples is particularly challenging as the surface finishing of the microscopy specimens should be clean, smooth, and flat. Any irregularity of the surface may lead to artifacts and wrongful estimation of void content. Another way of void content measurement is through isolation of fibers in a specimen either by matrix digestion or thermal degradation of the matrix (burn-off tests). In matrix digestion, the composite is dipped into a beaker containing a highly concentrated acid, which will dissolve the matrix. The remaining fibers are washed and weighed to estimate fiber mass fraction and void content. Similar to the matrix digestion method, in the burn-off test, the composite is placed in an oven and heated to temperatures around 550°C to degrade the matrix thermally. If the fiber volume fraction is already known, the void content of the composites can be directly estimated from density measurements. These two methods are mostly used for glass or carbon



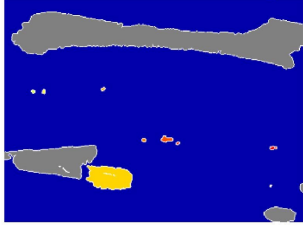

1. Micrograph	2. Convert colourmap to grayscale image	3. Gaussian filter	4. Threshold
			

Figure 2.8: Image processing steps for micrographs of a carbon/epoxy composite [75]

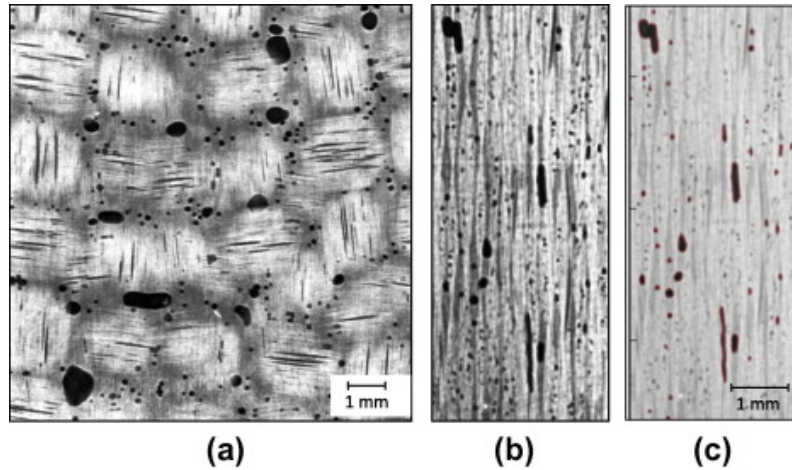


Figure 2.9: Scan images of a Carbon/Epoxy fabric specimen: (a) planar section; (b) thickness section; and (c) thickness section with detected voids [79]

fiber composites, at times basalt fiber composites. However, in the case of natural fiber-based composites like flax or hemp, the latter method cannot be implemented because the fibers start to degrade at 200°C [77]. Although the method of matrix digestion can be implemented for natural fiber-based composites, the selection of digestion acid is quite important because some of the components of fibers may be affected, which in turn can affect the estimation of fiber volume fraction. Therefore, microscopy and density measurements are the only good options in the case of natural fiber-based composites. On the other hand, Micro-CT can be used to determine the void content, position, and shape. As mentioned earlier, however, it involves expensive equipment, and the specimen size is restricted [78] (see Figure 2.9).

2.6 Flax fiber composites

As explained in the previous sections, the flax fibers themselves exhibit a non-linear behavior when subjected to tensile loading. For a unidirectional composite material, the

flax or hemp composites can match with conventional glass fiber composites in terms of tensile behavior, because the specific stiffness is equivalent due to their lower density. When the strength of flax fiber composites is compared, the scatter of their properties is less in comparison with the fiber tensile properties. In the case of bending properties, it was found that, in terms of specific properties, flax fiber composites can even outperform common metals like aluminum [80]. Similar to that of single fiber tensile response, unidirectional composites also do have a 'knee' point around at 0.3% of strain indicating the rearrangement of micro-fibrils inside the fibers [81]. Depending on the matrix type, several types of damage mechanisms were identified by many studies either by micrograph observations or in-situ tests, namely, (a) bundle cracking, indicating the individualization of elementary fibers within a bundle, (b) transverse cracking of fiber bundles, (c) matrix cracking, (d) fiber-matrix interfacial damage [82–86].

Madsen et al. [87] had investigated the effect of the process temperature on the mechanical properties of hemp fiber-reinforced thermoplastic composites manufactured by a compression molding technique. The process temperature used for composite manufacturing is shown to affect the tensile properties of the composites. When processing temperature is increased from 180 to 220 °C, the modulus is increased from 19 to 23 GPa, while the ultimate stress is decreased from 240 to 170 MPa, and the ultimate strain is decreased from 0.021 to 0.012. The measured stress-strain curves are nearly identical for different process temperatures, whereas only the ultimate properties are changed. Thus, it is indicated that the effect of thermal degradation is mainly confined to the failure mechanisms in the fibers, and they fail prematurely in composites processed at high temperatures.

To ensure an effective stress transfer between the fiber and the matrix, excellent adhesion between the two components is necessary. A good fiber-matrix adhesion improves the strength of the composite. Because of the hydrophilic nature of the flax fibers and the hydrophobic nature of (most) polymer matrices, the adhesion may not be perfect [88–90]. Intimate contact between fiber and matrix is necessary for them to bond correctly. This can be governed by the degree of wetting. If the wetting of the fibers is insufficient, this may lead to bad interfaces which decrease the stress transfer between the fibers and the matrix. Three main types of adhesion exist: physical adhesion which is deposition of resin on the surface of the fiber, chemical adhesion is where the adhesion between fiber and matrix is achieved by a change in the chemical composition of the fibers and finally mechanical adhesion caused due to the interlocking of fiber and matrix [91]. These mechanisms are explained in detail in Chapter 3.

Along with an excellent interface, a low void content is also required so that there is no premature failure of the composite. For natural fibers, the void (residual and preform)

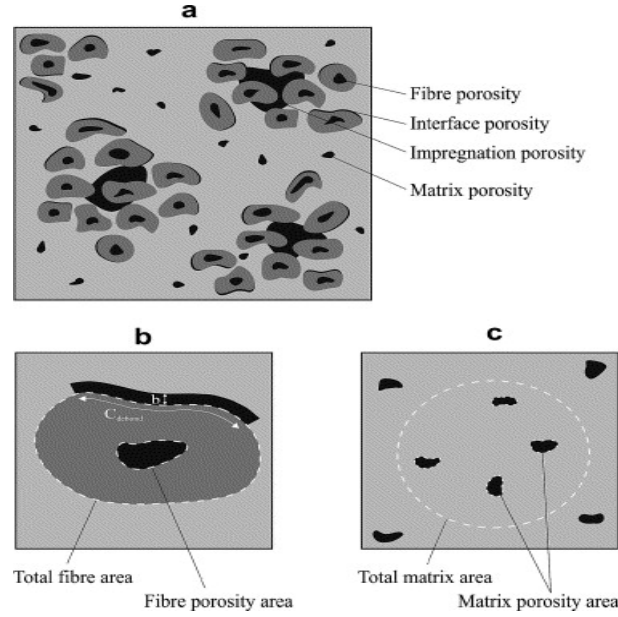


Figure 2.10: Schematic of different types of porosities in natural fiber composites [87]

is highly dependent on several factors like the existence of fiber cavities (lumen), complex surface chemistry of natural fibers, a heterogeneous cross-section of natural fibers, low packing ability of fibers [87] (See Figure 2.10). It was stated by Madsen et al. [87] that as the fiber volume fraction of composites is estimated from weight fraction, the presence of fiber porosities (lumen) will lead to the wrong estimation of composite density. However, in their study, their models predicted the lumen induced void content to be ≈ 0.025 for Hemp/PET composites with an overall void content of 4.6%, and they assumed the same for Flax/PP composites which had a total void content of 9.1%. It was pointed out that this porosity (lumen) cannot be avoided and the only parameters that can be controlled are the interfacial voids and matrix voids. Aslan et al. [92] showed that in reality, the lumen occupies about 1.6% of the fiber area, and it does not largely influence the estimation of fiber properties or porosity. Interfacial voids can be tackled easily by proper selection of matrix system and surface treatment for fibers [93], whereas the impregnation induced voids can be controlled by optimizing the manufacturing conditions of composites. On the other hand, many works reported that the lumen collapses if the compaction pressure is higher, which leads to the reduction of fiber induced porosity which either way was found to be ineffective [94].

Unfortunately, none of the available works in the literature point out the relation among the manufacturing parameters, the residual porosity content, and induced mechanical properties. In order to understand the relationships among processing conditions, fiber volume fraction, and residual void content, a non-exhaustive list of references is presented in Table 2.5, which provides interesting conclusions. Many works consid-

Composite	Method	Processing conditions	Porosity	Characterization technique	Ref
Flax/PP	Compression moulding	200°C, 11bar (staged consolidation)	5-70	Density	[95]
Flax/Epoxy	Infusion	injection at 23°C, post cured at 50°C for 16hours	17.2% (Vf=37.8%) 19.3% (Vf=34.4%)	Micrographs	[96]
Flax/Epoxy	Compression moulding	90°C at 0.1bar& 125°C at 1 bar	0.07%	C-scan	[97]
Flax/Epoxy	Compression moulding	90°C at 0.1bar& 125°C at 1 bar	1.53%	Micrographs	[97]
Flax/PP	Compression moulding	200°C at 20bar	0.42	Micrographs	[8]
Flax/PLA	Compression moulding	175°C, 1 Mpa	8.4	Density	[98]
Flax/PU	Infusion	injection at 23°C, post cured at 65°C for 7 hours	16.3 (Vf=32%)	Micrographs	[99]
Flax/epoxy	Vacuum bag	24H at RT and 8 hours at 60°C	3-20%	Micrographs	[94]
Flax/PP	Compression moulding	0.7 Mpa	3-8%	Micrographs	[87]
Flax/PP	Compression moulding	2.1 Mpa	9.1%	Micrographs	[87]
Flax/Epoxy	Infusion	RT curing	2.7%	Micrographs	[44]

Table 2.5: Process induced porosity content in flax fiber composites

ered the compression molding process to manufacture the flax fiber-based composites and extensively investigated the influence of processing conditions. Indeed, there are a significant number of works reporting the studies of flax composites manufactured with LCM process, but only a handful of them studied the influence of process parameters on the quality of composite. Pucci et al.[44] concluded that the treatment of fibers is essential to ensure good impregnation and fiber wetting, and in their case, the residual void content was decreased from 2.7% to 1.2%.

As previously mentioned that the flax fibers are highly hydrophilic, their composites are highly susceptible to weathering. Even after using highly hydrophobic matrices, it was observed that the properties of the flax fiber composites drastically dropped after a week of water immersion. Reggazi et al. [100] investigated the influence of water aging of flax/PLA composites with two different fiber contents on creep behavior. They observed that when samples were aged at two different temperatures, the composites exhibited an improved creep behavior and a prolongation in time to failure of the composites. This was attributed solely to the plasticizing effect of composites, which makes them ductile. In fact, the same authors also reported in another work that the lost properties of the composites during aging can be obtained by drying them [101]. They also identified a threshold period for each property of composite, which can be regained by drying. It should be noted that water aging is the worst-case scenario even if the composites are usually coated with other substrates or painted.

2.7 Conclusion

Among previous studies on the processing of natural fiber composites using LCM, most contributions just concentrated on the resulting mechanical properties rather explaining the physics behind the process. Recently, works by Pucci et al. [44, 102, 103] and Nguyen et al. [1, 43] shed light on the physics behind on the capillary behavior and macroscopic flow in natural fiber media. Nevertheless there are several factors which were either overlooked or not considered in their proposed models. It should also be noted that no work has addressed the void formation mechanisms in natural fiber media during LCM. To sum up, the following issues were not addressed in the literature.

1. Understanding the effect of LCM process parameters on the part quality

A significant amount of work has dealt with the composites of synthetic fibers like glass and carbon explaining the sources of voids, their creation, and possible ways to reduce their content. In the case of natural fibers, there are some works where the authors dealt with this problem and provided plausible solutions but were restricted only to Autoclave [104] or Compression molding [105]. This part of the work will

be carried out using the models in Equation 2.12 to consider processes where resin flow is predominant.

2. Linking processing conditions and mechanical characterization of flax fiber composites

It has been previously mentioned that due to the particular properties of natural fibers like liquid absorption and fiber swelling, there exists a complex interface between the fiber and the matrix. This is mostly governed by the resin absorption during the manufacturing step. It is also argued that in contact with the humidity, the fiber swells and induces stress on the matrix enclosing the fiber. In other words, the method suggested by Bensadoun et al.[106] to estimate the tensile properties of natural fibers should be refined by considering the phenomena as mentioned earlier.

3. Implementation of a bio-based thermoset resin as matrix for flax fiber composites

There are several works about bio-based thermoplastic composites [107–111] but in case of thermoset composite, there are only some works addressing partially bio-sourced composites. Hence, in this work, a bio-sourced thermoset resin and its flax composites will be characterized. Most importantly, as both materials are bio-sourced, their durability in extreme environments is studied.

Considering the above stated issues, the overall objective of this dissertation is to investigate and explain the phenomena that take place during manufacturing and testing of 100% bio composite laminates aiming at high performance structural applications.

Chapter 3

Tensile characterization of flax fibers

3.1 Introduction

In the previous chapter, the issues pertaining to tensile characterization of flax fibers were described. It was also pointed out that the fiber tensile strengths are also dependent at which processing step these fibers are being characterized. In the Figure3.1, it can be noted that there are various steps between the harvest and the final product. A handful of studies in the literature has pointed out that fibers which are scutched can be directly used as reinforcements without combing/hackling them [8]. In that study, it has been pointed out that both scutched and hackled fibers exhibit similar performance whereas scutched fiber had a higher hand. As the fibers undergo combing steps, there is a higher chance for them to get damaged and lose their integrity. On the other hand, it will be difficult to remove the pertaining impurities around the fibers without hackling. There has always been a constant criticism on the method of characterization of tensile properties of natural fibers. A conventional method that has been adopted by every research group is single fiber testing, but many have reported that this method, although provides value is not accurate because there are several factors influencing it. Firstly, the measurement of the diameter of the fibers and their cross-section is not straightforward. These two parameters are neither constant along the fiber nor reproducible for other fibers. This leads to high variations in the tensile strengths and moduli (as seen in Table 2.2. [Details are presented in Chapter 2]).

In this study, after assessing the pros and cons of the available testing methods, Impregnated Fiber Bundle Test (IFBT) method was selected as a suitable test. This method relies on the estimation of fiber properties from composite properties. For this reason, it can be argued that there will be an effect of processing conditions on the estimated properties. In fact, it has also been debated that if this IFBT method is utilized, the efficiency factor (factor defining the contribution of reinforcement to the strength of com-

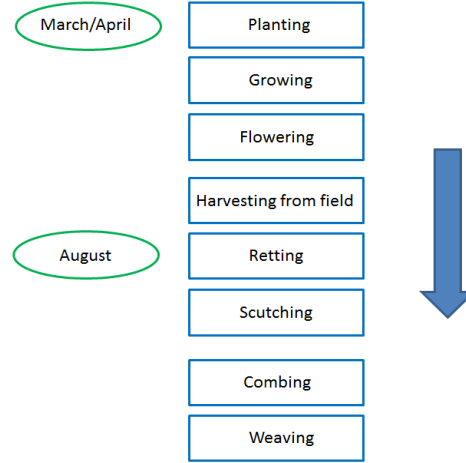


Figure 3.1: Flow chart depicting the production chain of flax fiber

posite) is dependent on the individualization of flax fibers and their quality [14]. This fiber individualization can be associated to the degree of retting and the processing conditions [20].

To characterize the process-induced-properties of fibers and overcome the fibers slippage, the IFBT was recently reported as a potential method applicable in the case of flax fibers [106]. According to this method, a priori assessment of the tensile properties of a UD composite and of its matrix is required. The effective Young's modulus and tensile strength of the fibers are back-calculated from the properties of the UD composites and of the matrix using micro mechanical models such as the rule of mixture. In this context, two assumptions should be satisfied. From the mechanical point of view, the matrix should have a high ductility to guarantee higher failure strain than the fibers. From the processing point of view, a good impregnation quality with a limited content of residual voids is required. Based on collaborative work between five laboratories, a comparison between back-calculated elastic moduli indicated that the IFBT method was more efficient than elementary fiber tests [106]. However, no clear reasoning was provided to explain the scattering of the results for tensile strength [106].

A non-extensive literature review indicates that the variability of the tensile strength of natural fiber composites can be related to different parameters which can be classified into three major categories [112]. The first category encloses the parameters affecting the intrinsic characteristics of flax fibers such as the change in cross-section due to swelling caused by resin absorption, moisture absorption, or due to shrinkage caused by desorption. Elevated processing temperature (higher than 180 °C) can also cause a degradation of the mechanical properties of flax fibers [77, 113, 114], and a change in the microfibrils angle [43, 115]. The second category is related to the parameters which can influence the

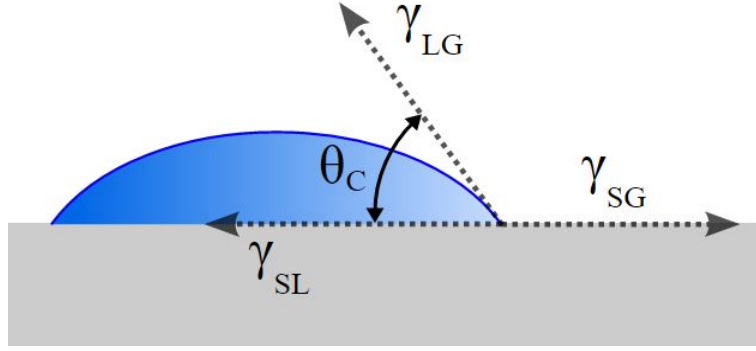


Figure 3.2: Schematic of a liquid drop wetting a solid substrate with

mechanical properties of the matrix such as the curing conditions in the case of thermoset matrix composites by affecting the cure kinetics and the activation energy of the cross-linking reactions [116]. The third category is mostly related to the parameters affecting the interfacial bonding between the fibers and the matrix. Four principal mechanisms, in general, explain interfacial bonding between natural fibers and matrix: molecular inter-diffusion, electrostatic adhesion, chemical bonding, and mechanical interlocking [91, 117]. The predominant bonding mechanism in the case of untreated flax fibers is the mechanical interlocking. The interface forms by a mechanical anchoring of the matrix on the rough and non-uniform surface of the external cell-wall of the flax fibers [1, 118]. Also, surface fiber treatments such as alkali or silane treatments can help to produce free radicals on fiber surface which can interact with matrix molecules by enhancing chemical and inter-diffusion bonding mechanisms [119, 120].

Physical adhesion is dependent on the surface energies of the matrix and the fiber. A good interaction is obtained when the matrix and fiber have a low contact angle. The following equation describes the wetting (See Figure 3.2)

$$\gamma_{SG} = \gamma_{SL} + \gamma_{LG} \cos \theta_c \quad (3.1)$$

where γ_{SG} is the force tending to spread the liquid and γ_{SL} is the force tending to pull it into a drop. Good wetting is obtained when the contact angle (θ_c) approaches zero which is usually achieved when there exists a chemical similarity between matrix and fibre.

Several types of physical treatments exist to improve the wettability of fibers. The most used ones for fibers are the cold plasma and the corona treatments. In the cold plasma treatment, fibers are exposed to plasma (partially ionized gas) which makes their surface more reactive without affecting their bulk properties [117]. The corona treatment is based on the discharge that occurs when there is a localized electric field gradient on the surface, which in return causes the ionization and electrical breakdown of the air near the fiber surface. The polarity of the surface is increased during treatment by introducing

polar functional groups such as hydroxyl groups. This treatment is not limited to natural fibers, and Calgar et al. [62] applied this for glass fibers to increase the wettability.

Chemical adhesion is obtained by chemically bonding the fiber and the matrix. It can be done by introducing a coupling agent as a ternary reactant to form bonds between the hydrophilic fiber and the hydrophobic matrix. The chemical treatment can be performed on either the fiber or the matrix material. A commonly used treatment in flax-polypropylene (PP) composites is the addition of maleic anhydride (MA) to the PP to increase wetting and adhesion. The MA forms a covalent bond between the anhydride group of the MAPP (hydrophobic PP) and the OH group of the cellulose (hydrophilic flax). A series of chemical treatments are also applied to flax fibers, such as acetylation, mercerization, or silanization. With the alkali treatment, also known as the mercerization process, cellulosic fibers are treated with sodium hydroxide (NaOH), which aims at removing the hydrogen bonds. The addition of NaOH to flax fiber helps the ionization of the hydroxyl group to the alkoxide [121]. This process directly influences the composition of cellulose, the degree of polymerization, and the dissolution of lignin and hemicellulosic compounds. Indeed, the alkaline treatment not only makes the natural fiber less hydrophilic, but it also removes the impurities and certain quantities of waxes and pectin. As a consequence, the fiber surface becomes more uniform while the surface roughness increases resulting in increased mechanical interlocking and fiber-matrix adhesion [122]. Even from a processing point of view, this treatment was proved to be efficient because it decreased the resin infusion time when compared to untreated fibers [48].

Hence, there are several variables to be considered before the characterization of flax fibers. As stated earlier, the composites themselves exhibit different properties depending on their processing method. Thus, in order to validate the feasibility of IGBT method to characterize tensile properties of flax fibers, the parameters which affect the fibers should be ruled out. With respect to flax fibers themselves, the fiber treatment highly affects the fiber matrix adhesion and it would be of best interest to consider untreated fibers as it would be a humongous task to characterize every possible treatment, which is out of the scope of this study. Secondly, the manufacturing process should also be consistent and reproducible. Hence, compression molding was selected to be the best option, because the processing parameters to produce a high-quality composite was already investigated by Cadu et al. [105]. It was stated that the most critical parameters affecting the mechanical properties of composites processed using the thermo-compression process are fiber conditioning, pressure level, cooling speed, mold exit temperature, and post-curing duration [105].

To our best knowledge, the influence of some other parameters such as the curing temperature, and the curing duration have not been investigated. The current study

focuses on the influence of the cure temperature and duration for unidirectional (UD) flax composites manufacturing on the back-calculated effective properties of an untreated flax tape according to the IFBT method. UD flax fiber composites were fabricated by hand layup and isothermal compression molding according to four different curing cycles. Firstly, the impregnation quality was assessed to verify the assumptions of the IFBT method. Secondly, the mechanical tests were conducted on composite specimens and neat matrix to back-calculate their tensile properties. Finally, microstructure analyses were conducted to explain the causes of the scattered values of the tensile strength of flax fibers. Particular attention was paid to the fracture mechanisms and the interfacial quality to point out the modification of the interfacial bonding.

3.2 Materials

Unidirectional flax-fiber tape FlaxtapeTM110 (Lineo, Belgium) having an areal weight of $110g/m^2$ was used as reinforcement. The UD flax fibers within the tape were maintained aligned by the reactivation of their natural pectin cement without application of any additional surface treatments. To impregnate the flax fibers, an epoxy resin Prime-27 (Gurit, Switzerland) was used. As recommended by the supplier, the resin was mixed with a hardener Prime-20 (Gurit[®], Switzerland) concerning a stoichiometric ratio of 100:28. This resin has a relatively low viscosity (265-285 mPa.s at 25°C), low exothermic reaction during the cross-linking reaction and limited shrinkage [123].

3.3 Manufacturing of UD composites

UD composite plates were manufactured using hand-layup process followed by isothermal compression molding. Neat epoxy plates and unidirectional composite laminates with 13 plies ($[0]_{13}$) were prepared according to four different manufacturing cycles. Each cycle comprised five consecutive steps: cutting (1), drying (2), hand-layup (3), isothermal compression (4) and post-curing (5) [Figure 3.3].

In the hand-layup process, dry UD flax tapes which had been dried at 60 °C for 14 hours, were placed in a rectangular mold with dimensions $270 \times 40 mm^2$. To avoid the increase of the resin viscosity during the impregnation process, the mold was also preheated to the same temperature as the curing temperature. Then, the resin mixture was gently applied by a roller on a dry fiber ply, and another dry fiber tape ply was put on this resin layer in the mold. This procedure was repeated until the total number of plies was reached. Subsequently, the impregnation of fibers by the resin was induced by the upper mold closing. In this study, the differences between these cycles were limited

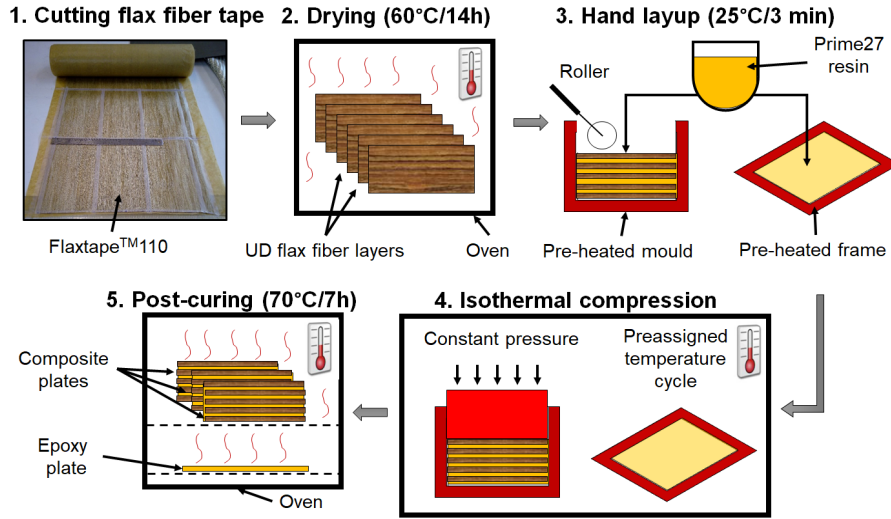


Figure 3.3: Schematic of manufacturing steps

to a change of the duration and temperature of the isothermal compression step in the aim of enhancing the impregnation quality by decreasing the viscosity and reducing the curing time of the matrix. The process parameters were selected based on trial-error tests to measure the gel time of the used epoxy during isothermal curing carried out at 25, 60 and 80°C referred to as the “RT”, “60” and “80” cycle respectively. A second cycle at 80°C (“80_S” cycle) is conducted with a reduced consolidation duration of 20 minutes. To ensure the complete cure of the resin, post-curing step was adopted in a temperature regulated oven. The parameters of the manufacturing cycles are provided in Table 3.1. The composites were cooled under natural convection.

Cycle Reference	Temperature (°C)	Duration (min)
RT	25	1020
60	60	80
80	80	40
80 _S	80	20

Table 3.1: Isothermal cure parameters

3.4 Characterization

3.4.1 Differential Scanning Calorimetry analysis

In order to gain more insight into the cure kinetics of the epoxy during isothermal compression step and post-curing, isothermal DSC measurements were conducted at 60, 70 and

80°C. Measurements at 25 °C were not considered because their corresponding isothermal compression duration was too long, viz. 17 hours. Samples of 5 to 10 *mg* were extracted from the freshly mixed resin at 25°C and encapsulated in aluminum pans. The average duration from the start of the resin/hardener mixture to the start of each isothermal DSC measurement was fixed to 15 minutes. Each measurement sequence comprised a temperature ramp of 100°C/min from 25°C to the target temperature which was then maintained for 90 minutes to guarantee a total cure of the samples. This temperature ramp helped to achieve the target temperature faster by preventing the reaction of epoxy during heating. Dynamic DSC measurements were conducted to measure the glass transition temperature (T_g) of the post-cured epoxy in the cured neat matrix and composite plates. Samples of 10 to 12 mg were exposed to two successive temperature sweeps between 25°C and 140 °C at 10 °C/min. All isothermal and dynamic DSC measurements were conducted on the same differential scanning calorimeter (DSC1, Mettler Toledo) and under a nitrogen atmosphere.

3.4.2 Laminate quality assessment

Out-of-autoclave manufacturing of laminate composites is known to generally induce residual void contents. Thus, to evaluate the void content of the manufactured composite plates, density measurements and SEM analyses were considered.

Density measurements

The density of the composite samples was measured using Archimedes principle. Two samples of rectangular geometry 20 × 40 mm² were extracted from each composite plate to measure the density of composites. The thickness of the samples was measured at each test. Dry mass (M_{air}) and immersed mass ($M_{ethanol}$) were measured using a micro balance (Mettler AE160) with an accuracy of 10⁻⁴g. Ethanol with a density of 0.789g/cm³ (Ethanol) was used as an immersion liquid. The density and void content (V_ϕ) of the composite specimens were calculated by Equation 3.2 and Equation 3.3, respectively.

$$\rho_c = \frac{M_{air}\rho_{ethanol}}{M_{air} - M_{ethanol}} \quad (3.2)$$

$$V_\phi = 1 - \rho_c \left[\frac{w_f}{\rho_f} + \frac{w_m}{\rho_m} \right] \quad (3.3)$$

Where, ρ_c , ρ_m , and ρ_f are the densities of the composite, matrix (1.09g/cm³) and fibers (1.5g/cm³) respectively. w_m and w_f are the weight fractions of the matrix and the fibers respectively.

SEM observations

SEM micrographs based on secondary electrons were acquired using Joel Neoscope 6000 equipment. Microstructure arrangement within the thickness of the manufactured composite plates was observed at a lower magnification (x60) to detect residual voids and at (x800) to examine the fiber/matrix interface. The corresponding samples were extracted using a band saw then polished with alcohol-based lubricant, and finally, a thin layer of gold was sputtered. Complementary SEM analyses were also conducted after the tensile tests to examine fractured faces.

3.4.3 Tensile tests

All tensile tests were conducted at a uniform crosshead speed of 2 mm/min on an Instron 1185 machine which was equipped with a 10 kN load-cell and an extensometer with a gauge length of 50 mm. At least five composite and five neat resin samples were tested for each manufacturing cycle. The composite samples had a rectangular geometry of $250 \times 10 \text{ mm}^2$ whereas the neat resin samples were dog-bone-shaped as defined by the standard ISO 527-2. All the samples were conditioned at 23°C for 24 hours at a relative humidity of 50%.

3.4.4 Back-calculation of the tensile properties of fibers

The rule of mixture, as described in Equations 3.4 and 3.5, was used to back-calculate the tensile properties of UD flax tape from the properties of composites and of matrix.

$$E_f = (E_c - E_m((1 - V_f)))/V_f \quad (3.4)$$

$$\sigma_f = (\sigma_c - \sigma_m^*(1 - V_f))/V_f \quad (3.5)$$

where the subscripts f , m , and c represent the fiber, the matrix and the composite, respectively. As the epoxy used in this work is more ductile than the fibers, we can assume that the failure mechanism of the composite specimen is dominated by fiber breakage. Hence, it is necessary to calculate the stress in matrix at failure (σ_m^*) as the product $E_m \times \epsilon_c$, where ϵ_c is the failure strain of the composite. The application of such procedure relies on the assumption of perfect interfacial bonding between the fibers and the matrix and a limited void content.

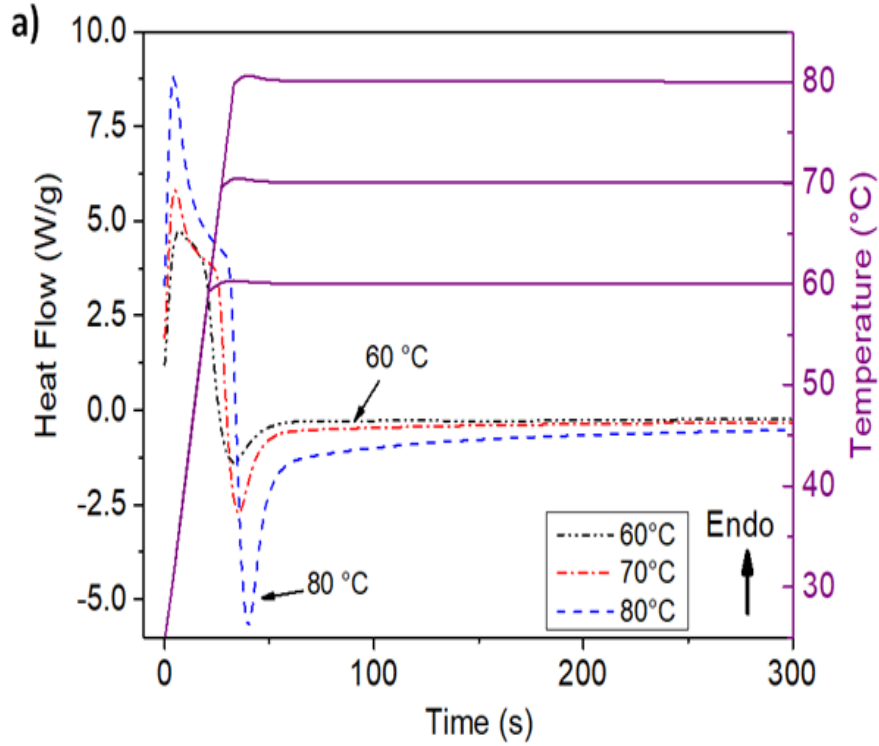


Figure 3.4: Isothermal DSC measurements: heat flow evolution of resin for each cycle

3.5 Effect of curing temperature on physicochemical properties

Figure 3.4 shows that the cross-linking reaction of the epoxy exhibits two different thermal regimes. The first regime takes place for the first 60 seconds and marks the initiation of the cross-linking reaction. By increasing the temperature of the isothermal plateau from 60 °C to 80°C, the reticulation reaction is accelerated as indicated by the increase of the corresponding areas of the exothermic peak, which are 13.4, 17.4 and 22.7 % for 60, 70 and 80 °C, respectively. The second regime is marked by a drop of the heat flow and a slower advance of the cross-linking reaction as the heat flow tends towards an asymptotic level. To gain more insight in the curing kinetics of the epoxy during the steps four and five of the manufacturing cycle (see Figure 3.3), the degree of cure $\alpha(t)$ was calculated by Equation 3.6

$$\alpha(t) = (\Delta H(t)) / (\Delta H_T) \quad (3.6)$$

where $\Delta H(t)$ is the heat of reaction at time (t), and ΔH_T is the total heat of the reaction of the epoxy mixture. To illustrate the change of cure kinetics during the isothermal compression, ΔH_T (1159.8 W/g) was obtained by integrating the heat flow measured over time during the isothermal DSC test conducted at 80°C. As illustrated in Figure 3.5 which shows the time evolution profiles of the cross-linking reaction, the epoxy cure

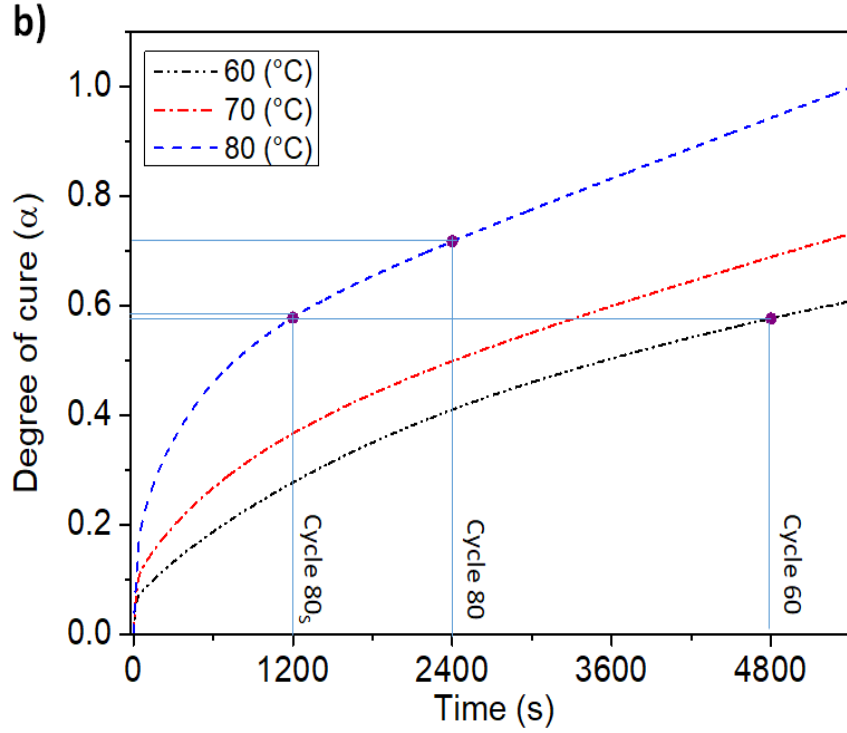


Figure 3.5: Time dependent evolution of degree of cure

cycles exhibit two-step paths of different kinetics. By considering the manufacturing cycle “80_s” as an illustrative example, the cross-linking reaction advances during the first step following the same profile of the cycle “80” until it reaches degree of cure of 0.58 at the end of the isothermal compression step (i.e. 1200 s). During the second step, viz. the post-curing operation, the advance of the cross-linking reaction follows the same curing rate as the cycle “70” (i.e. the same slope in Figure 3.5) until it reaches the total cure of the matrix (i.e., $\alpha \approx 1$). The relative degrees of cure at the end of the isothermal compression step for the cycles “60” and “80” are 0.58 and 0.72, respectively. The glass transition temperature (T_g) values obtained from the dynamic DSC measurements also confirmed a high cross-linking level following the two-step curing cycle. All the glass transition temperatures of the neat matrix range between 71.5 and 78.2°C (determined using tangent method) which is higher than the reference T_g of 69.4 °C indicated by the epoxy supplier (see Table 3.2). At least 3-4 samples have been tested to be sure of the obtained value. Moreover, the cure kinetics according to the cycle “80” seems to be as efficient as the cycle “60” in spite of its shorter curing duration. The increase in T_g values could be due to the decrease in the activation energy of the system thereby allowing higher cross-link density and resulting in higher T_g [124]. Similar results of the T_g values which ranged between 75.2 and 82.5°C, can be also verified from the composite samples.

T_g levels of the composite samples were higher, however, than those of the pure resin

Cycle	Matrix	Composite
RT	71.5(± 0.6)	75.2(± 0.7)
60	78.0(± 0.6)	79.7(± 0.5)
80	78.2(± 0.5)	82.9(± 0.8)
80 _S	75.5(± 0.8)	75.2 (± 0.8)

Table 3.2: Glass transition temperatures of neat epoxy and composites

samples (see Table 3.2). The increase of T_g values was limited to 5.2, 2.2 and 6.3 % for the cycles “RT”, “60” and “80” respectively. In the literature, a few studies have indicated such an increase of T_g values between 10 to 27 % after the addition of natural fibers [125–127]. The actual cause responsible for T_g change has not clearly been explained in the literature, and more investigations are still required to verify some of the following assumptions. The increase of T_g can be hypothetically attributed either to a reduction of the activation energy of the cross-linking reactions or to an enhancement of the thermal conductivity between the tooling and the core of the matrix due to the presence of reinforcements which is usually in the case of synthetic fibers [128, 129]. It could also be induced by an increase of the ratio of some functional groups at the surface of the natural fibers which may enhance the chemical bonding between the fibers and the resin molecules, therefore, restricting the movement of polymer chains. The latter cause seems to be more probable as the natural fibers have low thermal conductivity. Nevertheless, the same T_g value for the resin and the composite samples processed by the cycle 80_S requires more investigations to verify that assumption.

3.6 Qualitative and quantitative assessment of residual voids

The density measurement results presented in Table 3.3 indicate that the manufacturing cycle composed of hand-layup and isothermal compression molding guarantees good controls of the fiber volume fraction around $51 \pm 2\%$ and of fiber distribution with the absence of resin rich zones as shown by the SEM micrographs in Figure 3.6. Moreover, the increase of the curing temperature decreases the average void contents which correspond to 1.93, 1.67 and 1.60 % for the cycles “RT”, “60” and “80”, respectively. At the same curing temperature, i.e. 80 °C in this case, the increase of the curing duration decreases the average void content (cf. the cycles “80” and “80_S”). Nevertheless, the scattering of void contents highlights that the reproducibility of high-quality impregnation (i.e. void content $< 2\%$) is limited. Considering the fiber reinforcement drying and the resin de-

Cycle	Plate Index	Fiber mass(g)	Sample thickness (mm)	Fiber volume fraction (%)	Void Content (%)
RT	1	17.7	1.7	52	1.8
	2	18.2	1.8	51	1.9
	3	18.1	1.8	51	2.1
60	1	17.5	2.0	53	1.4
	2	17.4	2.0	51	2.2
	3	17.0	2.0	52	1.4
80	1	17.8	1.7	49	1.5
	2	18.0	1.7	51	1.2
	3	17.7	1.7	51	2.1
80 _S	1	18.4	2.0	50	2.3
	2	17.8	1.9	51	2.2
	3	17.1	2.0	53	2.6

Table 3.3: Fiber mass, fiber volume fraction and residual void content of composite plates

gassing before the molding process, this limitation seems to be related to the intrinsic structure of the flax preforms such as distorted or fractured technical fibers which may potentially trap air pockets during hand-layup and the isothermal compression steps, as shown in SEM images in Figure 3.6 [130].

Alongside with voids, Figure 3.6 shows the presence of a significant amount of macro-scale (x60 magnification) cracks. These cracks are supposed to be induced by the SEM samples polishing which leads to the coalescence of mesoscale (x240 magnification) cracks in zones of the high plasticity of the matrix with interfacial debonding. Even if these meso and macro-scale cracks are not directly induced by the manufacturing process, their presence can provide an indication about the quality of the interfacial bonding. Figure 3.6b shows that for a sample prepared by the cycle “*RT*”, macro-scale interfacial debonding between the matrix and the technical flax fibers exhibits a total separation between the matrix and the fibers without altering the external cell-wall of the technical fibers. At higher temperatures (60°C and 80°C), however, similar meso-scale debonding cracks seem to be associated with the partial separation of the outer layers of technical fibers from the matrix because the cell-walls are partially torn off from the technical fibers. Such meso-scale SEM observations indicate an enhancement of the interfacial bonding between the matrix and the outer cell-walls of some technical flax fibers with the increase

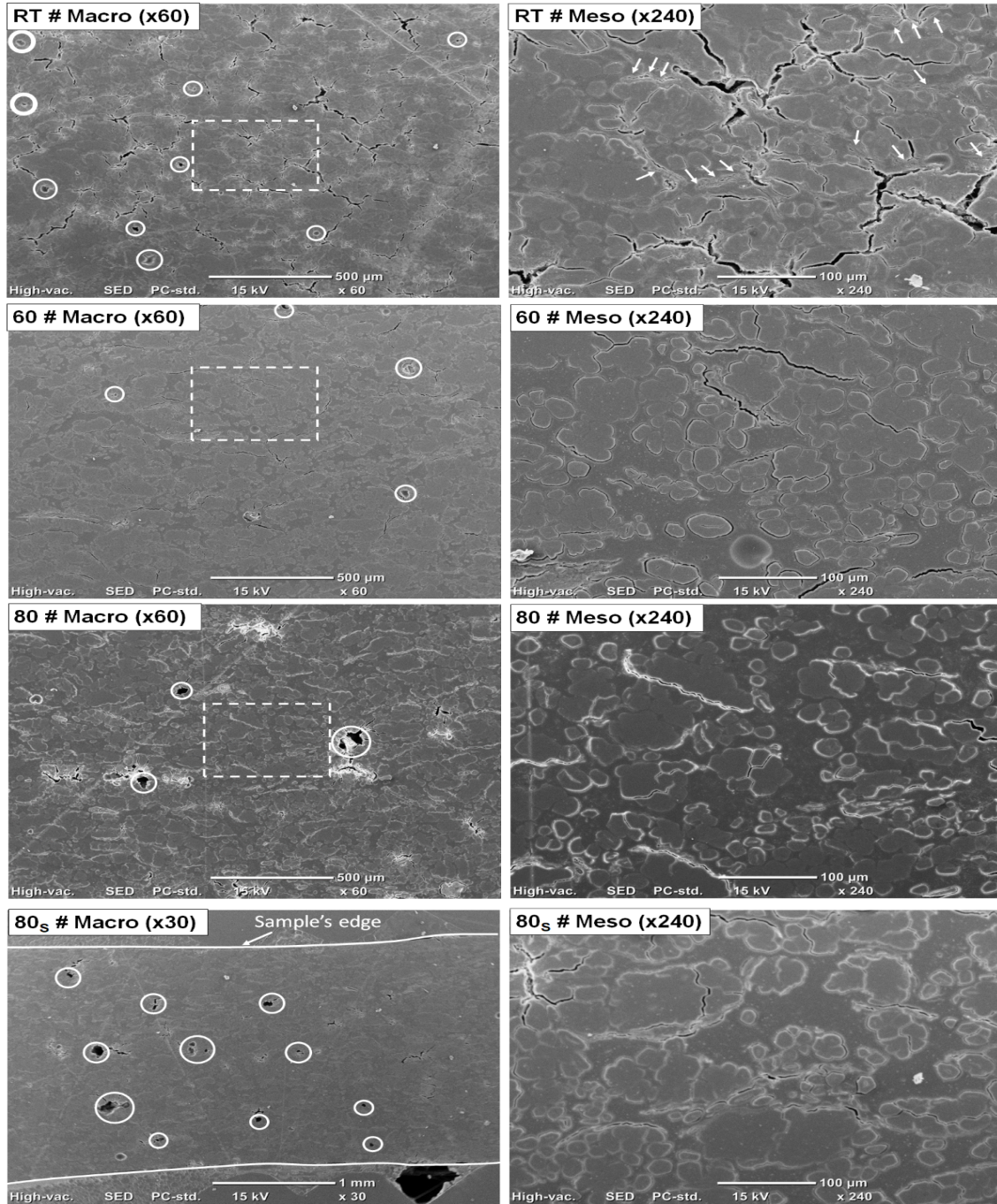


Figure 3.6: Micro structure of UD composites at two different magnifications (x60 on left and x360 on right)

of temperature.

As described previously, interfacial bonding between natural fibers and epoxy is in general classified into four principal mechanisms: molecular inter-diffusion, electrostatic adhesion, chemical bonding and mechanical interlocking [91, 131]. Because the fibers of flax tape used in this work were not subjected to any surface treatments, the mechanical interlocking mechanism is predominant. This mechanism corresponds to a mechanical anchoring of the resin on the outer surface of the flax fibers. As reported by Le Duigou et al.[132] working on laser confocal microscopy measurements, the mean penetration lengths of an epoxy resin polymerized at 65 °C during 14 hours can reach up to 1.7 μm and 2.2 μm for Hermes and Electra flax fibers, respectively. By increasing the impregnation temperature, the viscosity and contact angle of the epoxy resin decrease and induce an increase in the wettability of the flax fibers, and thus better mechanical interlocking can be achieved [133, 134].

3.7 Variation of tensile properties of composites with cure cycle

Figure 3.7 shows the typical stress-strain curves of flax-epoxy composite samples prepared by the manufacturing cycles presented in Table 3.1. It can be noticed that the curves include two slopes which are the first linear-elastic region between 0% and 0.1 % of strain, followed by a strain softening region between 0.2 % and 0.3 % of strain. The point of slope decrease is known as the knee-point, and it is commonly observed in stress-strain curves of flax fiber composites. According to the literature, the knee-point is the results of opposite effects. On the one hand, it marks the initiation of strain softening mechanism which is notably related to the visco-elastic or visco-plastic behavior of the elementary fibers composing the technical flax fibers of the tape or to the failure of the pectin-rich regions in-between the elementary fibers causing them to slide. On the other hand, the increase of tensile load induces the re-orientation of fibrils of the secondary wall of elementary flax fibers which causes a strain hardening effect [10, 135]. Moudood et al. [2] have indicated that this knee-point was dependent on the initial moisture content of fiber preforms and an increase of the moisture content caused its shift towards lower stress levels.

Two elastic moduli (referred to as E_1 and E_2) were calculated within the strain range of 0-0.1% and 0.3%-0.5% as suggested by Bensadoun et al.[106]. Theoretically, E_1 corresponds to Young's modulus, and E_2 corresponds to the stabilized elastic modulus following the stabilization of the intrinsic non-linear behavior of flax fibers. The average values of E_1 , E_2 and the tensile strength of the composite as well as the neat matrix samples, are presented in Figures 3.8 and 3.9. The tensile properties were greater in the case of

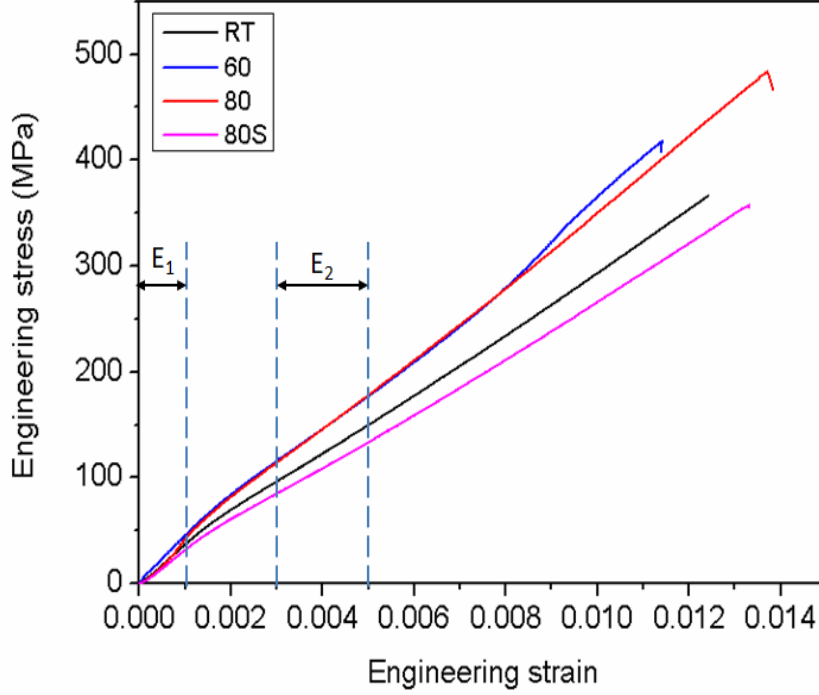


Figure 3.7: Stress-strain curves of UD composite samples

specimens obtained by the cycles “60” and “80” than by the cycles “RT” and “80_S”. The experimental results clearly show that the tensile properties of composites are dependent on the manufacturing cycle. From the cycle “80” to “80_S”, the tensile strength and the moduli E_1 and E_2 of composite have decreased by 23.6, 20.2 and 19.7%, respectively. The origin of such decreases in the tensile properties is directly linked to the imposed dwell time under the pressure as the other process parameters were maintained constant. The decrease in the dwell time of the isothermal compression from 40 to 20 minutes may affect some mechanisms which can alter the interfacial bonding, such as the advancement of the resin curing and the penetration of the matrix into the cell walls of flax fibers.

The effect of the resin curing on the interfacial bonding can be excluded from the tensile test results of the matrix and of the composite samples manufactured by the “60_S” and “80_S” cycles. Indeed, the similarity of the degree of cure (i.e. 0.58; see Section 3.5 and Figure 3.5) at the end of step 4 for both manufacturing cycles, has resulted in a very small difference in the tensile properties of the neat matrix samples obtained by the “60” and “80_S” cycles (see Figures 3.8 and 3.9). Given that the average moduli E_1 and E_2 are almost the same for the “60” and “80” cycles, the hypothesis of the matrix penetration into the cell wall of flax fibers is more convincing. Nevertheless, the similar values of E_1 and E_2 for the “60” and “80” cycles indicate that the resin penetration did not affect the stress softening region of the tensile behavior of the composite samples. Thus, resin

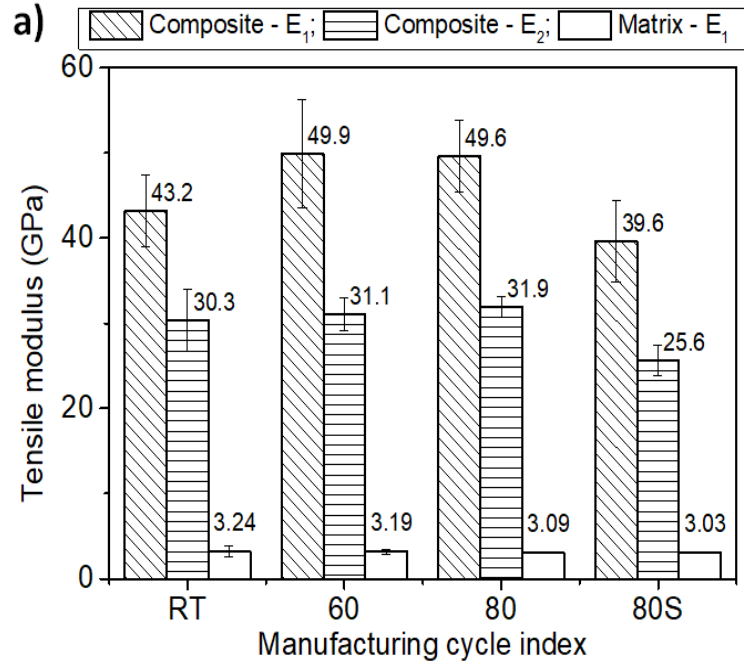


Figure 3.8: Tensile modulus of UD composites and neat matrix

penetration did not affect the stiffness of the elementary fibers, which is governed by hardening of pectin, gradual crystallization of cellulose present in fibers, etc.[136]. The increase of the tensile strength of composite by 7.4 % in the case of “80” cycle compared to the “60” cycle also implies that the deep resin penetration enhanced by lowering the resin viscosity at higher temperature strengthened the mechanical interlocking between the interface between the external cell wall of technical fibers and the matrix as stated in the previous section. The same principle can apply to explain the difference between the “80” and “80_S” cycles. Even at the same temperature, viz. 80°C, the time for resin penetration at the “80_S” cycle was not sufficiently long and the mechanical interlocking effect was smaller than that in “80” cycle. For the “RT” cycle, the small tensile moduli is correlated with the weak mechanical interlocking as described in Section 3.6. It has been widely known that elementary plant fibers have porous structures and absorb certain liquid through the fiber cell walls. As the liquid is absorbed into plant fibers, the fibers swell. Nevertheless, it is still difficult to directly observe the resin penetration into the fiber cell walls. Given the small thickness of cell walls and tiny pores on the surface of flax fibers ranging between 16 to 38 angstroms, intensive characterization studies are required for a comprehensive analysis [132].

Figure 3.10 shows the fractographs of transverse fracture surfaces where the predominant failure mechanisms are supposed to be dependent on the manufacturing cycle. In fact, for the sample of the “RT” cycle (see Figure 3.10a), matrix cracks between technical fibers can be observed along with the presence of fractured fiber bundles and the neat

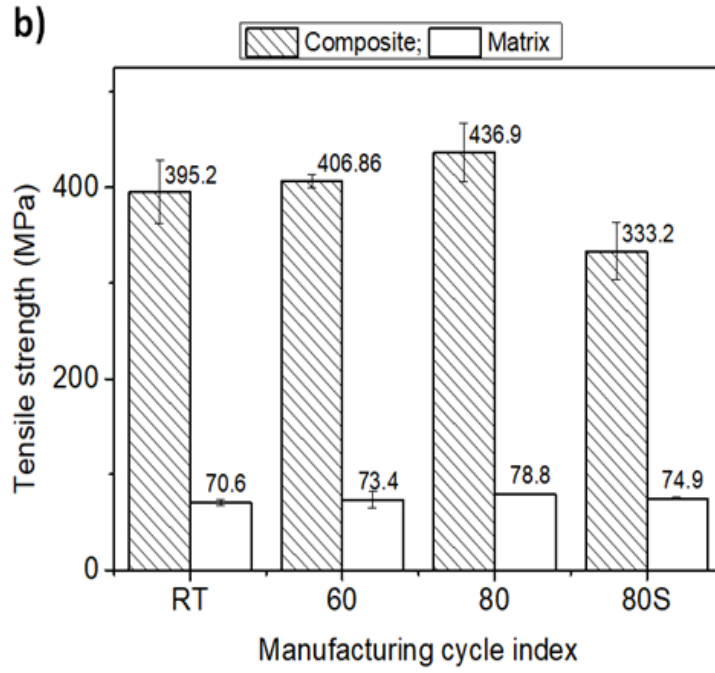


Figure 3.9: Tensile strength of UD composites and neat matrix

surface of single fibers which were pulled out. This observation indicates a relatively weak interfacial cohesion between the matrix and the fibers. In the case of the samples prepared by the “60” cycle (see Figure 3.10b), we can observe elementary fibers decohesion and significant longitudinal breakage of technical fibers. It is clear that even when the fibers decohesion takes place, there is a significant amount of matrix surrounding the fibers. Also, the fractured surface of “60” samples show small fiber-like structures around the failed fiber regions. These thin structures are the outer cell-walls the fibers which were peeled off during the failure of the composites. In the case of “80” cycle, the presence of residual voids can be observed and the fracture surface shows a significant amount of peeled fiber cell walls (see Figure 3.10c), which implies a strong mechanical interlocking between the fibers and the matrix. This is also coherent with the observations made by Le Duigou et al.[132]. This proves the assumption of the improved mechanical interlocking. In Figure 3.10d, the decohesion between the matrix and flax fibers exhibits less peeling of cell walls than that of “80” cycle due to the high void content which was the precursor of composite failure.

The IFBT method was adopted to investigate the influence of resin curing cycle on the tensile properties of flax fibers. In Figures 3.8 and 3.9, it can be noticed that the properties of the composites exhibit significant changes according to the cure cycle, whereas the matrix properties remain constant. This implies that there is a significant change either in the properties of fibers or in the stress transfer between fibers and matrix. To understand these changes caused by the cure cycle, the back calculation of tensile properties of fibers

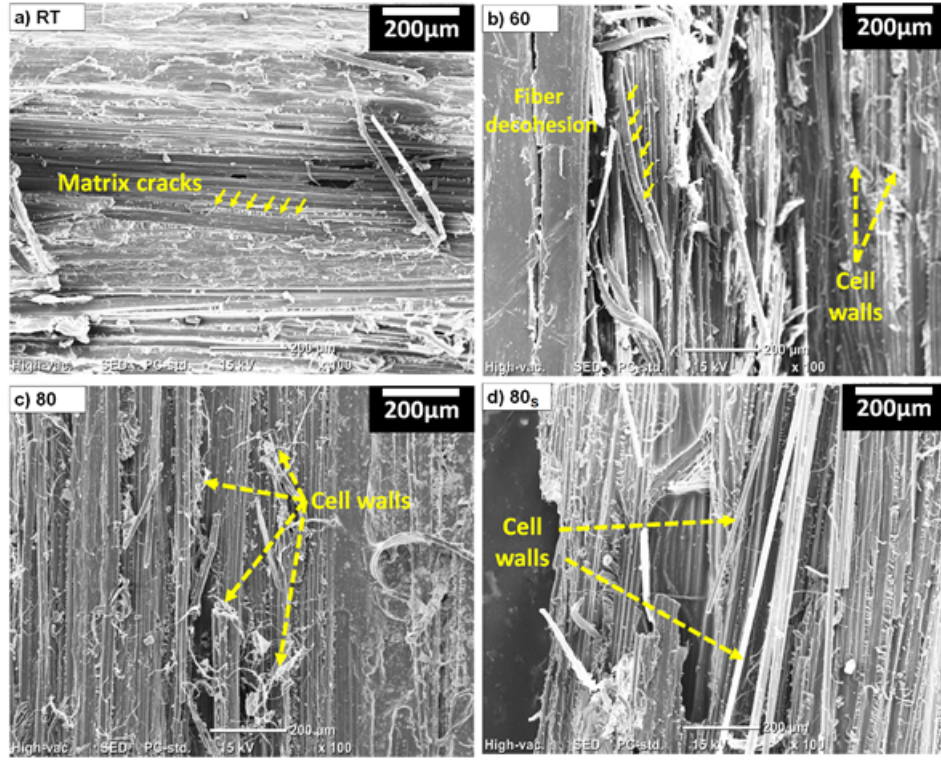


Figure 3.10: SEM images of fractured surfaces of composite samples

was performed. Conceding the assumptions of the rule of mixture such as perfect interfacial bonding between the fibers and the matrix and very low void content, a threshold of 2% void content was considered. Thus, the calculation of fiber strengths was only carried out for cycles "RT", "60" and "80". Based on the results obtained from ANOVA analysis (See Table 3.4), significant differences were observed only in case of tensile strength and E_2 . Figure 3.11 and Figure 3.12 show that the back calculated flax fiber properties by the IFBT method of the "60" and "80" cycles had maximum relative variations about 10.5% and 7.5% for strength values respectively. The fiber strength, in particular was the highest in case of "80" cycle. This difference of back-calculated strengths of fibers between the cycles "60" and "80" can be attributed to the change of interfacial bonding, as explained in the Section 3.6. This result suggest that the reliability of back-calculated tensile strength of flax fibers is dependent on the mechanical interlocking between matrix and flax fibers.

A comparison was made between the tensile strength data obtained in this work and the literature values in Figure 3.13 [8, 81, 85, 105, 113, 126, 137, 138]. It can be verified that the highest strength of the impregnated fibers is obtained by the cycle 80 adopted in this work. This implies that the impregnation process at 80 °C which increases the degree of mechanical interlocking of fibers and matrix, seems the most reliable method to improve the mechanical properties of flax composites even with the presence of a few

	Composite			Matrix	
Cycle	Tensile strength (MPa)	E1 (GPa)	E2 (GPa)	Tensile strength (MPa)	E (GPa)
RT	395.19 ± 32.96	43.22 ± 4.27	30.32 ± 3.63	70.61 ± 3.55	3.1 ± 0.63
60	406.86 ± 6.71	49.93 ± 6.33	31.08 ± 1.97	73.40 ± 8.45	3.19 ± 0.27
80	436.92 ± 30.41	49.60 ± 4.19	31.9 ± 1.236	78.85 ± 0.59	3.09 ± 0.04
80_S	333.22 ± 30.02	39.61 ± 4.79	25.63 ± 1.80	74.09 ± 1.30	3.03 ± 0.07
P-value	0.0045	0.024	0.0071	0.0413	0.1114

Table 3.4: ANOVA result for tensile properties of UD composites and matrix

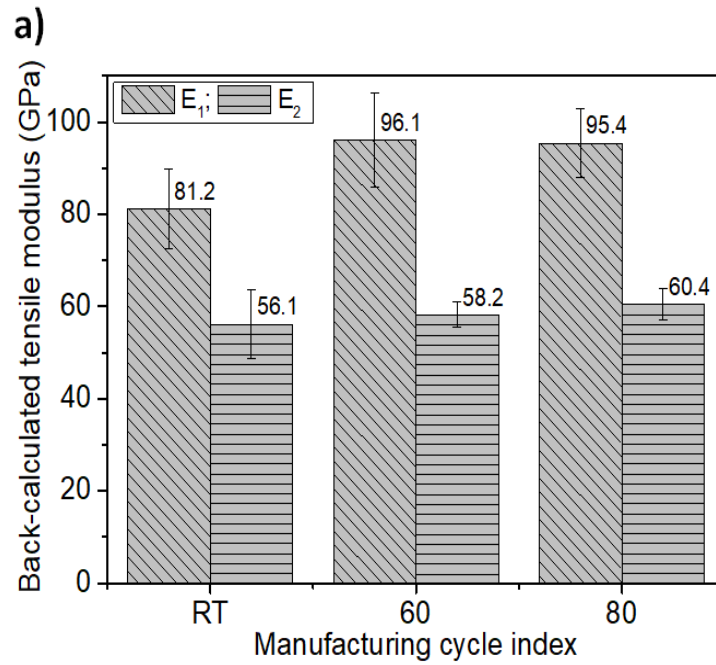


Figure 3.11: Back calculated tensile modulus of flax fibers

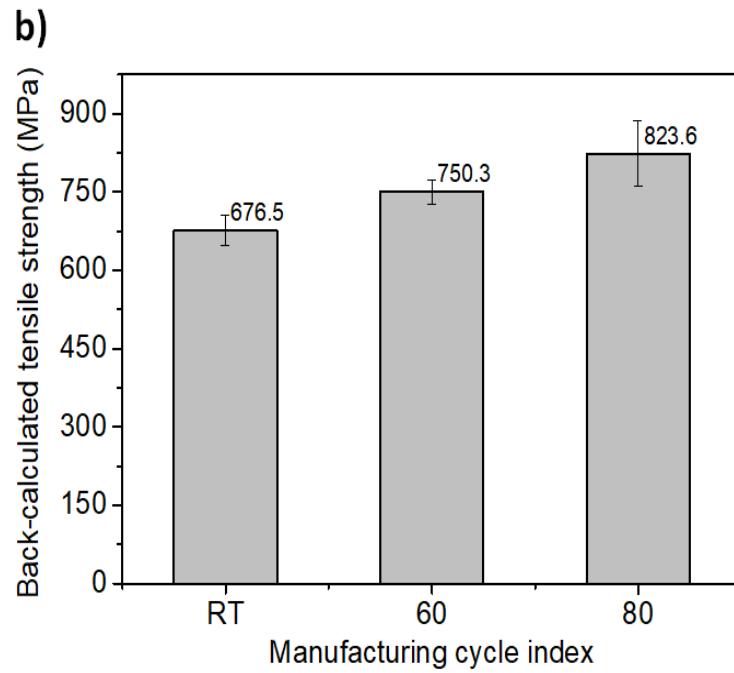


Figure 3.12: Back calculated tensile strength of flax fibers

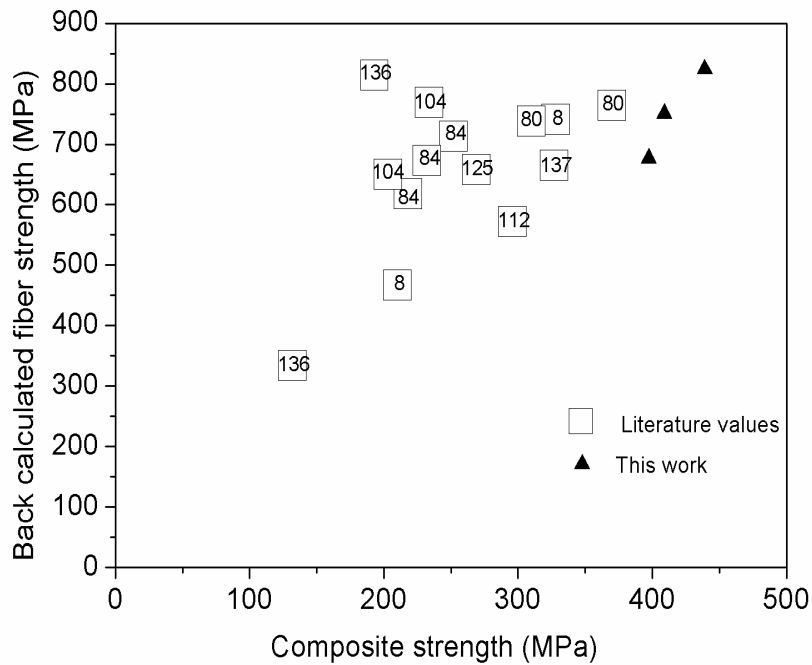


Figure 3.13: Comparison of composite strength and back-calculated fiber strength between literature and this work

residual voids. This also suggests that the reliability of back-calculation of fiber properties is dependent on the manufacturing process. Therefore, an optimum process cycle should be considered before characterizing the fiber properties, in particular tensile strength, which could otherwise lead to scattering in the results as presented by Bensadoun et al. [106].

3.8 Conclusion

The influence of manufacturing cycle on the mechanical properties of flax-epoxy composites was investigated. The quality assessment of composites was carried out by measuring the void content of the laminates. The void content was found to decrease with increase in curing temperature. It was reported that the void contents in all the cases except for the cycle “80_s” were smaller than two percent which might not significantly degenerate the mechanical properties. This satisfies the first requirement to use IFBT. The second hypothesis of the good interface was proved by SEM observations. The fractography images supported the hypothesis of resin penetration into fiber walls, because more cell-walls were peeled off for the sample of the cycle “80” indicating a good fiber-matrix interfacial adhesion. The curing duration under pressure also played an important role to determine the quality of composites even at the same curing temperature, e.g. 80 °C in this work. The influence of temperature on the physicochemical behaviors of both neat epoxy and composites was also examined by the measurement of glass transition temperature whose value was higher for higher temperature cycle in both the cases of neat epoxy and of composite. It should be also noted that the composite specimens exhibited a higher glass transition temperature than the neat epoxy. It was observed that the processing temperature had a substantial effect on the tensile behavior of the composites. A linear trend was noticed between the processing temperature and the tensile strength of the composite. This increase in the tensile strength of fibers was attributed to the enhanced resin impregnation into the fiber cell walls at higher processing temperatures, which was verified by fractographs. The decrease in the tensile properties were related to the improper curing and increased void-content of composites. The results of back-calculated properties clearly show the dependence on the cure cycle. It was shown that if IFBT is adopted to characterize fiber properties, special care should be taken in the selection of cure cycle. Otherwise the properties of flax fibers can be underestimated which was the plausible issue in the literature.

Chapter 4

Wettability characterization of flax fibers

4.1 Background

Wettability plays an important role because capillary pressure is the factor that drives the flow inside tows of fabric and governs the formation of microvoids. Incomplete wetting leads to entrapped air, which will provoke dry areas. Many researchers presented works on the study of capillary flows, and its influence on the formation of microvoids [118, 139–141]. Wettability of a material can be studied by characterizing the surface tension and contact angle with several test fluids. Knowledge of the surface properties of cellulose fibers is essential to understand the interaction of these fibers with polymer matrices.

4.1.1 Mathematical modelling

On surface energies, Young, in his essay on the cohesion of fluids [142], mentioned a mathematical model but not in an exact representation. Surface energy γ is a material property at an interface with another medium. In simple terms, surface energy or surface tension (for fluids) is the energy required to separate the atoms in a plane or along two different planes. In an ideal case where a liquid drop is placed on a smooth surface, the drop tends to minimize its surface as the molecules are pulled inwards, causing the surface to contract.

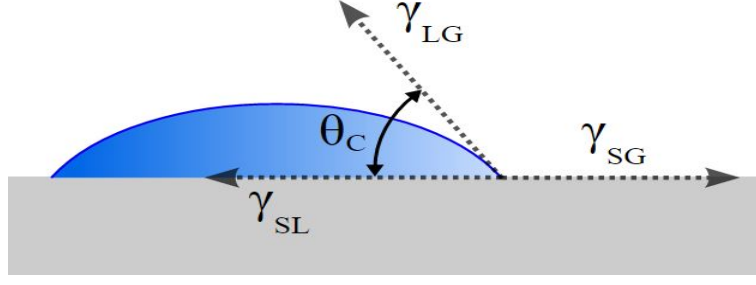


Figure 4.1: Schematic representing surface energies and contact angle

Solid and liquid surface energies determine the behavior of wettability, which is assessed quantitatively by a contact angle. The force equilibrium of the three surface tensions for a drop placed on a smooth and homogeneous solid surface derives the relation about the contact angle at the equilibrium point, which is defined by the relation of Young (Equation 4.1). The contact angle is the angle between the direction of the solid-liquid surface SL (tangent to the solid surface) and the vapor-liquid surface tension LG which is tangent to the outer surface of the drop, the apex of which is the SLG triple point. In Figure 4.1, a schematic of the contact angle is presented. The surface energies are represented along the line of contact where the three phases solid 'S', liquid 'L', and gas 'G' are presented. The contact angle is represented by θ_c . Mathematically, this can be represented as

$$\gamma_{SG} = \gamma_{SL} + \gamma_{LG} \cos \theta_c \quad (4.1)$$

Further, Equation 4.1 can be modified as $\gamma_S \simeq \gamma_{SV}$ and $\gamma_L \simeq \gamma_{LV}$

$$\gamma_S = \gamma_{SL} + \gamma_L \cos \theta_c \quad (4.2)$$

The wetting configuration (complete or incomplete) and the contact angle depend on the chemical nature of the solids and liquids and also on the morphology of the solid surface. It should be noted that Young's relation is only valid in the case of an ideal surface, which is smooth and chemically homogeneous in an equilibrium condition. In the real scenario where the solid has physical (the surface is rough) or chemical (its composition varies from point to point) defects, there is not a single contact angle. The equilibrium contact angle can take all the values comprised between a maximum, known as the angle of advancement or advancing contact angle θ_a and a minimum, known as the receding contact angle θ_r . This is translated into the inequality shown below.

$$\theta_a > \theta_e > \theta_r \quad (4.3)$$

The contact line will advance only if the contact angle exceeds θ_a and vice versa. Models to define an equilibrium angle in the case of a drop placed on a surface, depending on the

physical and chemical defects, are presented by [143–147]. Depending on the direction of the contact line, the receding or advancing front can be determined. Different models for such cases are provided in the literature [148–152]. The measurement of the contact angles is crucial to determine the surface energy of a solid (static contact angle) as well as the impregnation mechanisms by a liquid (dynamic contact angle). For the measurement of contact angle, there are several techniques available but are strongly dependent on the geometry of the system under study. The static drop method can be applied in the case of flat surfaces (Figures 4.2 and 4.3). Once deposited on a solid substrate using a syringe, with a camera and a goniometer, one can measure the contact angles at both corners and obtain an average apparent angle [153, 154]. If the drop is small enough, i.e., with a radius r smaller than the capillary length, the assumption can be made that the drop is spherical and hence the following geometric relation can be applied (Figure 4.2):

$$\tan\left(\frac{\theta}{2}\right) = \frac{h}{r} \quad (4.4)$$

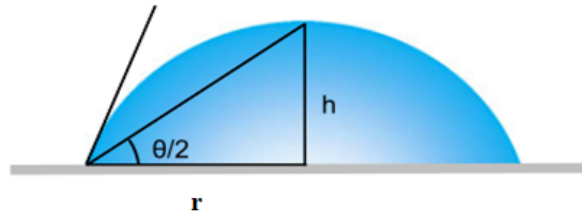


Figure 4.2: Representation of contact angle

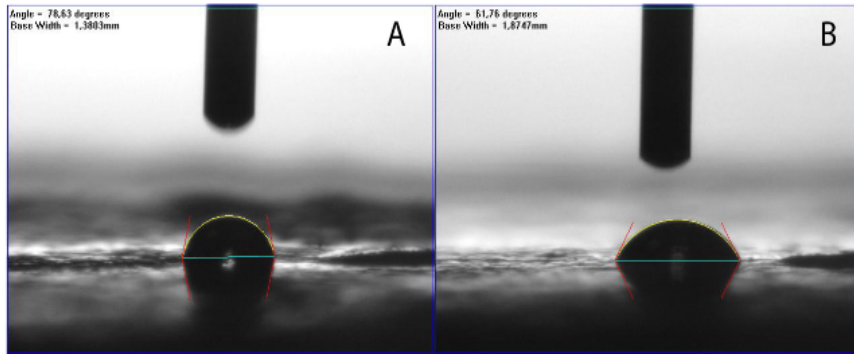


Figure 4.3: Observing contact angles using drop shape method on (A) Untreated Kraft fibers (B) Treated Kraft fibers

However, this method is difficult to implement in the case of thin filaments like fibers because the measurement of angles is not precise. This is due to the variation of the radius of curvature of the meniscus in the vicinity of the fiber. In this case, the drop will be axisymmetric, and other parameters can be measured in visual terms, such as the

length of the drop on the filament or the maximum radius of the drop from the axis of the fiber will differ from fiber to fiber. It should be noted that this procedure has been applied to fibers with diameters of 200 μm and bigger, whereas a natural fiber generally has a diameter at least ten times lower. Given the small dimensions of the system, the reliability and reproducibility of this method is therefore even lower than in the case of plane surfaces [155].

A vertical fiber plunged into a liquid has been studied, and a mathematical relationship was used to describe the profile of the meniscus to calculate the contact angle [156]. The meniscus has the topology of a catenoid $y = f(x)$ and the height H , to be measured visually for $x = r$ as shown in Figure 4.4 and is related to the contact angle in the James relation [115, 157, 158]

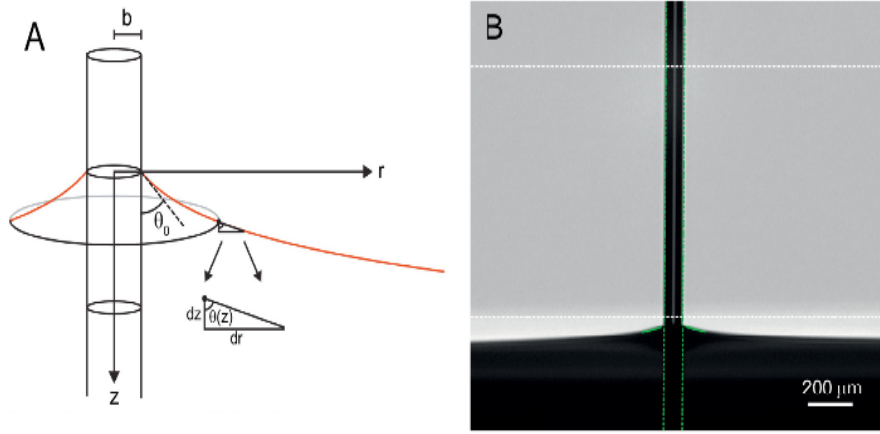


Figure 4.4: Meniscus on single fiber

$$H = r \cos \theta \left[\ln \left(\frac{4k}{r(1 + \sin \theta) - C} \right) \right] \quad (4.5)$$

where $C = 0.577$ and k is the capillary length.

Another method to measure contact angle is Wilhelmy's weighing method which is the most reliable technique. There is also feasibility to measure other parameters such as the wetting perimeter p and the liquid-liquid interfacial tension (Equation 4.6). It can be applied to most geometries (blades, tubes, powders, etc.) and different wetting regimes.

$$F_c = \gamma_{LV} p \cos \theta = mg \quad (4.6)$$

where F_c is the force recorded and m is the recorded mass of meniscus.

Using a tensiometer, consisting of an electronic microbalance, the mass m of the meniscus in contact with the solid to be tested is measured. Initial weight of solid is weighed (Figure 4.5 A-1). The container with the liquid whose surface tension γ_{LV} is known rises with a constant speed till the test sample comes in contact with liquid.

When a weight change is detected, the solid begins to sink into the liquid. This position is recorded and serves as a reference; From this position, the tensiometer measures the weight. The container continues to rise till the programmed immersion depth is attained. In this phase, the advancing contact angle can be determined (Figure 4.5 A-2). The container can remain in a fixed position for a time defined by the user, which would make it possible to determine a static angle (Figure 4.5 A-3), then it goes back down allowing to measure an angle of withdrawal (Figure 4.5 A-4) [153].

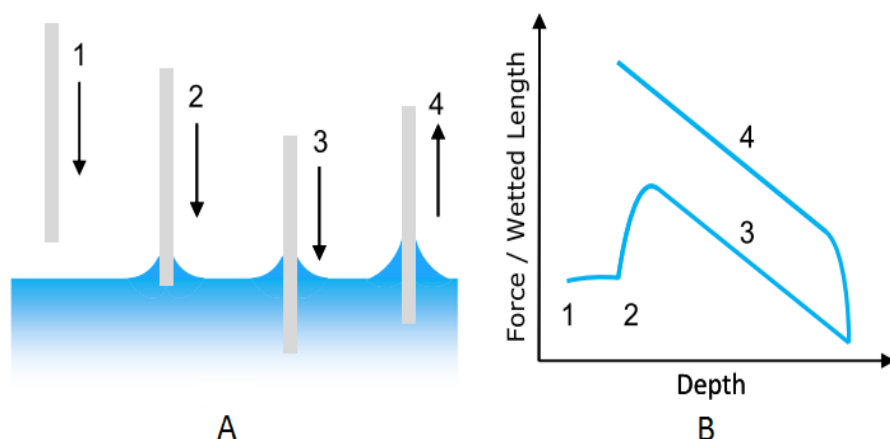


Figure 4.5: Illustration of advancing, static and receding contact angle measurements with Tensiometer

In the case of natural fibers, several factors affect the wettability measurements. The chemical composition of fibers differs from one type of fiber to another by variation in components mainly cellulose, hemicellulose, and lignin, and therefore their wettability is also different from one other. The variation in chemical composition is also found for the same type of fiber, as a function of time and place of harvest as well as of the fiber extraction method [20, 22, 119, 159]. Moreover, the morphology of natural fibers is much more complex than that of synthetic fibers. Surface irregularities must be taken into account, as well as their perimeter, which varies along the fiber. Perimeter variations cause variations in the weight of the measured meniscus and thus influence the determination of contact angles and surface energies. Moreover, natural fibers are also sensitive to moisture absorption, and phenomena of swelling or shrinkage of the fiber may also occur [160]. Nevertheless, the effect of liquid absorption on the natural fiber wetting has not been thoroughly investigated, whereas the influence of fiber swell was considered in the literature [161]. For example, the mass of liquid in the pores between the fibers should be obtained in the Washburn method. During a capillary rise experiment with natural fiber bundles, however, the liquid penetrates inside the individual fibers, i.e., liquid absorption, as well as flows in the pores between the individual fibers, i.e., capillary wicking. Thus,

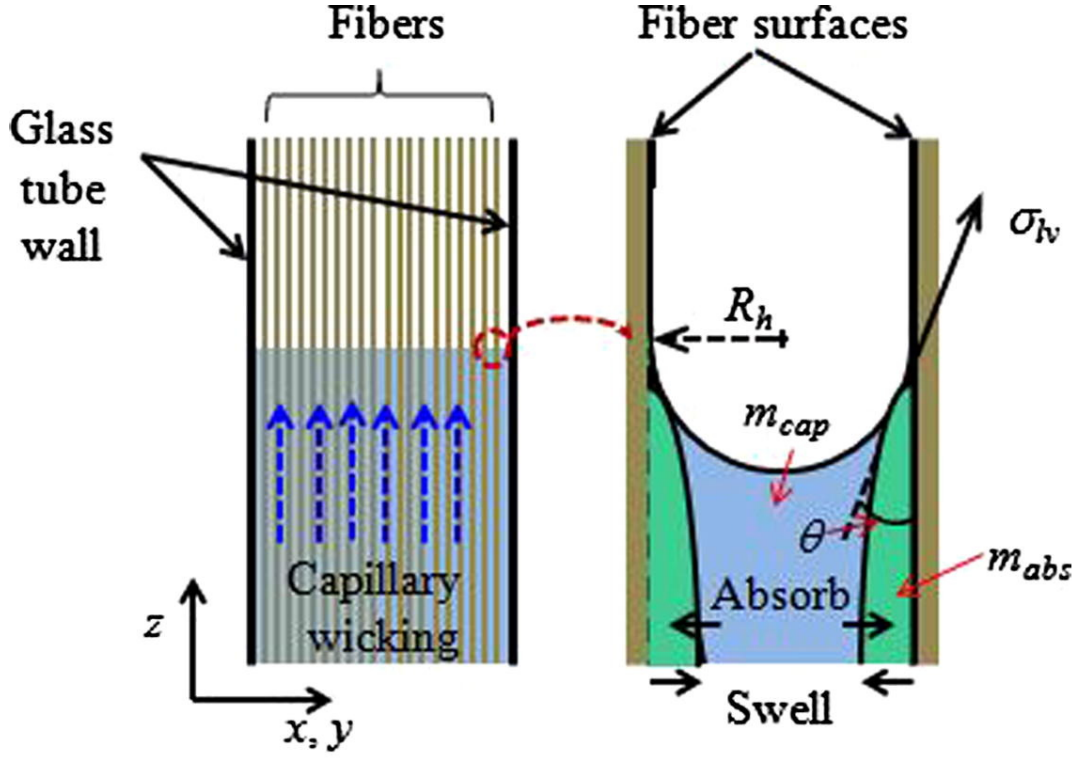


Figure 4.6: Schematic of the capillary wicking mechanism in swelling fibrous medium

the mass of the liquid measured by a tensiometer during the Washburn method is the sum of the mass of the liquid absorbed into the fibers and that imbibed between the fibers. As a matter of fact, the mass of the liquid imbibed in the pores between the fibers is required to characterize the wetting properties of natural fibers. Therefore, the mass of the liquid which does not stay in the pores between the fibers but penetrates into the fibers should also be considered in the momentum balance equation to evaluate the contact angle of natural fibers (See Figure 4.6).

For natural fibers, diameter D_f is usually initial diameter $D_{f,0}$ as the fiber swells with time. As handling single fiber is very tedious and difficult, the capillary rise method is more convenient and also depicts the real-time scenario. It is noted that the values of contact angles vary from tows to fibers. Mathematically, the capillary rise can be modeled by the momentum balance

$$\rho_L A(1 - V_f) Z \ddot{Z} = \lambda_{perimeter} \sigma_{LV} \cos \theta - m_{cap} g - \frac{\mu}{K} A(1 - V_f) Z \dot{Z} - \frac{1}{2} \rho_L A(1 - V_f) Z^2 \quad (4.7)$$

where ρ_L is the density of test liquid, A is the cross-sectional area of test specimen, V_f is the fiber volume fraction, Z is the vertical displacement, \dot{Z} is the vertical velocity and \ddot{Z} is the vertical acceleration, g is the gravitational acceleration, K is the permeability of a porous medium and m_{cap} is the mass of the liquid imbibed in the pores.

Ignoring the inertial and gravity terms, Lucas and Washburn [162] presented an ex-

pression for a liquid rise (h_{cap}) in a capillary tube with a pore radius R_c

$$h_{cap} = \sqrt{\frac{\gamma_L R_c \cos \theta}{2\mu}} \quad (4.8)$$

Bonsanquet [163] considered only inertial and viscous terms and presented an equation for capillary rise height as:

$$h_{cap}^2 = \frac{2b_1}{a} \left[t - \frac{1}{a}(1 - e^{-at}) \right] \text{ where } a = \frac{8\mu}{R_c^2 \rho_L}; \quad b_1 = \frac{2\gamma_L \cos \theta}{R_c \rho_L} \quad (4.9)$$

Fries and Dreyer [164, 165] only neglected the inertial term and presented the h_{cap} . It was also mentioned that the gravity effect must be taken into account as the rise height reaches 10% of the h_{max} .

Conventional models like Washburn's model, tend to overestimate the capillary rise of the media. Schuchardt and Burg [50] modified Washburn's model during swelling by assuming that the pore radius decreases linearly with time.

$$h_{cap} = \sqrt{\left(\frac{\gamma R_o \cos \theta}{2\mu} \right) \left[t - \frac{a_{sw}}{R_o} t^2 + \frac{a_{sw}^2}{3R_o^2} t^3 \right]} \quad (4.10)$$

Where h_{cap} is the height of capillary rise or wicking length, R_h is the hydraulic radius and R_o is the initial hydraulic radius. R_h is considered to be a linear function of time with a factor a_{sw} representing swelling.

$$R_h = R_o - a_{sw} t \quad (4.11)$$

In case of synthetic fibers or fibers which does not swell, ($a_{sw} \rightarrow 0$), the Equation 4.10 reverts to conventional Washburn's equation (Equation 4.8). Masoodi and Pillai [166] considered a modified Darcy's law by adding a factor of swelling to basic model and a sink term (S)

$$\nabla \cdot \langle V \rangle = -S - \frac{\partial \epsilon}{\partial t} \quad (4.12)$$

Considering a 1-D flow, above equation will take form of Darcy's equation which can be further solved to present an analytical model for wicking height can be written as :

$$h = \sqrt{\frac{2P_{cap}}{\epsilon_{fo}\mu} e^{(b-1)\frac{\epsilon_f(t)}{\epsilon_{fo}}} \int_0^t e^{(1-b)\frac{\epsilon_f}{\epsilon_{fo}}} K(t') dt'} \quad (4.13)$$

Where P_{cap} is the capillary pressure, ϵ is the initial porosity and $\epsilon_f(t)$ is preform porosity at time t and b is the absorption coefficient. For a special case when swelling rate matches the volumetric absorption rate (i.e, $b = 1$), the above equation can be reduced to

$$h = \sqrt{\frac{2P_{cap}}{\epsilon_{fo}} \int_0^t K(t') dt'} \quad (4.14)$$

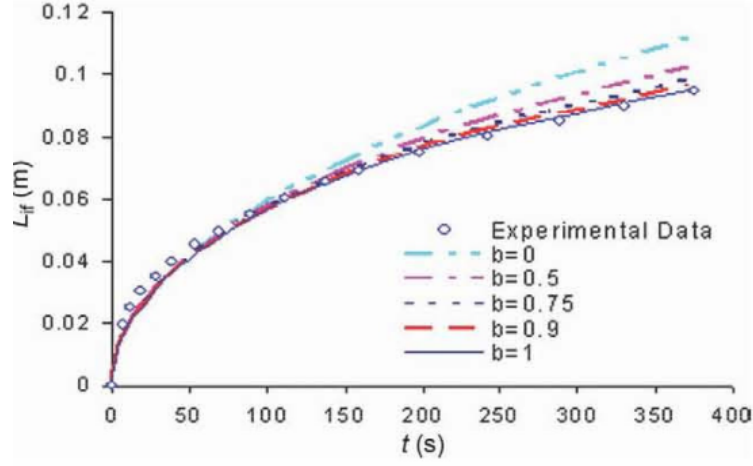


Figure 4.7: Wicking height with different values of b [161]

In the Figure 4.7 [166], we can observe that the change in the factor b can affect the estimation of wicking length. Although during the initial seconds, all the values tend to converge, the curves diverges in the long run.

Moreover, the same work was extended towards numerical modeling of capillary wicking where a control volume approach was used to implement both absorption and swelling based on Darcy's law [49]. Instead of measuring the capillary rise heights which can lead to errors, some authors [167, 168] suggested the tensiometric method where the mass gain in the specimen during wicking is linked to capillary pressure and rise height.

$$m^2(t) = \frac{2K\epsilon\rho_L^2(\pi R^2)^2 P_{cap} t}{\epsilon} \quad (4.15)$$

Where P_{cap} is capillary pressure which is represented in terms of tortuosity $[c\bar{r}]$ of fibers, porosity ϵ and permeability of fibers K . The capillary pressure is expressed as:

$$P_{cap} = \frac{c\bar{r}\epsilon\gamma_L \cos \theta_a}{4K} \quad (4.16)$$

θ_a is advancing contact angle and K is the permeability.

Two assumptions were considered for this model. The one is that liquid absorbed by fiber can be neglected. The second is that the fiber sample swells instantly after contact with test fluid, as in f_{sw} reaches its maximum value. These two assumptions overlook the fact that f_{sw} does not reach its maximum value instantly [1]. Also, it is widely stated that the wettability of fibers is dependent on the treatment of fibers [167]. It has also been stated that treated fibers have faster wicking and low contact angle.

4.2 Model development for capillary rise

The objective of this study is to incorporate both swelling and absorption behaviors in the same model for the capillary rise. A hollow tube filled with fibers can be regarded as a porous medium which is a pack of many capillary tubes. Thus, Washburn Equation can also be applied to the capillary wicking of liquid into a fibrous medium by defining an effective capillary radius. White defined an effective capillary radius ' r_{eff} ' as :

$$r_{eff} = \frac{2(1 - V_f)}{V_f \rho A} \quad (4.17)$$

Schuchardt and Berg proposed a modified Washburn Equation that takes into account the rate of swelling to predict the capillary wicking into a bundle of natural fibers [50]. In this model, the effective capillary radius in the porous medium can change from its initial value because of fiber swelling [169]. The long-term behavior of fiber swelling can lead to a reduction of the size of inter-fiber pores and therefore, the effective capillary radius. The authors stated that the gravity can be neglected if the pore dimensions are sufficiently small, as in the case of their experiments, except when the equilibrium weight of capillary liquid rise is approached. Fiber swelling is supposed to alter the size of pores between fibers, and the fiber volume fraction. Instead of effective capillary radius, the hydraulic radius (R_h) in Equation 4.11 is redefined in terms of fiber volume fraction [170].

$$R_h = \frac{A(1 - V_f)}{\lambda_{per}} \quad (4.18)$$

Where λ_{per} is the perimeter of fibers inside the mold. As stated earlier, the capillary rise can be monitored either using optical techniques like infrared or visual light transmission [64] or by measuring the mass uptake by the fiber bundle. The optical measurements provide information regarding the position of the flow front, thereby exact height, but in the case of natural fibers which are opaque, it is quite difficult to determine the flow front position. Also, the capillary rise in natural fibers is not just related to the amount of liquid between the fibers. The liquid inside fibers should also be taken into account. Therefore the mass uptake by natural fibers (m) during capillary rise can be expressed as:

$$m = m_{capillary} + m_{absorption} \quad (4.19)$$

where, $m_{capillary}$ is the mass of liquid which rises along the interfiber spaces and $m_{absorption}$ is the mass of liquid absorbed by the flax fibers. These two terms can be further expressed as:

$$m_{capillary} = A_{mold}[\rho_L(1 - V_f(t))h(t)] \quad (4.20a)$$

$$m_{absorption} = A_{mold}[\rho_f V_f(t) C_r(t) h(t)] \quad (4.20b)$$

where $C_R(t)$ is the liquid absorption ratio of fiber which is mass of liquid in fibers per unit mass and A_{mold} is the cross-sectional area of the mold. More details regarding these terms can be found in [1]. As liquid absorption by fibers causes the fibers to swell, the effects of fiber swell are also considered. The swelling of fibers was experimentally determined using an optical microscope. As it is widely known that the flax fibers do not possess a regular cross-section, the swelling ratio presented in this work is calculated using the apparent diameter of the fibers. Also, in reality, the swelling may also cause an increase in the length of the fibers, but it has been known that the increase in length is negligible. Therefore, the fiber volume fraction can be expressed as a function of fiber swell [43]. The effective fiber volume fraction can be expressed as:

$$V_f(t) = f_{sw}^2(t) \times V_{f,i} \quad (4.21)$$

where $V_{f,i}$ is the initial fiber volume fraction of the sample. By replacing $h(t)$ in Equation 4.19 with Washburn equation, the total mass gain can be expressed as,

$$m(t) = A_{mold}[\rho_L(1 - V_f(t)) + \rho_f V_f(t) C_r(t)] \sqrt{\frac{2K}{R_h} \frac{\sigma_L \cos \theta t}{\mu}} \quad (4.22)$$

Fiber swell causes a change in effective volume fraction of fibers and it can be presented as a function of fiber swell ratio. As $V_f(t)$ changes, the permeability also changes along with it and can be represented as :

$$K(t) = f(V_f(t)) \quad (4.23)$$

The only unknown parameter is $\frac{K}{R_h}$ in Equation 4.22. Both permeability and hydraulic radius are related to the fiber volume fraction which is also dependent on the geometrical organization of fibers in the mold. Since the diameter of flax fibers is not constant and varies from fiber to fiber, a log-normal distribution is implemented to determine the hydraulic diameter.

The i -th moment of a distribution of an entity is given by:

$$m_i = \int_0^\infty r^i n(r) dr = n_0 \exp\left(i\mu + \frac{i^2 \sigma^2}{2}\right) \quad (4.24)$$

The sum of cross-section area of fibers can be represented as :

$$\pi m_2 = \pi \int_0^\infty r^2 n(r) dr = \pi N_0 \exp(2\mu + 2\sigma^2) \quad (4.25)$$

and the perimeter of fibers as :

$$2\pi m_1 = 2\pi \int_0^\infty r n(r) dr = 2\pi N_0 \exp\left(\mu + \frac{\sigma^2}{2}\right) \quad (4.26)$$

And from the above Equations, hydraulic diameter can be expressed as :

$$R_h = \frac{\pi N_0 \exp(2\mu + 2\sigma^2) V_f}{2\pi N_0 \exp\left(\mu + \frac{\sigma^2}{2}\right)} \quad (4.27)$$

$$= \frac{1 - c_1 V_f}{c_2 V_f}$$

The empirical model to determine the ratio of K to R_h can be written as :

$$\frac{K(V_f)}{R_h(V_f)} = \frac{c_2 V_f^{bm+1}}{1 - c_1 V_f} \quad (4.28)$$

where c_1 , c_2 , bm are model constants. Inserting Equation 4.28 in Equation 4.22,

$$m(t) = A_{mold} [\rho_L (1 - f_{sw}^2(t) V_f(t)) + \rho_f f_{sw}^2(t) V_f(t) C_r(t)] \sqrt{2 \frac{c_2 V_f^{bm+1}}{1 - c_1 V_f} \frac{\sigma_L \cos \theta t}{\mu}} \quad (4.29)$$

4.3 Experimental Setup

4.3.1 In-house experimental setup

Initially, an in-house experimental setup consisting of a borosilicate glass tube of length 150mm with a diameter of 8 mm was used to measure the mass gain in the sample (Figure 4.8). The fibers were cut to the length of the tube and weighed. The volume fraction of test samples was controlled by weight and length of fibers. A mass balance with an accuracy of 0.0001g was utilized to record the change in the mass of the sample using a digital camera. Test liquid, water in the current scenario, was carefully added to a container onto which the sample was hung with the help of a metal frame. The liquid was added in small quantities with the help of a pipette until the level of liquid reached the edge of a glass tube containing the fibers. After complete saturation of fibers, the recording was stopped and was processed manually to obtain the m^2 vs. time graph. Due to high inaccuracies and intense manual labor, this setup was replaced by tensiometer with automatic acquisition (Figure 4.9).

4.3.2 Tensiometer

A tensiometer(K100 by Kruss GmbH) was used for capillary experiments with an accuracy of $100\mu\text{g}$. All the tests were carried out under the standardized conditions, at 20°C and 50% RH. The sample holder was a cylindrical borosilicate glass tube of length 100mm with a diameter of 8mm. The fiber samples were cut to the exact length of the tube and were inserted into the mold, making sure that there are no bends or twists of fibers (See

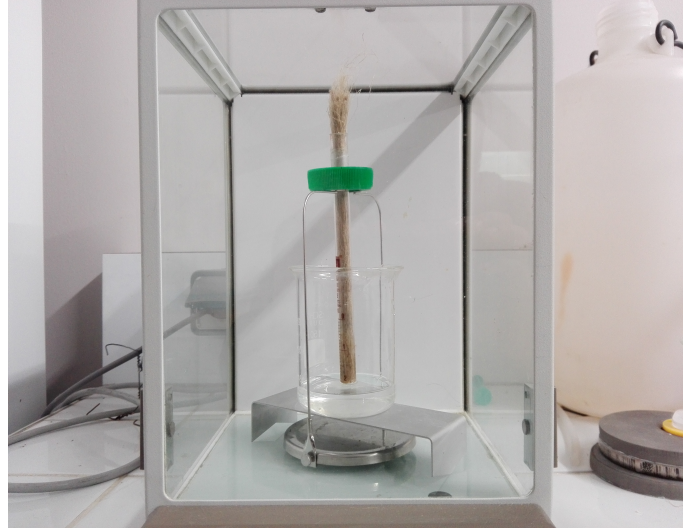


Figure 4.8: In-house experimental setup for capillary wicking

Figure 4.9). Two different fibers were tested, i.e., glass and flax. Glass fibers were used to study the case where fibers exhibit no absorption nor swelling.

Three different fiber volume fractions ($V_f = 30, 35, 40\%$) were tested during this study. For glass fibers, it was easy to achieve a fiber volume fraction of 55%, but for flax, 40% was the maximum as the tube was not able to accommodate more than 40% of fibers as they were in a swollen state at the end of experiment and it was not possible to replace the sample for next experiment. Also for glass fibers, due to their fineness, the tube was not able to hold the fibers in place when 30% of fibers was tested. Washburn's equation was adopted for this experimental procedure. It is obvious that this relation is well-verified if m^2vt curves recorded by the tensiometer during capillary wicking have a linear trend.

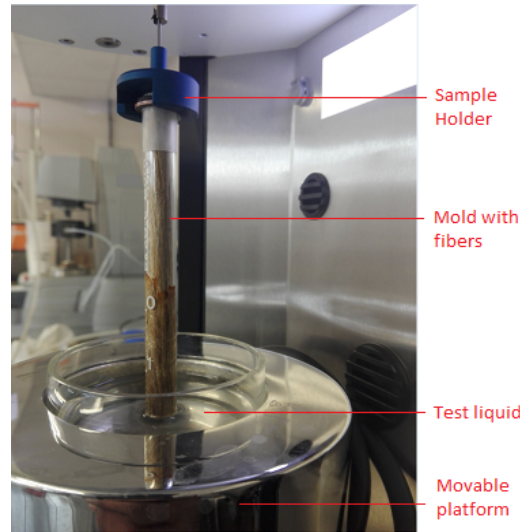


Figure 4.9: Sample setup for capillary wicking test

In this study, two types of fabrics were used to obtain the fiber samples: a unidirec-

Liquid	γ_L	μ	ρ	γ_L^p	γ_L^d
	mN/m	mPa.s	g/cm ³	mN/m	mn/m
n-Hexane	18.4	0.32	0.659	0	18.4
Water	72.8	1	0.998	51	21.8

Table 4.1: Properties of test liquids

tional glass fabric provided by Chomarat, France with an areal weight of 1300g/m² and a flax fabric Nattex 600 provided by Dehondt, France with an areal weight of 600g/m². The flax fibers were preconditioned in a conditioning room at RH 65% and 20°C for at least 24 hours before the tests. This conditioning of fibers will ensure the repeatability of tests as there will no change in the mass of fibers before and after the preparation of the sample. Glass fabric was mainly used as a model material to validate the technique. n-Hexane and distilled water were used as test liquids. The properties of fluids are provided in Table 4.1. Water is the most common test liquid for capillary wicking experiments [115], and it has a high polar component of surface energy. This high polar content will lead to the maximum interaction with flax fibers as they are also highly polar by nature. n-hexane, on the other hand, is mainly used due to its high dispersive nature which leads to almost complete wetting of the solid ($\cos\theta = 1$). All the experiments were conducted in a controlled environment of 20 °C \pm 0.5 at 65% RH. The tests are carried out by placing the fibers inside a 10cm long borosilicate tube, ensuring that there are no fiber kinks or misorientations. It should be noted that the efforts were made to ensure the uniformity and perfect alignment of fibers. Nevertheless, in the case of flax fibers, due to their bulkiness, at times, a few fibers were misaligned or kinked, which was deemed to be inevitable. It was foreseen that in the case of highly misoriented fibers or kinks, the sample was classified as 'not suitable' and was omitted from the calculation.

4.4 Experimental results

4.4.1 Validation of experimental set-up

Initially, a series of wicking experiments were conducted to verify the reproducibility of experiments using glass fibers and water. A constant fiber volume fraction of 40% was maintained for all experiments to avoid any discrepancies arising from a change in the fiber volume fraction. Also, two different cylindrical tubes were used during these tests. The interest was to select the appropriate tube for these wicking experiments considering the placement of fibers inside the tube and the effect of the tube's length. One sample holder was made of borosilicate with a length 50 mm provided by KRUSS GmbH, and

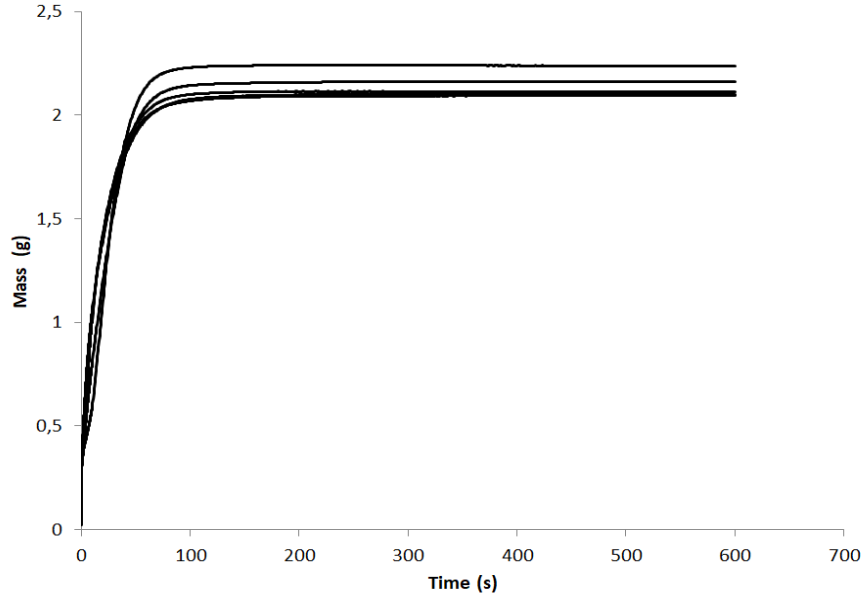


Figure 4.10: Repeatability of capillary experiments with 50mm capillary tube

another sample holder was an in-house holder made from a borosilicate glass pipette with the length of 100mm.

In Figures 4.10 and 4.11, we can observe the reproducibility of the experiment. A linear mass gain is observed, and a complete saturation plateau is achieved for an experimental run of 600 seconds. This linear part of the curve can be modeled with Washburn's equation (Equation 4.8). The difference in the mass gain in Figures 4.10 and 4.11 is due to the change in the size of samples. Even though the long term behavior is considerably same for both tubes, the 50mm tube shows high variability in the saturation limit. Also, it was found to be difficult to handle smaller length fibers as introducing them into the glass tube without deformation was highly difficult. Furthermore, even if the uniformity of fibers was achieved, the saturation limits are highly variable even in the case of constant fiber volume fraction whereas, in the case of 100mm tube, the saturation limits are almost the same showing little variation. Hence, all further experiments were carried out using the 100mm long glass tube.

4.4.2 Capillary rise results for glass and flax fibers

The experimental results of capillary rise tests with water for glass and flax fibers with a constant fiber volume fraction of 40% is shown in Figure 4.12. It can be noticed that the repeatability of tests for flax and glass fibers is not the same. Glass fibers exhibited excellent repeatability, whereas, for flax fibers, the variability is pronounced. This variability can be induced by highly variable tortuosity caused by the irregular fiber diameters and fiber lengths[171]. It can also be caused by the irregular fiber swell ratio,

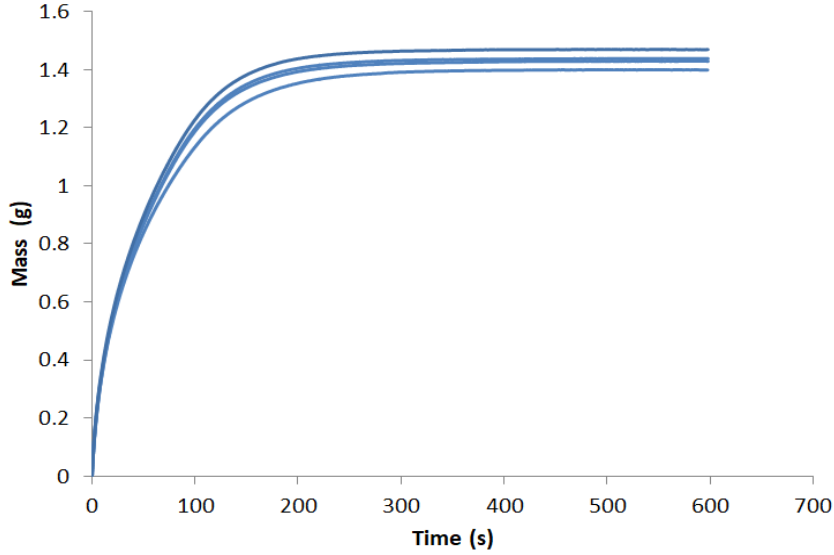


Figure 4.11: Repeatability of capillary rise experiments with 100mm capillary tube

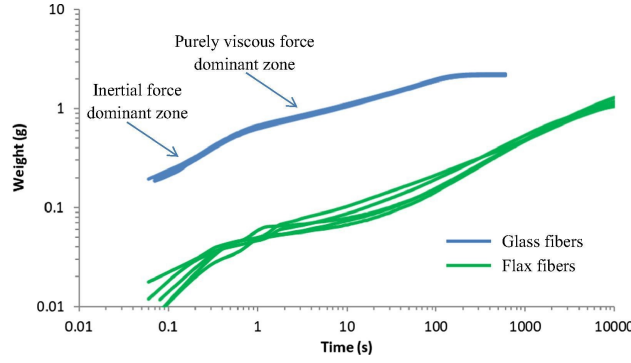


Figure 4.12: Capillary rise tests for glass and flax fibers at $V_f = 40\%$ exhibiting different zones

as the fiber swell ratio is highly dependent on the chemical composition of the fibers [44]. These results clearly show the difference between a non-swelling porous medium and a swelling porous medium (Figure 4.12).

In the case of glass fibers, irrespective of the test liquid used, the complete saturation of the test specimen was observed. The time taken to reach complete saturation was around 200 seconds. On the contrary, an equilibrium plateau was not observed for flax fiber specimens even after 10000 seconds (except for n-hexane) (Figures 4.13 and 4.14). This is caused by the particular properties of natural fibers, i.e., liquid absorption and fiber swelling which do not occur in the case of glass fibers. As stated in the previous section, the mass gain by glass fiber specimens is only due to capillarity. Usually, n-hexane is expected to completely wet the fibers because of its dispersive nature regardless of the induced fiber swell ratio and liquid absorption rate. In Figure 4.13, it is evident that

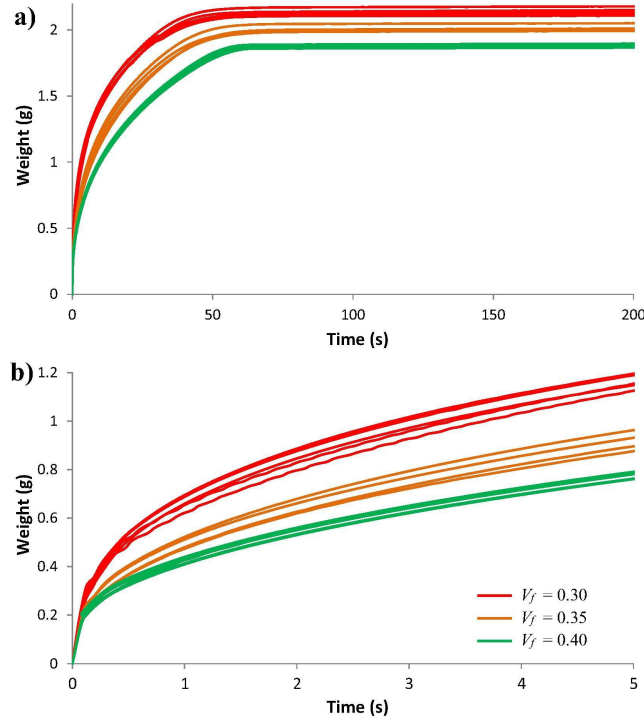


Figure 4.13: Capillary rise in flax fibers with n-hexane: complete duration (top) and initial stage (below)

when n-hexane is used as the test liquid, a clear saturation plateau can be observed after 60-70 seconds of wicking but is not the case for water.

In the case of water, due to the high polarity of fibers and liquid, the fibers swell faster and occupy the space around them, thereby locally increasing the apparent fiber volume fraction of specimen. Consequently, the capillary pressure inducing the liquid rise was increased. Thus, the equilibrium capillary rise height where the capillary pressure was equal to the gravitational force was increased. Therefore, it took longer to reach the equilibrium height in the case of the water. In Figure 4.14 and Table 4.3, it can be noticed that at low fiber volume fractions, the variability of mass gain is very high compared to those of high fiber volume fraction samples. This high variability can be explained by different swell ratios of individual flax fibers, and these values can be considered to be acceptable given the natural variation in morphological properties of fibers themselves. Even for different fiber volume fractions, the rate of mass gain for almost every sample at a particular fiber volume fraction is the same. If the distance between each filament is decreased and the fibers are more densely packed, the collective response of the fibers induces a repeatable output. The variations among each test and for each volume fraction for both test liquids can be found in Tables 4.2 and 4.3.

However, flax fibers, on the other hand, do not reach a saturation plateau even after 14000 seconds. In Figure 4.15, the initiation of saturation plateau cannot be observed

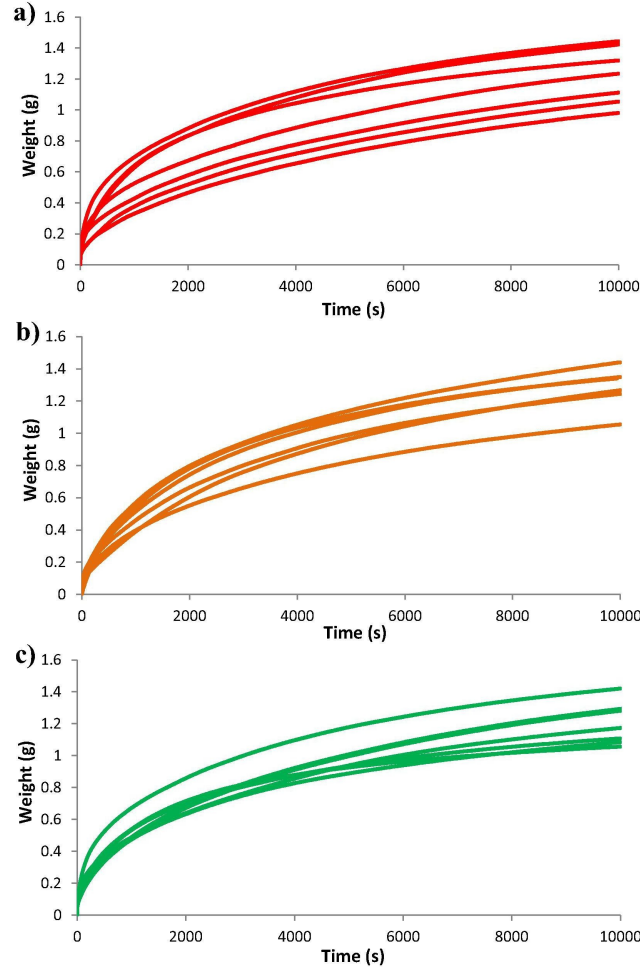


Figure 4.14: Capillary rise in flax fibers with water: 30% V_f (top), 35% V_f (middle) & 40% V_f (bottom)

	$V_f=30\%$		$V_f=35\%$		$V_f=40\%$	
	m^2/t (g^2/t)	R^2	m^2/t (g^2/s)	R^2	m^2/t (g^2/s)	R^2
Test 1	1.20E-1	0.991	9.47E-1	0.996	7.31E-2	0.997
Test 2	1.17E-1	0.994	8.98E-1	0.998	7.06E-2	0.998
Test 3	1.04E-1	0.994	9.14E-1	0.997	7.19E-2	0.998
Test 4	1.11E-1	0.997	9.81E-1	0.995	7.21E-2	0.998
Test 5	1.20E-1	0.993	8.98E-1	0.998	7.15E-2	0.998
Test 6	1.14E-1	0.994	9.81E-1	0.995	7.08E-2	0.997
Average	1.14E-1		9.37E-2		7.17E-2	
SD	6E-3		3.88E-3		9.18E-4	
Variation	5.2%		4.1%		1.3%	

Table 4.2: Capillary rise results for flax fibers with n-hexane at different fiber volume fractions

	$V_f=30\%$		$V_f=35\%$		$V_f=40\%$	
	m^2/t (g^2/t)	R^2	m^2/t (g^2/s)	R^2	m^2/t (g^2/s)	R^2
Test 1	1.09E-3	0.958	7.14E-4	0.999	4.17E-4	0.997
Test 2	9.68E-4	0.964	5.04E-4	0.998	4.82E-4	0.997
Test 3	7.87E-4	0.989	7.43E-4	0.999	4.54E-4	0.998
Test 4	8.05E-4	0.997	4.42E-4	0.999	3.72E-4	0.987
Test 5	7.38E-4	0.977	5.29E-4	0.996	3.54E-4	0.998
Test 6	6.35E-4	0.982	7.15E-4	0.998	3.72E-4	0.998
Average	8.37E-4		9.37E-2		7.17E-2	
SD	1.6E-4		3.88E-3		9.18E-4	
Variation	19.6%		21.5%		12.6%	

Table 4.3: Capillary rise results for flax fibers with water at different fiber volume fractions

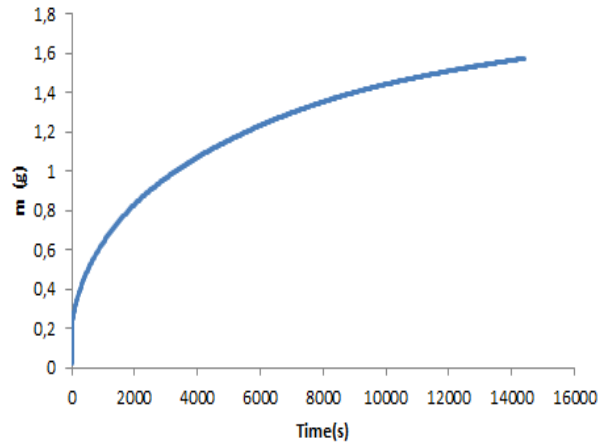


Figure 4.15: Capillary rise of flax fibers with water as test liquid (Experiment time: 14000s)

even after 14300 seconds. It can be observed that the mass of the sample is continually increasing, but the rate of mass uptake has decreased. This decrease is caused by swelling of fibers which led a decrease in hydraulic radius because the permeability of fibers is a function of swelling and volume fraction.

4.4.3 Identification of model constants

In order to use the proposed model in Section 4.2, it is necessary to identify the model constants. The first step was to determine the ratio of the permeability to the hydraulic radius ratio. n-hexane was used as a test liquid because the contact angle θ is 0. Therefore the Equation 4.22 becomes,

$$m(t) = A_{mold}[\rho_L(1 - V(t)) + \rho_f V_f(t) C_r(t)] \sqrt{\frac{2K}{R_h} \frac{\sigma_L t}{\mu}} \quad (4.30)$$

By varying fiber volume fraction, K/R_h for each case can be obtained, and the empirical model, Equation 4.28 can be fitted to the experimental values. The results are presented in the Figure 4.16 and in Table 4.4. Even in this case, the experimental results are highly scattered at low volume fractions, and the scattering gradually decreases as V_f increases to 40%. The curve fitting in Figure 4.16 shows a very good agreement with R^2 of 0.96. The value of maximum absorption ratio ($C_R = 0.39$) and the evolution of liquid absorption were adopted from [1].

Table 4.4: Coefficients of K/R_h empirical model 4.28

Coefficient	average	max and min values
C_2	3.563e-007	(-2.19e-006, 2.903e-006)
$bm + 1$	-3.185	(-6.154, -0.215)
C_1	-0.02274	(-12.01, 11.96)

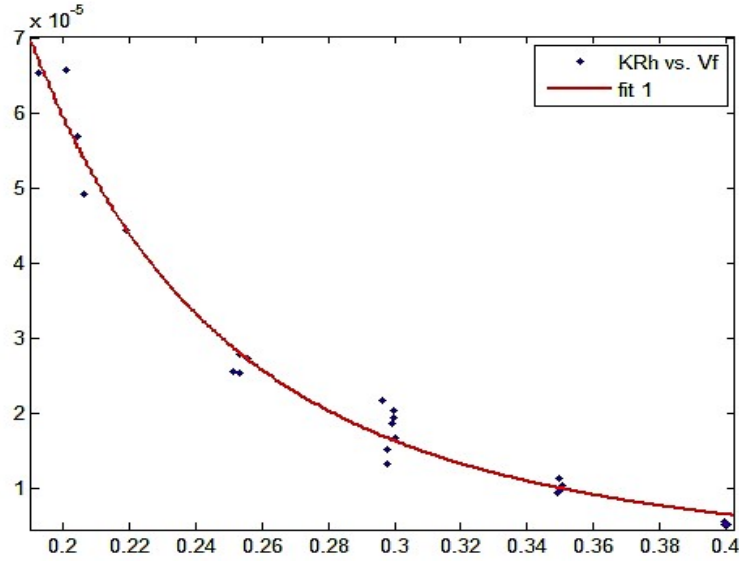


Figure 4.16: K/R_h determination using n-hexane and flax fibers

With these two (k/R_h and absorption ratio) parameters known, the contact angle between test liquid and fibers can be calculated using Equation 4.29. The model was fitted in the initial viscous stage and the dynamic contact angle (or advancing contact angle) was estimated (see Table 4.5).

Table 4.5: Estimated contact angle based on Equation 4.29 for different V_f

Fiber volume fraction	Contact angle
30%	62.4 ± 5.6
40 %	68.0 ± 4.8
45%	70.5 ± 4.2

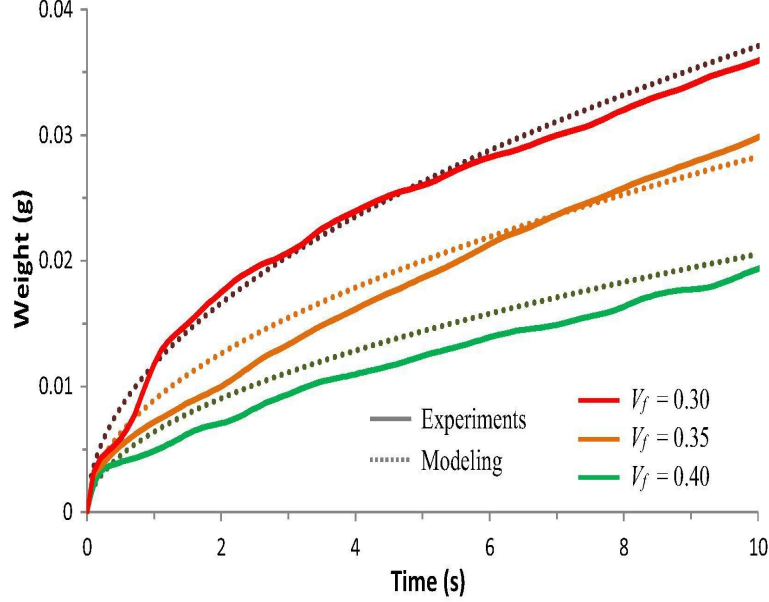


Figure 4.17: Comparison between proposed model and experimental results in the initial viscous stage

4.5 Validation of proposed model

The model prediction and experimental results in the initial viscous stage are compared in Figure 4.17. The evolution of K/R_h ratio with time is presented in Figure 4.18. Even though the initial K/R_h is different for each V_f , as the flow front advances, the individual values tend to converge. This indicates that in the case of long term wicking, the influence of fiber swell on mass gain is more significant.

The results of model prediction by the modified Washburn equation 4.29 using the data of fiber swelling and liquid absorption in the references of Nguyen et al.[43] were compared with the experimental results for the fiber volume fraction of 30%. We can see that the modeling results by the modified Washburn equation highly underestimated the mass gain compared with the experimental results (Case E in Figure 4.19) at the later stage of capillary rise whereas there was a good agreement in the early stage. It has been already reported by experimental work in the literature that the increase of fiber swelling decreases the capillary wicking velocity [102]. As the water is absorbed into the flax fibers and the fiber diameter is increased, the ratio of permeability to hydraulic radius

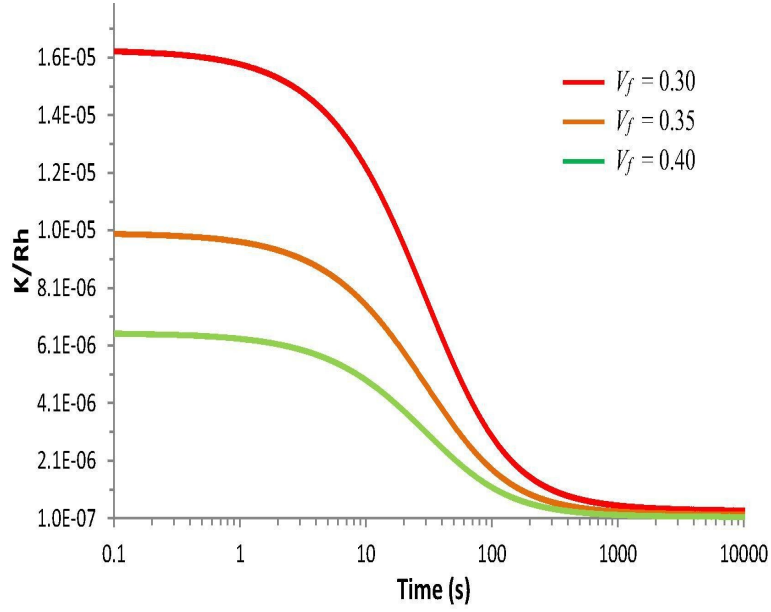


Figure 4.18: Evolution of K/R_h ratio with time for different fiber volume fractions

Case	$f_{sw,max}$	$C_{R,max}$
A	1.00	0
B	1.05	0.10
C	1.10	0.20
D	1.24	0.3
E	1.31	0.39

Table 4.6: Values of fiber swell ratio and maximum liquid absorption ratio used for parametric study

is decreased, and the capillary rise velocity is decreased. Therefore, we can deduce that the fiber swelling ratio of the flax fibers used in the capillary test was smaller than that reported in [1]. It should be kept in mind that the experimental observation of flax fiber swelling in the literature [43] was performed with a single individual fiber which could swell without any external constraint. Conversely, the flax fibers used in the current capillary tests were confined inside the cylindrical tube and were contact with each other. Hence, there was an interaction among the fibers, which might lead to a mechanical constraint hindering fiber swelling.

A parametric study was carried out to investigate the influence of fiber swell and liquid absorption parameters on the capillary rise. The mass gain was calculated using Equation 4.29. The different swell ratios and absorption coefficients used to conduct such parametric study are reported in Table 4.6. The values selected in this work were based on the assumption that the swelling is linearly proportional to liquid absorption. Two extreme

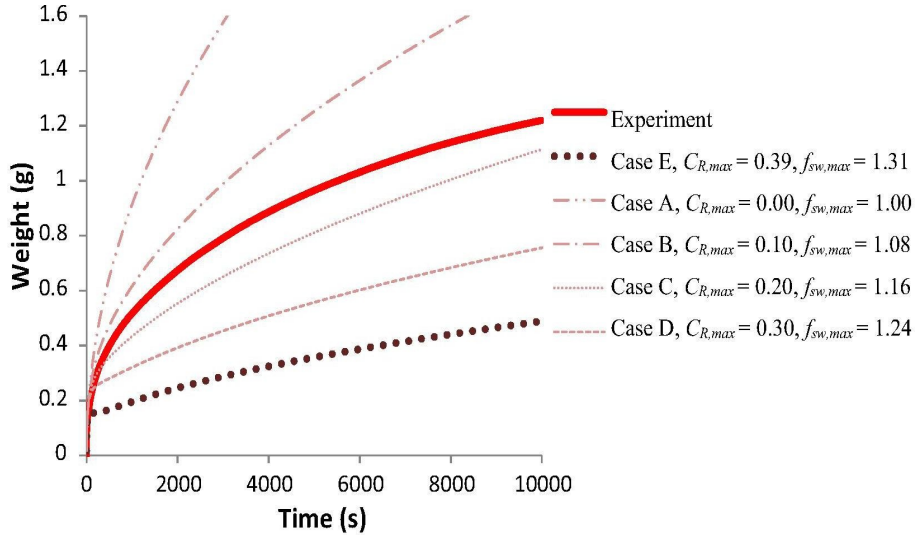


Figure 4.19: Parametric analysis of capillary wicking model with different fiber swell and liquid absorption ratios

cases, Case A and E, are also included in this study. Case A refers to glass fibers, where the fibers neither swell nor absorb liquid and Case E refers to free flax fibers in a free space where the fibers swell to their maximum and absorb liquid the most. The data concerning the case E were obtained from the literature [1, 43]. The modeling results can be seen in Figure 4.19. Regarding case A, the rate of mass gain was smaller than the model estimate. For case E, when the modeling results are compared with the experimental results, the mass gain rate is lower than the experimental data while the mass gain tends to reach a plateau value far less than that of values observed experimentally. This indicates that the fiber swell ratio and maximum absorption ratio values used not coherent with real values. These two cases act as the lower and upper bounds for these fibers. Whereas the intermediate case, Case C, exhibits a closer agreement to the experimental results. The fiber swelling ratio and liquid absorption ratio of the flax fibers confined in the glass tube were estimated to model the long-term behavior of capillary rise. Firstly, the contact angle, as well as the model coefficients for the ratio of permeability to hydraulic radius, was obtained by the modified Washburn equation (Equation 4.29) for the initial viscous stage of the capillary rise where the effects of fiber swelling and liquid absorption were insignificant. Then, the fiber swelling ratio and liquid absorption ratio were estimated by fitting the experimental data of mass gain for the later stage of capillary rise. The results for the maximum fiber swelling ratios and the corresponding effective fiber volume fractions are shown in Table 4.7. It can be clearly observed that the effective fiber volume fraction reached the same value irrespective of the initial fiber volume fraction. This indicates that the fibers cannot swell to their maximum extent.

Table 4.7: Maximum fiber swell ratio and corresponding fiber volume fraction obtained from experimental data

V_f (t=0s)	$V_{f,eff}$ (t=10000s)	$f_{sw,max}$ (t=10000s)
0.30	0.43	1.19
0.35	0.43	1.11
0.40	0.45	1.06

4.6 Conclusion

A capillary rise model was developed considering the fiber swell and liquid absorption in flax fibers. It was experimentally validated by conducting wicking experiments with both glass and flax fibers. This proposed model takes into account not only the mass of the liquid between the fibers by capillary wicking but also the mass of liquid absorbed inside the fibers which have not been addressed in the literature about the capillary wicking in swelling and absorbing media [44, 50, 115, 169, 172]. The change of flow resistance during the capillary rise due to the fiber swelling can be taken into account by modeling the ratio of permeability to the hydraulic radius (K/R_h) in terms of effective fiber volume fraction (Figure 4.16). Due to the non-uniform distribution of flax fibers, the statistical approach was used to calculate the ratio of permeability to the hydraulic radius. The experimental results of capillary rise tests showed evident differences between these two fiber types and demonstrated the validity of the proposed model. The data for fiber swelling and liquid absorption obtained from a single individual fiber was not adequate to model the long-term behavior of capillary rise of liquid in flax fiber samples inside the glass tube. The fibers confined in the glass tube were submitted to a mutual interaction in a closed space. Hence, the fiber swelling and liquid absorption of the flax fiber samples in the capillary rise were smaller than those of a single individual fiber in free space. For example, when immersed in water, the maximum swell ratio of flax fibers contained in a glass tube with the fiber volume fraction of 0.40 was 1.06 whereas the maximum swell ratio of single individual fibers in free space was 1.31. This implies that the fiber swell should be considered with respect to the initial porosity of the sample. Nevertheless, two issues should be addressed in further research. Firstly, the assumption of constant contact angle is not exactly true in reality and it is dependent on fiber swell as the advancing velocity in porous media is a function of fiber swell. The fiber swell also affects the K/R_h ratio, which can also affect the contact angle. Therefore, the contact angle estimated in this work is an average contact angle.

Chapter 5

Influence of process parameters on composite quality

Composite materials have intrinsic heterogeneity which is usually caused by their complex microstructure leading to a different range of physical and mechanical properties. This variation in properties is dependent on the fiber preform architecture and processing conditions. Because the uncertainties arising from the material is unavoidable, it is necessary to understand how the processing conditions will affect the final composite [116]. In textile fiber composites, one of the essential steps in processing is the impregnation of the fiber reinforcement. In the case of Liquid Composite Moulding, the most influencing parameter for impregnation is the permeability of preform (K). For designing a tool for part production, it requires the knowledge concerning the placement of injection points and air vents, and geometric shape parameters. This is usually tackled by creating virtual parts using CAD and CAE software to find the optimum conditions to fill the part without any dry spots. A handful of softwares already exist in the market, which can perform such simulations. Nevertheless, these programs need several inputs related to both preform (tow permeability, global permeability, fiber volume fraction, etc.) and impregnating fluid (viscosity, surface tension, etc.). Nevertheless, determining the preform properties is challenging. As explained in Chapter 2, the fiber preforms exhibit often dual-scale porosity, one within the tows and the other in channels between the tows. This difference in the porosities causes a delay in impregnation of tows leading to a new term in the mass conservation equation (Equation 2.9) called 'Sink' term. The influence of this term was highlighted in many studies [38, 45, 173, 174], and this term is highly dependent on the tow permeability. Moreover, this parameter also affects the void formation during impregnation. Generally, the tow permeability is estimated by using one of any existing analytical models in the literature because its experimental measurements are difficult. Recently, it has been pointed out that not all the models are capable of predicting the

actual value of tow permeability [175]. Therefore this chapter mostly concentrates on two issues. The first is to identify which model is suitable for flax fiber tows and the second one is to understand the influence of fiber swell and liquid absorption on void formation in flax fiber preforms.

5.1 Tow Permeability

Many works suggested mathematical models for predicting the permeability of a saturated porous media at different scales, both macroscopic and microscopic level. At the microscale, for modeling the steady-state flow through fiber arrangements, periodic fiber arrangement such as hexagonal or square packing is assumed which is far from the reality. In these models, the fiber waviness, fiber surface roughness, and the variations of diameter are not taken into account. Also, the fibers are assumed to be rigid and non-deformable. Gebart [176] proposed an analytical model for unidirectional fiber bed with two different fiber arrangements based on Navier-Stokes equations for creeping flow. He retained the Kozeny-Carman model for permeability in the longitudinal direction while proposing the Kozeny constant according to the arrangement of the fibers. Whereas, for the transverse permeability of the fiber bed, it was based on the periodicity of an elementary cell consisting of a cylinder stack. The permeability of this elementary cell was calculated and then homogenized to the macroscopic application. For the transverse flow across the fibers, Gebart defined expression for permeability as:

$$K_{\perp G} = C_1 \left(\sqrt{\frac{V_{fmax}}{V_f}} - 1 \right)^{\frac{5}{2}} r_f^2 \quad (5.1)$$

Where C_1 is the model constant based on the fiber arrangement. It can be noted that in Equation 5.1, the permeability is only dependent on the geometric parameters and the fiber packing arrangement. Also, the model limits to a maximum fiber volume fraction (V_{fmax}) of 0.785 and 0.907 for square and hexagonal packing arrangements, respectively. Because of simplicity of this model, the agreement with experimental data was not always found to be a good fit yet this model is still used by many authors [68, 69, 141, 177] as it is easy to implement.

Berdichevsky and Cai [178] developed a model to predict the longitudinal and transverse permeabilities of unidirectional fiber bed with square and hexagonal packing. They implemented a self-consistent scheme to develop an analytical expression for the permeability of fibrous media with regular packing arrangement. The model was in good agreement with the finite element simulations, but again, the assumptions like constant

fiber diameter and regular packing are the drawbacks of the model.

$$K_{\perp BC} = \frac{d_f^2}{32(1-\epsilon)} \left[\ln\left(\frac{1}{(1-\epsilon)^2} - \epsilon(2+\epsilon)\right) \right] \quad (5.2)$$

where d_f is the diameter of the fiber and ϵ is the porosity of the preform.

Kuwabara [179] investigated the flow across parallel cylinders which were randomly distributed in a square cell by considering that the local coordinate system is moving along the direction of principal velocity. Using a Stokes approximation, he proposed a model to predict the transverse permeability ($K_{\perp kuw}$) of a unit cell.

$$K_{\perp kuw} = \frac{d_f^2}{32(1-\epsilon)} \left[\ln\left(\frac{1}{(1-\epsilon)}\right) - 1.5 + 2(1-\epsilon) - \frac{(1-\epsilon)^2}{2} \right] \quad (5.3)$$

Tamayol and Bahrami [180] employed a scale analysis technique for determining the transverse permeability of a unit cell with various arrangements including square, staggered, and hexagonal. For a square arrangement, the permeability is represented as:

$$K_{\perp TBsq} = \frac{0.16d_f^2}{\sqrt{\epsilon}} \left[\frac{\pi}{4(1-\epsilon)} - 3\sqrt{\frac{\pi}{4(1-\epsilon)}} + 3 - \sqrt{\frac{4(1-\epsilon)}{\pi}} \right] \quad (5.4)$$

For a hexagonal arrangement, the permeability is expressed by:

$$K_{\perp TBhex} = \frac{0.16d_f^2}{\sqrt{\epsilon}} \left[\frac{\pi}{3\sqrt{3}} - 3\sqrt{\frac{\pi}{3\sqrt{3}(1-\epsilon)}} + 3 - \sqrt{\frac{3\sqrt{3}(1-\epsilon)}{\pi}} \right] \quad (5.5)$$

Similar to Kuwabara's model (Equation 5.3), Westhuizen and Du plessis [181] also developed a model by integrating the Phase averaged Navier Stokes equation. An assumption was made that at high fiber volume fractions, the channels can be regarded as square ducts.

$$K_{\perp WD} = \frac{\pi(1-\alpha)(1-\sqrt{\alpha})^2}{96\alpha^{1.5}} \quad (5.6)$$

where α is expressed as:

$$\alpha = 2.2(1-\epsilon)^2 - 1.22(1-\epsilon) + 0.56 \quad (5.7)$$

Unlike the above-mentioned models, there are some models in literature which are defined at a preform level. The Kozeny-Carman model [41] was developed originally for granular porous media. This model is based on parallel channel geometry and makes it possible to predict the permeability in the direction of the fibers. However, by generalizing the Kozeny constant in 3D, the following permeability tensor can be obtained:

$$K_{KC} = \frac{1}{4C_{cozi}} \frac{(1-V_f)^3}{V_f^2} r_f^2 \quad (5.8)$$

The constant C_{coz_i} can be determined experimentally and thus making the model into a semi empirical model . The Kozeny-Carman model was developed for an isotropic granular medium, and was generalized for fibrous media.

Zarandi et al [175] compared their experimental results of permeability measurement with a model suggested for sedimentary media by Knacksted and Duplessis [182]. Although the model (Equation 5.9) is suggested for low porosities, the predicted values were far from the experimental results. Nevertheless, this model considers both porosity and average grain size, thus, it might be interesting to test it for flax fibers.

$$K_{KD} = \frac{\epsilon \left[1 - (1 - \epsilon)^{1/3} \right] \left[1 - (1 - \epsilon)^{2/3} \right]}{\left[64(1 - \epsilon)^{4/3} \right]} \quad (5.9)$$

All the proposed models, the discussed above, are based only on the regular microstructures and ignore the intrinsic variability of the fibers as well as fiber waviness. If these factors are considered, the estimated permeability value can be closer to reality and no more a mere approximation. In order to do so, a practical approach would be to use the numerical tools for flow simulations to provide a permeability value from the microstructure of preform.

5.1.1 Methodology

Flow simulations in LCM are carried out based on the assumption that the resin is an incompressible fluid flowing through a rigid homogeneous porous medium and is modeled using Darcy's law (Equation 5.10) coupled with the mass conservation equation (Equation 5.11).

$$\bar{u} = -\frac{\bar{K}}{\mu} \nabla P \quad (5.10)$$

$$\nabla \cdot \bar{u} = 0 \quad (5.11)$$

where \bar{u} is Darcy velocity, μ is the viscosity, ∇P is the pressure gradient, and \bar{K} is the permeability tensor of the fibrous medium. It is known that the permeability depends only on the geometric parameters and it can be expressed as:

$$K = f(r_f, V_f) \quad (5.12)$$

Where r_f is the radius of the fiber, V_f is the fiber volume fraction of Representative Volume Element (RVE). During the impregnation of resin into the fibrous bed, the Reynolds number is usually less than one satisfying the condition of laminar flow. Therefore, the classical Stokes equation can be used to estimate the averaged velocity, and is expressed as:

$$\nabla \left[-p\mathbf{I} + \mu(\nabla \mathbf{u} + (\nabla \mathbf{u})^T) \right] = \mathbf{0} \quad (5.13)$$

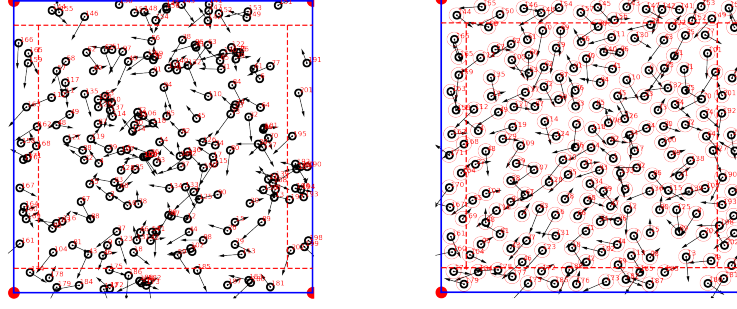


Figure 5.1: Evolution of RVE in case of 40% fiber volume fraction

5.1.2 RVE generation

In this work, RVEs are generated using the algorithm developed by Liu et al. [183]. The algorithm is based on Molecular Dynamics model to generate disks inside a given domain. The interest in using this algorithm is mainly related to its uniqueness like the placement of fibers with random size, packing randomly inside a predefined irregular region, which can be approximately outlined by a polygon and user-defined packing heterogeneity. The complete details regarding this algorithm can be found in [183] [Figure 5.1]. The only issue with this algorithm is that the maximum packing fraction is limited to 0.72. However, in comparison with other methods like Montecarlo or RSA adopted by previous studies, this algorithm gives better control over fiber diameter distribution. In this current work the equation[5.13] is implemented in COMSOL Multiphysics 5.3 [184]. The permeability calculations were done by linking the CFD solver to Matlab 2018R. The mean values and the distributions presented in this work correspond to 100 simulations per each fiber volume fraction.

In terms of analysis, two parameters were defined to address the fiber distribution in a given RVE. One is the local packing factor, and other is the inter-fiber distance δ . Although the minimum inter-fiber distance is already predefined in the generation algorithm to 0.03 times of radius of a circle, due to the irregularity of the fiber diameters, this factor varies inordinately. The evaluation of δ is carried out by adopting the nearest neighbor algorithm implemented using Matlab.

5.1.3 Validation of RVE size

It is widely known that the reliability of numerical simulation results of RVE are highly dependent on computational domain size. Hence, an investigation on RVE size is carried out to select the size of a square domain suitable for this work. A parameter ζ defined as a ratio of the length of the square domain to the average fiber radius ($7.5\mu m$), is

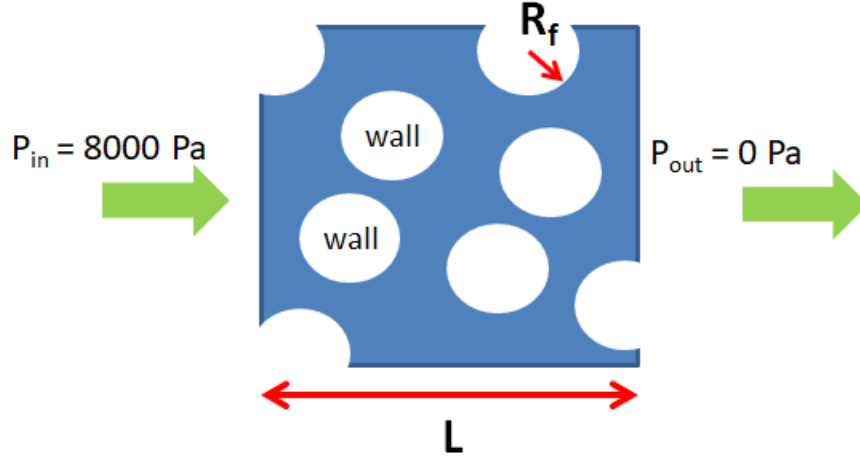


Figure 5.2: Illustration of a square domain used for numerical simulations

used to represent the domain size. Four different values of ζ (20, 30, 40, 50) are used to identify the minimum size required to estimate the permeability values without any domain induced errors. At least 150 simulations are conducted to obtain the mean value of K and the mean and standard deviation of K for every ζ . It can be seen that in Figure 5.3, the scatter in K values is significant in the case of domain size 20 and 30. With the increase in the domain size, the permeability value tends to converge. As the ζ further increases to 40 and 50, it can be observed in Figure 5.3 b, that the mean value reaches an almost constant value. It can be noted that the 75th percentile and 25th percentile range for $\zeta = 40$ and 50 are very small compared to that of that for $\zeta = 20$ & 30. As the minimum and maximum values are the only differentiating parameters between $\zeta = 40$ and 50, it is observed that there is no significant difference between the mean values of K . Therefore, it can be concluded that the domains with $\zeta \geq 40$ are suitable for these simulations.

Moreover, during the generation of these microstructures, the computational cost of the RVE generation is estimated. It is observed that the time to generate a single microstructure at $\zeta = 50$ is about 1.5 times longer than the microstructure $\zeta = 40$ with a fiber volume fraction of 60%. Given that at least 150 simulations are needed to obtain an average value with a small deviation, $\zeta = 50$ is computationally very costly. Also, with respect to solving this domain of interest in FEM solver, the computation time needed for one simulation with $\zeta = 50$ is twice that of the $\zeta = 40$ and the computation cost increased with increase in ζ . Hence, in order to save the computation cost, both in terms of generation, meshing and flow simulation, the domain that is 40 times bigger than the mean fiber radius is selected for further analysis. In case of constant fiber radius, the same domain size ($\zeta = 40$) is considered, which is in accordance with previous studies [185].

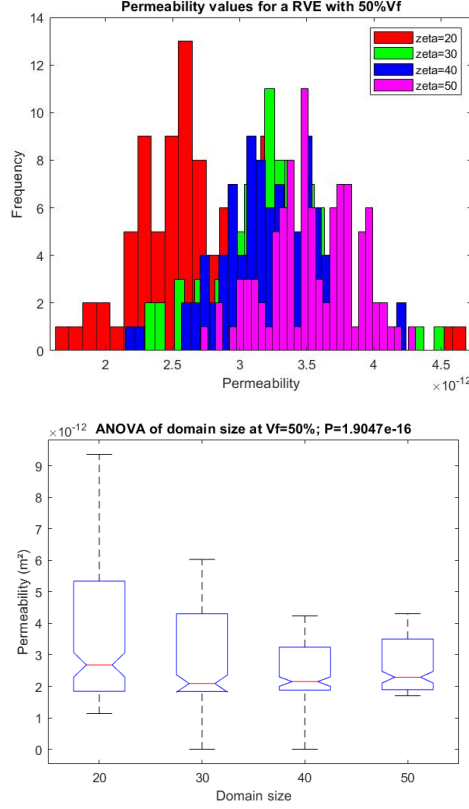


Figure 5.3: Comparison of different sizes of RVE at $V_f=40\%$ (a) Histogram of Permeability for four different ζ values and (b) ANOVA of the K values.

Once the size of RVE is determined, a mesh sensitivity study is carried out to understand the influence of element size and the mesh type that needs to be implemented in this study. COMSOL provides various mesh densities and also depending on the computational domain, it also suggests a mesh that would be apt for the simulation to converge faster. After several iterations, a minimum mesh size of $0.1\mu m$ and a maximum of $3\mu m$ is adopted. This mesh is adaptive to structure, i.e., the mesh density is higher around the fibers and comparatively lower far from the fiber edges. This approach decreases the number of elements therefore, the computational cost of the numerical model is less. This also solves the problem in the case of fibers which are positioned close together, especially in the case of high fiber volume fractions, as suggested by [186].

5.1.4 Inter fiber distances

The algorithm adopted for this study imposes a minimum fiber distance to facilitate the meshing of the computational domain [125]. Although this may not be true in reality because fibers touch each other at higher fiber volume fractions, the actual representation of microstructure not feasible for flow simulations because of meshing issues. So, in order to avoid such difficulties, a minimum fiber distance of 0.03 times of the average

fiber radius ($\approx 0.21\mu m$) is enforced, which is a relatively small gap compared to that of fiber radii which is around 5% [186–188]. Inter fiber distance is calculated for each RVE which is computationally analyzed. The inter-fiber distances were calculated for the first, second, third, and fourth closed neighbors. These distributions are right-tailed, but in the case of second neighbor distances, the distribution is observed to be heavily right-tailed, indicating that the distances are far from the observing fiber and randomness of distribution. A log-normal PDF can approximate these distributions. Also, in Figures 5.4 and 5.5, it can be noticed that there is a lower truncation limit as two fibers are not inter-penetrable. In reality, the distance between two filaments can be a value near to zero, but in the current scenario, this is not possible due to meshing issues which call for minimum distance. In Figures 5.4 and 5.5, we can notice the difference in the fiber volume fraction and the inter-fiber distances. In the case of RVE with constant fiber diameter (Cd-RVE), the first neighbor distance is highly dependent on the fiber volume fraction of RVE. It is known that as fiber volume fraction increases, the distance between two fibers decreases, and the fibers tend to be closely packed, which can be seen in Figure 5.4. In the case of fiber volume fraction above 50%, the majority of first neighbors can be found within a distance less than $4\mu m$, and for RVEs with $V_f = 60\%$, the first neighbors are within $1.5\mu m$ from each other. In reality, this value can be much lower; nevertheless, these values are in near agreement with the actual micro structures observed by Gommer et al.[76]. In the case of RVEs with variable fiber diameters (Vd-RVE), the distribution of inter-fiber distances is similar to that of Cd-RVEs. When a comparison is drawn between the second, third neighbor distances of both fiber distributions (Figure 5.4 and 5.5), there are higher number of fibers which are within the distance range of $0 - 3\mu m$ in Vd-RVEs. This indicates that the probability of finding a fiber within a fixed vicinity is higher in Vd-RVEs. Interestingly, when the fourth neighbor distances are compared, both sets of RVEs exhibit near similarities. In reality, this is true for composites with highly individualized fibers and can be true for technical bundles, but the distance range will be higher.

5.1.5 Numerical results and experimental validation

In Figure 5.6, the numerical results are plotted against the fiber volume fraction obtained from both RVEs. Clearly, at lower fiber volume fraction, there is no difference between both the cases of fiber diameter distribution, whereas, when the fiber volume fraction increases to 50%, the curves start to diverge. The difference in the permeability values between both cases is about 8% for fiber volume fractions between 30-45%. Above $V_f = 50\%$, the difference in permeability values between two RVE arrangements increased to 23%. This decrease in the permeability difference in the case of *Vd-RVE* can be linked to the high variation in fiber radius (see Figure 5.7), where the smaller fibers are usually

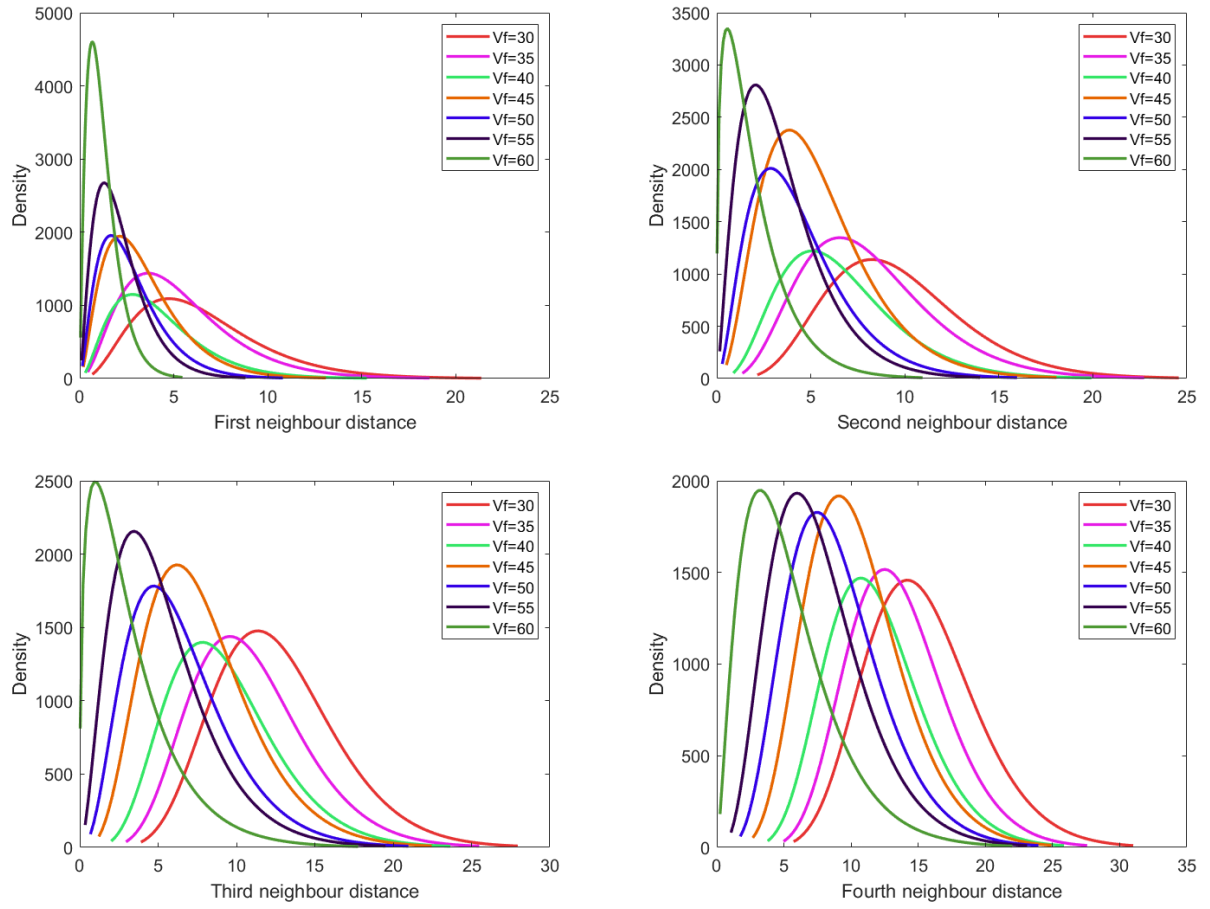


Figure 5.4: Inter fiber distances (μm) in RVEs with constant fiber diameter

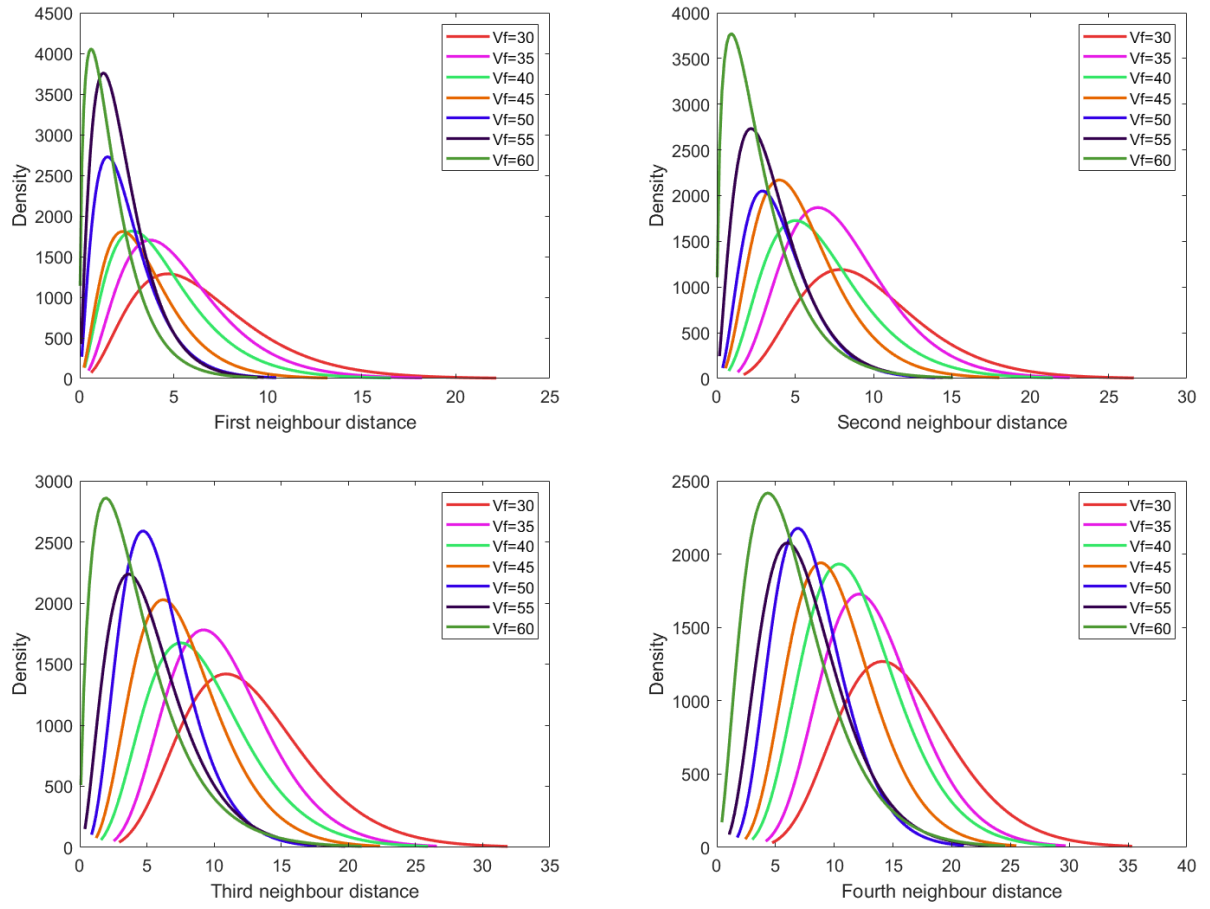


Figure 5.5: Inter fiber distances(μm) in RVEs with irregular fiber diameters

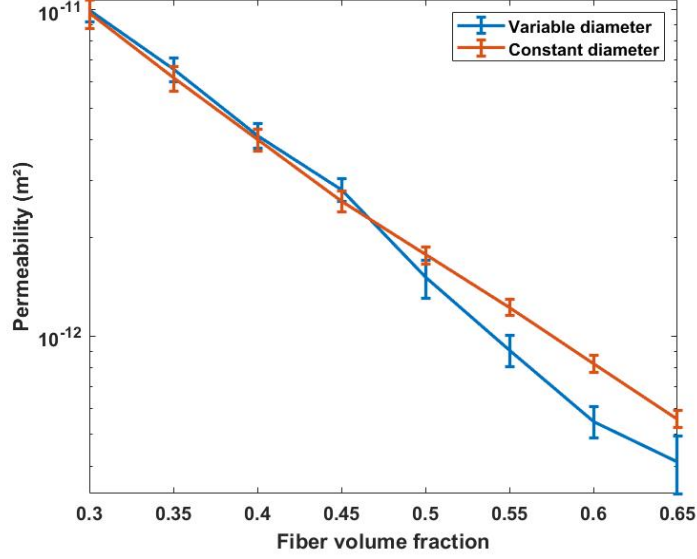


Figure 5.6: Permeability versus Fiber volume fraction: numerical results

arranged between the two bigger fibers, thus creating a torturous path. This increase in tortuosity led to a drop in permeability value. Conversely, in the case of *Cd-RVE*, with an increase in fiber volume fraction, there is no such effect. The only decrease in permeability is caused by the packing of fibers. The empirical models were identified in the form of exponential functions as presented in Equation 5.14, where i represents the fiber diameter distribution, a and b are model constants and V_f is the fiber volume fraction. Using the curve fitting module in Matlab, model constants for both the curves were identified and are presented in Table 5.1 with 95% of significance ($R^2 = 0.985$).

$$K_{rve,i} = a \exp(b V_f) \quad (5.14)$$

RVE type	a	b
Constant fiber diameter	1.102e-10	-8.179
Variable fiber diameter	1.879e-10	-9.689

Table 5.1: Model constants (Equation 5.14) identified using curve fitting.

In order to validate these numerical results experimentally, a UD flax fabric similar to that in Chapter 3 is used as reinforcement. This UD tape can easily mimic the tow geometry as all the fibers are aligned in one direction, the transverse permeability can be measured easily. A rectangular preform of dimensions $12 \times 12 \text{ cm}^2$ is cut and weighed to measure the areal weight of the fabric. The variability of the areal weight of this UD tape is shown in Figure 5.9. The values characterized, and the one provided by the supplier is not the same. Therefore an average areal weight of the plies is calculated, and this value

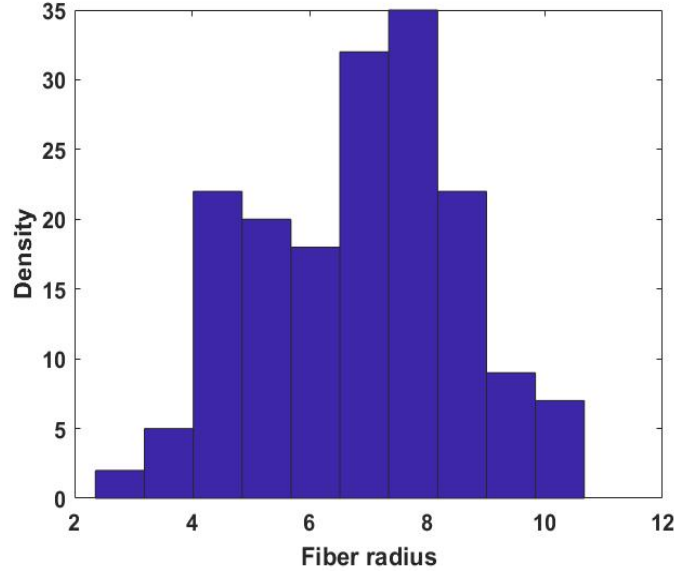


Figure 5.7: Distribution of fiber diameter in a RVE with 30% V_f

is used to estimate the fiber volume fraction of preform instead the one with a constant areal weight. The fiber volume fraction is varied by varying the number of plies(n) in the preform. The tests were repeated at least five times for each n . Unfortunately, only the unsaturated permeability of these plies is measured as the measurement of saturated permeability is difficult due to two main reasons. Firstly, the measurement of mass flow rate is an issue. There is no steady flow, and even if there is, the time to reach the steady state was very long. Secondly, the measurement of the mass of the test liquid was not possible as the accuracy of mass balance was far from the range of mass outflow. Concerning the statements in Section 5.1, the experimental results were plotted against the fiber volume fraction along with different permeability models presented in section 5.1.

In order to characterize permeability of reinforcement, unidirectional flow experiments are conducted on a test bench consisting of thick steel plate (bottom) and a transparent upper mold (see Figure 5.8). Mold deflection during injection is avoided by using a four-centimeter thick acrylic lid. The volume fraction of reinforcement is controlled using spacer plates between molds. Engine oil (provided by Mobil DTE) is used as test liquid in this study. The viscosity of oil is measured before each injection with a Brookfield viscometer and was found to be 130 ± 5 mPa.S at 23°C . The achieved pressure gradient is measured with the help of pressure transducers situated near the inlet and outlet of the preform. Four different fiber volume fractions are tested to obtain unsaturated permeability. The experiment is repeated at least three times for each test condition.

In Figure 5.11, the validity of these existing analytical models can be evaluated. The

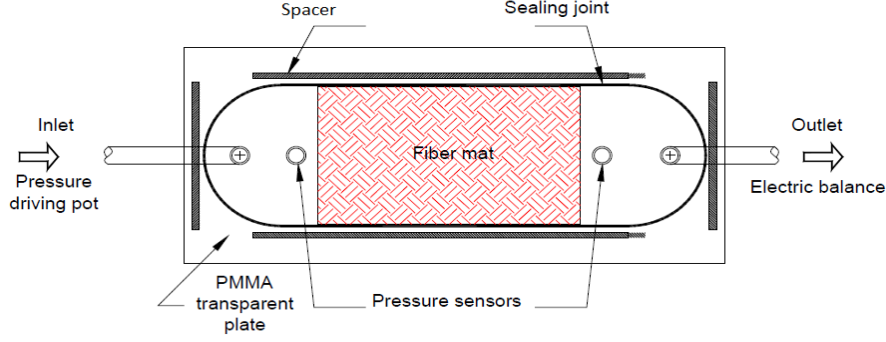


Figure 5.8: Schematic of permeability bench

analytical models available in literature take into account a constant fiber radius, but in the case of flax fibers, the radius is not constant. Therefore, the permeability values are calculated for radii between $7\text{-}10\mu\text{m}$ [Figure 5.11]. Recently, Zarandi et al.[175] made an effort to validate the existing permeability models. It was observed that the models suggested by Tamayol and Bahrami with the hexagonal arrangement were under predicting the permeability values where the model for the square arrangement agreed with experiments with glass fiber tows. Similar results were obtained in this study. In Figure 5.11, it can be easily noticed that the models by Berdechevsky and Cai [178], Knackstedt and Du Plessis [182] and Tamayol and Bahrami [180] (hexagonal arrangement) do not match the experimental results. Berdechvsky and Cai's model over predicts the transverse permeability by one order of magnitude. The experimentally characterized transverse permeability values are quite dispersed even for a constant number of plies. As pointed out, this is caused due to the irregularity of the flax tape. On a smaller scale, the variability of the preform stands out but whereas when the larger samples are used, the variability is compensated as observed in [189–191]. Nonetheless, these analytical models are based on the assumption that all fibers have a constant cross-sectional area and cannot be used for permeability estimation of flax fibers. It can be argued that a range of plausible permeability values can be obtained using one of the models by varying the radius of the fiber and the calculations for fill time or void formation can be made in a stochastic manner but that range of values will be very high and will not be a match to reality.

For this numerical approach to characterize transverse permeability, the experimental results are still not in agreement with numerical simulations. Even after imposing a normal distribution to fiber diameter, the experimental results are about 18% lower than the numerical results. This difference can be a result of omitting the real phenomena which occur during the impregnation of flax fibers, i.e., liquid absorption and swelling. Usually, the fiber swelling phenomena can be omitted as the impregnation time for a tow

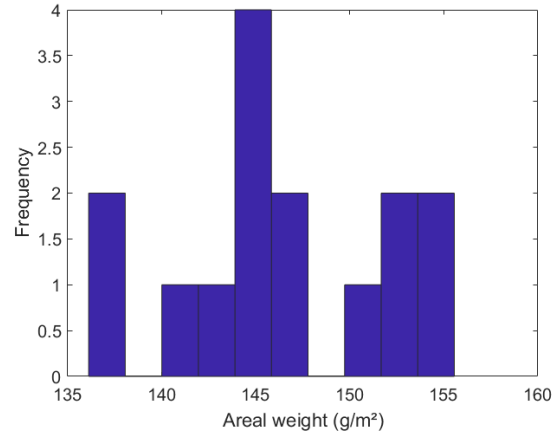


Figure 5.9: Variation of areal weight of UD flax tape

is very short compared to the time required for fibers to swell. Nonetheless, to avoid this issue, engine oil is considered, which led to a less significant swell rate and the maximum swell ratio of 1.04. Conversely, the phenomenon of liquid absorption takes place during the impregnation of fibers, which decreases the liquid velocity, thereby affecting the estimation of unsaturated permeability. If this loss of mass can be considered for in the numerical model, it can be expected that the difference between the experimental results and model can be decreased.

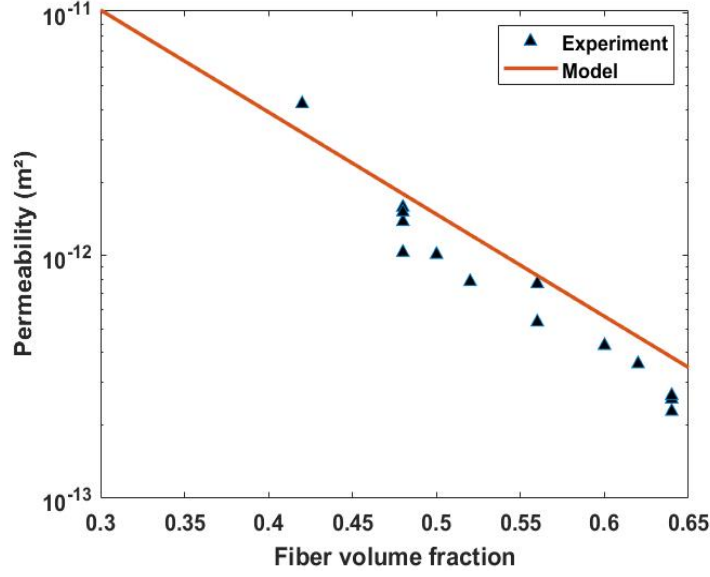


Figure 5.10: Comparison between experimental and numerical results for transverse permeability of UD flax tow

5.2 Void formation in flax fiber preforms

5.2.1 Experimental procedure

A 3X3 twill weave fabric, Nattex 400 provided by Dehondt Technologies, France is used as reinforcement and epoxy resin, Prime-27(Gurit) with Prime 20 hardener is used as matrix. The areal weight of fabric and density of fibers are $400g/m^2$ and $1.52g/cm^3$, respectively. The fabric is dried at $80^\circ C$ for 6 hours to remove the moisture content and is not subjected to any further treatment before injection.

The permeability of the fiber preforms are characterized using the same setup presented in Subsection 5.1.5 (Figure 5.8). In this case, both unsaturated and saturated permeabilities were characterized for same fiber preform. The results were plotted against fiber volume fraction and were fitted to the model suggested by Nguyen et al.[43] (Equation 5.15) in order to identify the model constants. This step helps in defining the preform permeability in the in-house numerical code.

$$K = \frac{(1 - f_{sw}^2 V_f)^{n+1}}{A f_{sw}^2 V_f^n} \quad (5.15)$$

Composites are manufactured using an in-house aluminum mold with dimensions $270 \times 290 \times 2.6mm^3$. The mold is set up in such a way that the resin injection is linear and without race tracking. Four layers of fabric are stacked in the mold, and the mold is closed with the help of a hydraulic press. A compaction pressure of 6 bars is applied on the mold to ensure the final thickness of the composite and also no resin leakage. The

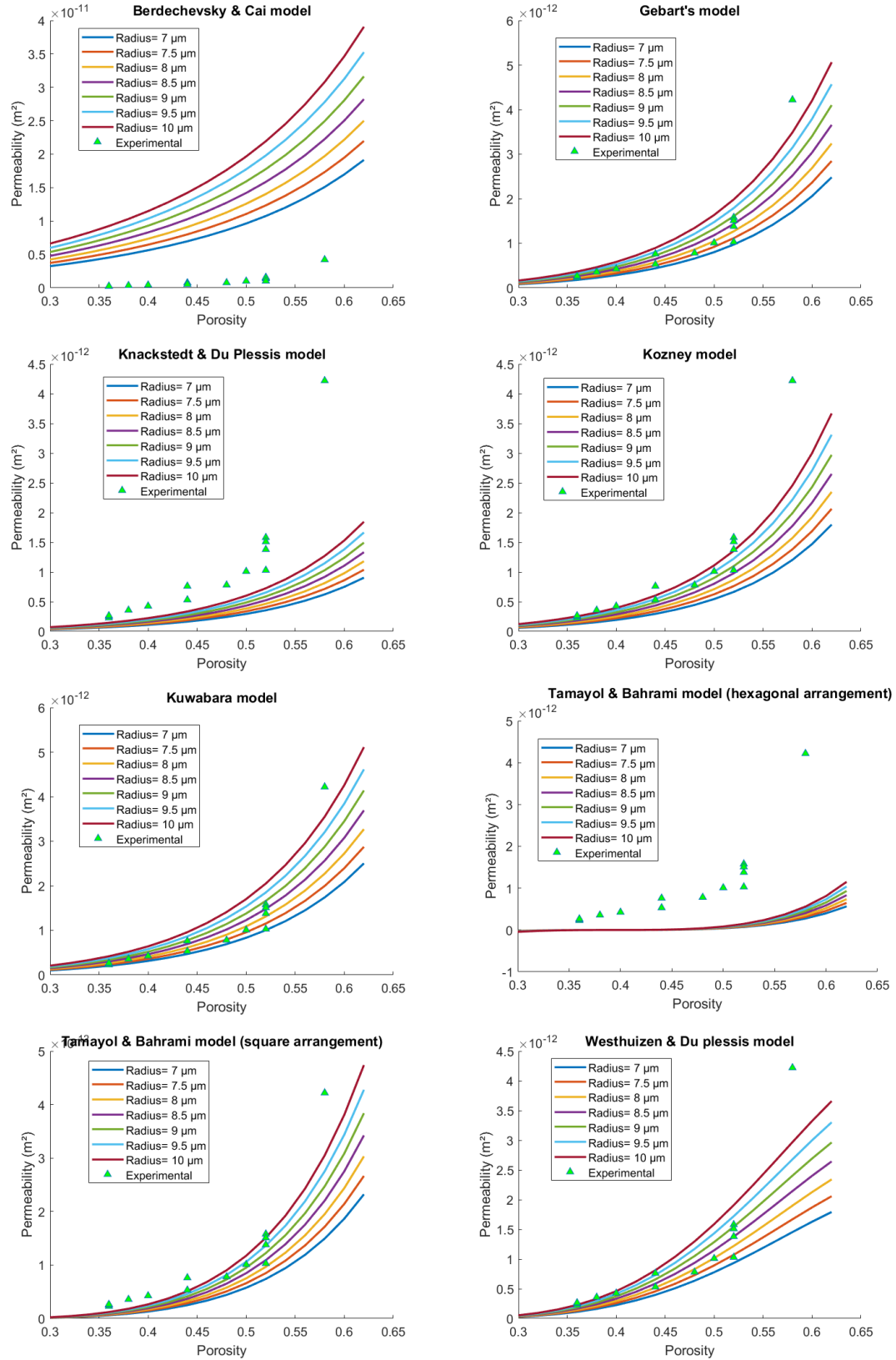


Figure 5.11: Permeability prediction with different analytical models with different fiber radii

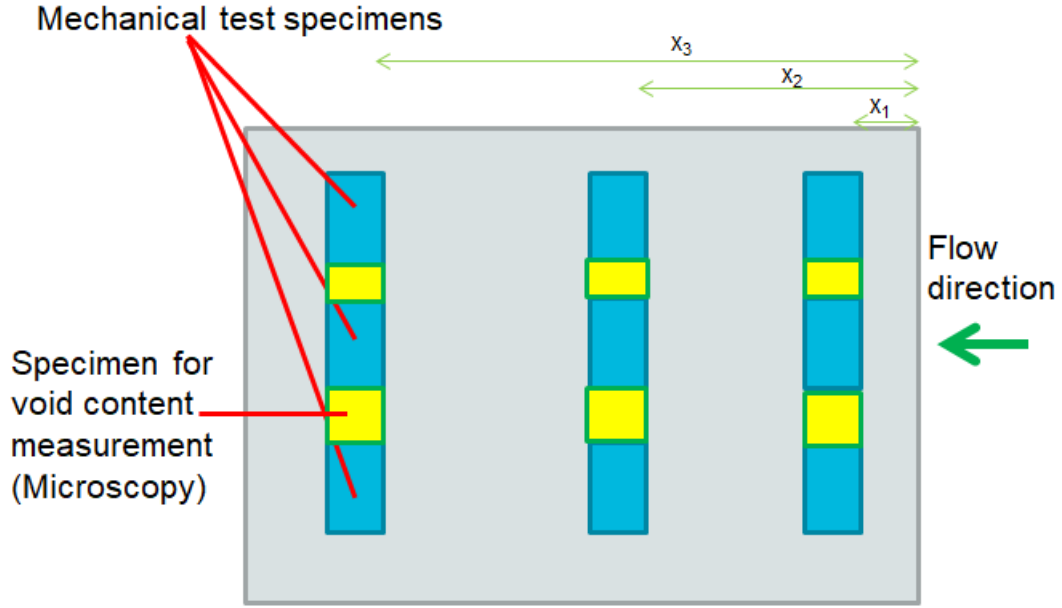


Figure 5.12: Schematic of specimen extraction points from manufactured plate

resin is injected at three different injection pressures 1bar, 1.5bar, and 2.0 bar. All plates are manufactured at room temperature and are cured at room temperature for 17 hours and then post-cured in an oven at 65C for seven hours. For each injection pressure, at least three plates are manufactured to ensure the repeatability of the process.

In order to characterize the local void content, specimens are extracted from the composite plate at specific distances from injection point (see Figure 5.12). These specimens are cast in a resin block and are polished using sandpapers (grit size varying from 80 to 4000) and are finished with diamond polish. The micrographs of polished specimens were acquired using an optical microscope. These images are then converted into binary images using FijiJ [192]. The binary images are compared to the original image ensure the absence of noises, and if any, they are removed manually. As voids are represented as black pixels, the void content is evaluated as a ratio of the number of black pixels to the total number of pixels in the image, which is easily calculated as area fraction.

5.2.2 Modeling of void formation in flax fiber preforms

It was mentioned in the previous sections that the primary source of voids during liquid composite molding is air entrapment. In this study, the approach suggested by Park et al. [35] is utilized with some modifications in governing flow model and initial set-up. It is known that the flow in natural fiber preforms is different from that of glass fiber preforms as pointed out in Chapter 2. In this study, the model suggested by Nguyen et al. [1] is

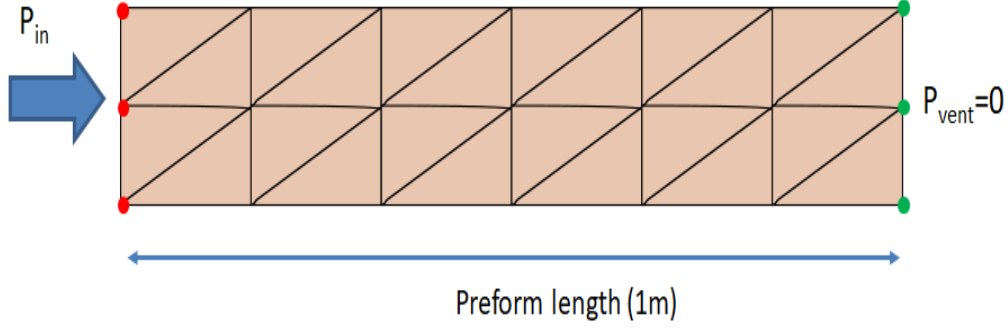


Figure 5.13: Applied boundary conditions on the numerical model

used both at tow and preform scale.

$$\nabla \cdot \left(- \frac{K(t, x)}{\mu} \frac{\partial P}{\partial n} \right) = S(t, x) \quad (5.16)$$

$$\nabla \cdot \left(- \frac{K_T(t, x)}{\mu} \left(\frac{\partial P}{\partial n} - \frac{P_c}{l_T} \right) \right) = S_{micro}(t, x) \quad (5.17)$$

where S , S_{micro} is the sink source term at a distance x for a given time t for the macroscopic flow and for the tow flow respectively. The difference between these two terms is just the time scales at which the phenomena of liquid absorption and fiber swelling occur. The permeability $K(t, x)$ refers to the unsaturated permeability of the preform [68, 70] whereas $K_T(x, t)$ is the tow permeability which is also a function of time and distance. An argument can be made that the influence of fiber swelling on the tow permeability can be neglected because the fill time for a single tow is relatively very short when compared to the composite. Also, the difference observed in numerical simulations is quite insignificant. Nevertheless, both fiber swell and liquid absorption were considered in the model. The Equations 5.16, 5.17 are solved using the numerical setup described earlier. The sink source term S_{micro} is defined at fiber level and is expressed as

$$S_{micro} = \frac{V_{f,i}}{1 - V_{f,i}} \left[\frac{2a_2c_2}{(b_2t + c_2)} e^{\frac{2a_2t}{b_2t+c_2}} - \frac{\rho_f}{\rho_l} C_R (a_1b_1e^{-b_1t} + c_1d_1e^{-d_1t}) \right] \quad (5.18)$$

where a_1 , b_1 , c_1 , d_1 are model constants for liquid absorption and a_2 , b_2 , c_2 are model constants for fiber swell, C_R is the maximum retention ratio and $V_{f,i}$ is the initial fiber volume fraction. The values for these model constants are presented in the Table 5.2 which are experimentally characterized. Similarly, the sink (S) term in Equation 5.16 is expressed as:

$$S = \frac{V_f}{V_{f,T}} \frac{\frac{2K_{eq}P_c}{\mu R_T^2} - \frac{S_{micro}(x^2-1)}{2} + S_{micro}x^2 \ln(x)}{\ln(x)} \quad (5.19)$$

The imposed boundary conditions on the numerical model are depicted in Figure 5.13.

Model constant	Value
a_1	0.144
b_1	0.012
c_1	0.856
d_1	0.314
a_2	0.015
b_2	0.233
c_2	29.99
C_R	0.15

Table 5.2: Model constants for sink terms in Equations 5.16 and 5.17

The estimation of void formation is carried out using the basic principles of comparing the time scales for the resin to transverse a length (l_T) in the channel and inside the tow. Once, the time scales are calculated, depending on their ratio, the origin of voids can be attributed either to the tows (V_{tow}) or the channels ($V_{channel}$) as follows:

$$\Delta t_T > \Delta t_C : V_{tow} = h_{tow} \cdot v_T (1 - V_{f,T}) \left(1 - \frac{\Delta t_C}{\Delta t_T}\right); V_{channel} = 0 \quad (5.20)$$

$$\Delta t_T < \Delta t_C : V_{channel} = h_{ch} (1 - v_T) \left(1 - \frac{\Delta t_T}{\Delta t_C}\right); V_{tow} = 0 \quad (5.21)$$

Where Δt_T , Δt_C are the time scales for the resin to travel a distance of l_T in tow and channel respectively. h_{tow} and h_{ch} are the void shape factors in tow and in the channel. v_T is the tow volume fraction and $V_{f,T}$ is the fiber volume fraction of the tow.

After the formation of air bubbles, two phenomena can occur simultaneously or independently. First, the air bubbles' size can change due to the surrounding resin pressure, which varies with time. As the flow front advances, the resin pressure surrounding the air bubble will increase from $P(t, x)$ to $P(t + \delta t, x)$ leading to a decrease in the volume of the air bubble from $V_{void}(t, x)$ to $V_{void}(t + \delta t, x)$, according to ideal gas law (when temperature is constant) which can be expressed as:

$$V_{void}(t + \delta t, x) = \frac{P(t, x)}{P(t + \delta t, x)} V_{void}(t, x) \quad (5.22)$$

Void formation models in the literature tend to ignore post-formation bubble migration which is an other important phenomenon. This void migration greatly influences the void content estimated using these models. Many bubbles, especially the smaller air bubbles in tows, remain trapped because the highly compact reinforcement architecture hinders their movement [55, 61]. Conversely, the air bubbles, located in the channels where the permeability is relatively higher, they manage to escape from their initiation point, and

are transported quickly toward the flow front along the negative pressure gradient [52]. Such bubble mobility depends on the inter-bundle gap width, the applied pressure, and the bubble size. In case the bubbles are large enough to be lodged, as the resin pressure continues to increase at a given location during the filling time in LCM, the bubbles decrease in size by both the ideal gas law and dissolution until the bubble is small enough to escape. In general, bubble mobility describes whether bubbles will move faster or slower than the surrounding resin flow, thereby aiding in the prediction of the final location and size of a bubble after formation. Due to the difficulty in the experimental observation of bubble motion in a flax fiber preform, limitations of time, the void migration model is not implemented in the current study. In order to understand the difference between existing models and this study, the analytical model (Equation 5.23) suggested by Geuroult et al. [68] is used to compare the estimated void fractions.

$$\frac{\Delta t_T}{\Delta t_C} = \frac{K_M}{K_T}(1 - V_{f,T}) \left[1 - \frac{FK_M V_{f,T}}{D_f(1 - V_{f,T})L_T Ca^*} \ln \left(\frac{D_f(1 - V_{f,T})L_T Ca^*}{FK_M V_{f,T}} + 1 \right) \right] \quad (5.23)$$

5.3 Results

5.3.1 Permeability of flax fiber preforms

In Figure 5.14, the model (Equation 5.15) shows agreement with the experimental values. The deviation at higher volume fraction from the expected value is caused by limitation of the model, as the model assumes that fibers swell to their maximum irrespective of the fiber volume fraction[43].

Figure 5.15 shows the ratio of unsaturated permeability (K_{unsat}) to saturated permeability (K_{sat}) versus fiber volume fraction (V_f). It can be noticed that at low V_f , the ratio is closer to one whereas, with an increase in V_f over 40%, the ratio decreases to 0.82 and lowest value of 0.78 at 53% V_f . This difference in the permeability ratio can be attributed to the delay in the saturation of fiber tows at a high V_f . The tow saturation at higher V_f takes longer due to the low permeability, and this might be the reason for this difference in permeability ratio. Also, for flax fibers, the phenomenon of liquid absorption and fiber swell can be directly related to V_f , which greatly affects the flow front advancement. Similar results were presented by Francucci et al. [48], although the fiber type is not the same, while the phenomenon of impregnation is the same as the flax fibers. At 55% of fiber volume fraction, they reported a ratio of 0.715, which is close to the value found in Figure 5.15. In literature, it is hypothesized the void formation causes this difference in permeability ratio during impregnation [39].

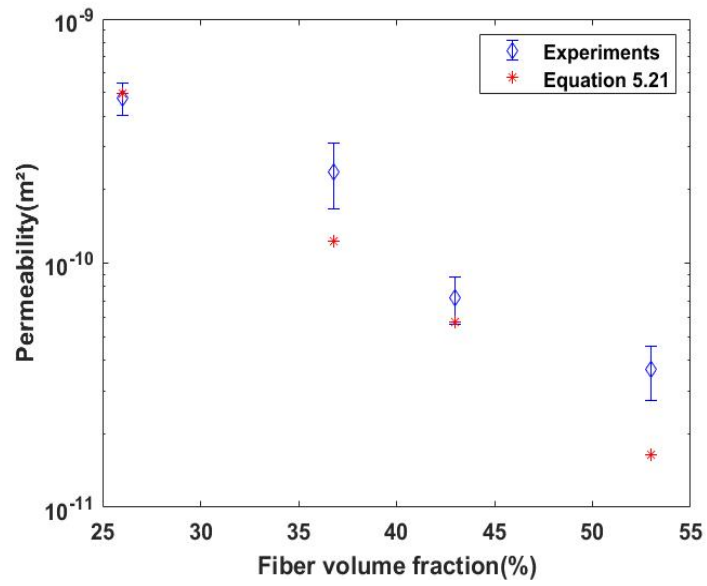


Figure 5.14: Saturated permeability vs fiber volume fraction: experimental results and model

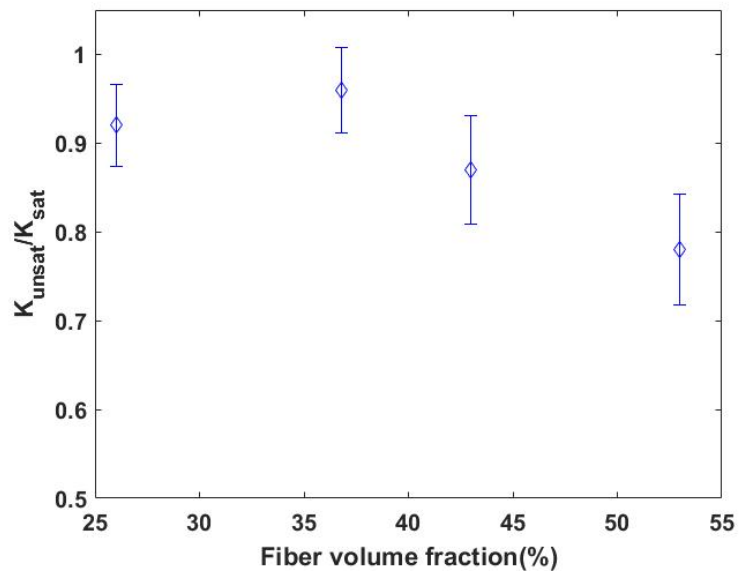


Figure 5.15: Ratio of unsaturated permeability to saturated permeability vs Fiber volume fraction

5.3.2 Effect of local variability on void formation

Due to the high variability of tow porosity of flax fiber preform, three different fiber volume fractions (0.53, 0.58, 0.63) were used to estimate the influence on void content. For the selected three different fiber volume fractions, the tow fill times were approximately 6.7, 8.4 and 10 seconds. Figure 5.16 represents the variation of the void fraction with different tow fill times versus modified capillary number. These simulations were conducted over a preform with 42% global fiber volume fraction impregnated with epoxy resin with a constant injection pressure of 2 bar. Here it can be clearly distinguishable that the variation in tow porosity greatly influences the process window. In case of highly porous tows ($\phi \approx 46\%$), the optimum $Ca^* = 0.0087$ but for tows with low porosity, the optimum $Ca^* = 0.005$. As these two porosity values are extremities, it can be assumed that for a flax fiber preform with 42% of fiber volume fraction, the optimum capillary number lies between 0.0052-0.0087. In the current case, the preform porosity is assumed to be unchanged, and only the variation in time ratios in Equation 5.24 and 5.25 were used to estimate the void formation. Nevertheless, if in case the local preform variation itself is highly varied due to fabric irregularities, will the optimal capillary number still lie in the same range as above mentioned? In order to answer this, a study on local variability is carried out where the tow porosity is assumed to be constant while the porosity variation is caused by variation in tow and channel widths.

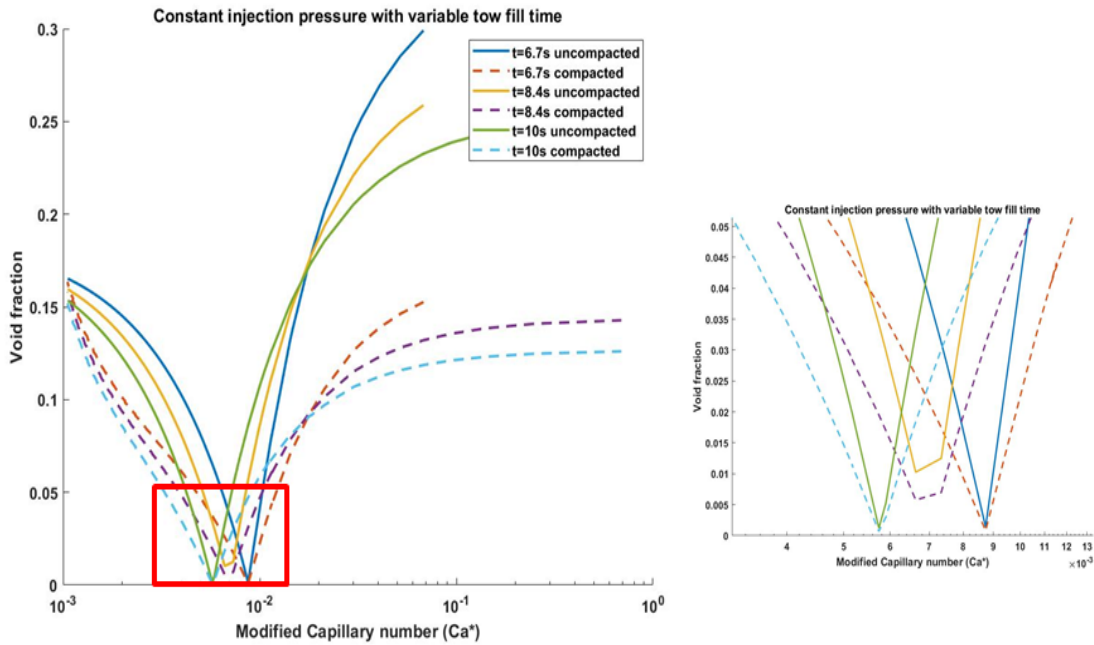


Figure 5.16: Variability of void content with tow fill time

Using the in-house numerical tool [35], the influence of local variability of porosity in a flax fiber preform can be investigated. It is in fact proven that in glass fiber preforms, the

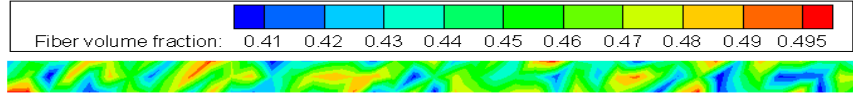


Figure 5.17: Contour plot of a random flax fiber preform with mean $V_f = 42\%$

variability of fiber volume fraction within a tow changes from position to position[193]. Similar variability is observed in the case of flax fiber tows. Nguyen [194] found that the tow porosity varies between 35% to 40%. Even if efforts are made by the textile manufacturer, the physical characteristics of tow cannot be maintained constant. The width and linear tex are highly varied from tow to tow. In the current study, the tow porosity of Nattex 400 is estimated using micrographs and image processing. The values were found to be similar to the values in [194] despite larger tow width. The linear weight of the warp and weft tows were similar to each other with a value of $195 \pm 12g/m$. This variation can be supported by the irregularity in fiber lengths. This local variations in the tows account for different tow permeability, thereby affecting the local flow.

Taking this into account, this variability in initial porosities is imposed by imposing different porosity values for each node. Normal distribution of tow porosities with mean around 0.42 and standard deviation of 0.06 is used to generate porosity values for each node and the element porosity is calculated as an average of the three nodes (see Figure 5.17). It should also be noted that in reality, this variability in porosities will lead to different fiber swell ratio but in the current scenario, this is not considered. Therefore a homogeneous fiber swell evolution is assumed. The computational domain is one meter long, which is sufficiently great to understand the influence of local variations. The domain consists of 602 elements, each with a length of $5e-3$ m. The domain is maintained constant for 10 runs but the porosity is varied. The numerical results can be seen in Figure 5.18. Even though the scatter in the flow front is small during the first 200 seconds, a difference can be observed in the final fill times. A difference of 6.7% in fill time can be observed which accounts to 12 minutes. Considering the length of the part, this difference may not seem significant but this can help us draw two interesting statements. First, this implementation of variable porosity values to the finite elements can provide an range of estimated fill times which can be expected during manufacturing of composites. This difference will help in proper selection of inlet and vent placements and inlet conditions. On the other hand, this difference in fill times can be also utilized to estimate the range of optimum flow velocities to minimize the void content. In Figure 5.18, it can be noticed that despite a difference of 6.7% in final fill time of the preform, the range of optimum capillary number is observed to very small. In fact, this implies that even if the porosity is normally distributed over a preform, the optimum injection conditions are still remain

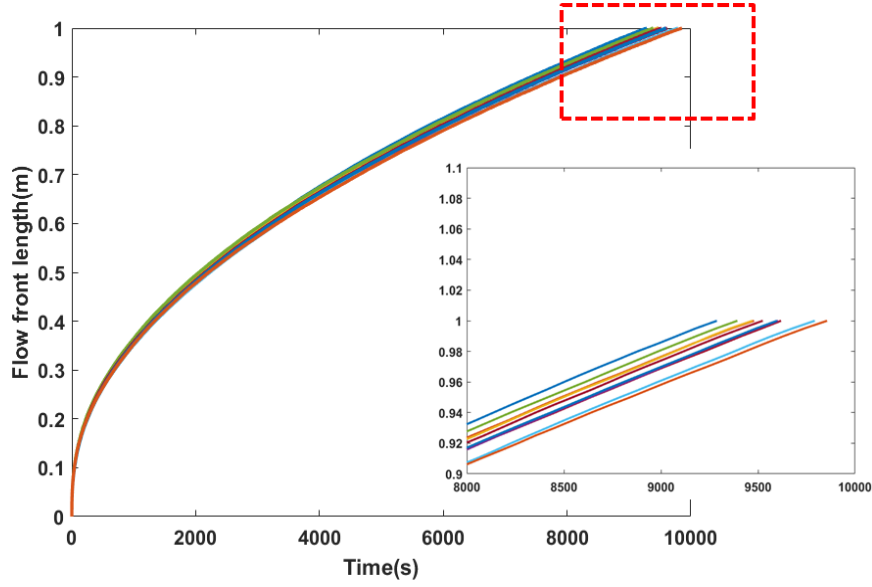


Figure 5.18: Influence of variation in local porosities on fill time

as if the initial porosity content is constant. Nonetheless, assuming that these variations are caused by tow porosity, then there might be a shift in the optimum capillary number which should be investigated.

5.3.3 Comparison of the current model with model in literature

The parameters used to predict the void content are presented in Table 5.3. In Figure 5.20 it can be observed that the model proposed by Geuroult et al. [68] predicts almost the same void content as Equations (5.22-5.26). The main difference is that the lowest void content was predicted at $Ca^* = 0.01$ for model where fiber swell and liquid absorption was not considered whereas the proposed model predicted the lowest void content at $Ca^* = 0.005$. Thus, this difference can be related to the delayed impregnation of tows in the case of flax fibers. Also, the unsaturated permeability of natural fibers is lower as fibers act as sinks, removing the fluid from the main stream as it travels along the preform. Nevertheless, the observed optimum capillary number is with the range of values suggested in the literature (10^{-2} - 10^{-3}). In Figure 5.20, it can be noticed that the volume of tow void formation is very high compared to that of the model suggested for non swelling porous media. This is due to the fact that in the case of flax fibers or any natural fibers, the fiber bundles exhibit high capillary pressure. It should be noted that the transition from tow to channel void content is sharper when compared to the model proposed in [68]. This indicated that finding the process window for natural fiber preforms is narrower than that of glass fibers.

The experimentally characterized void contents also show the similar tendency but are

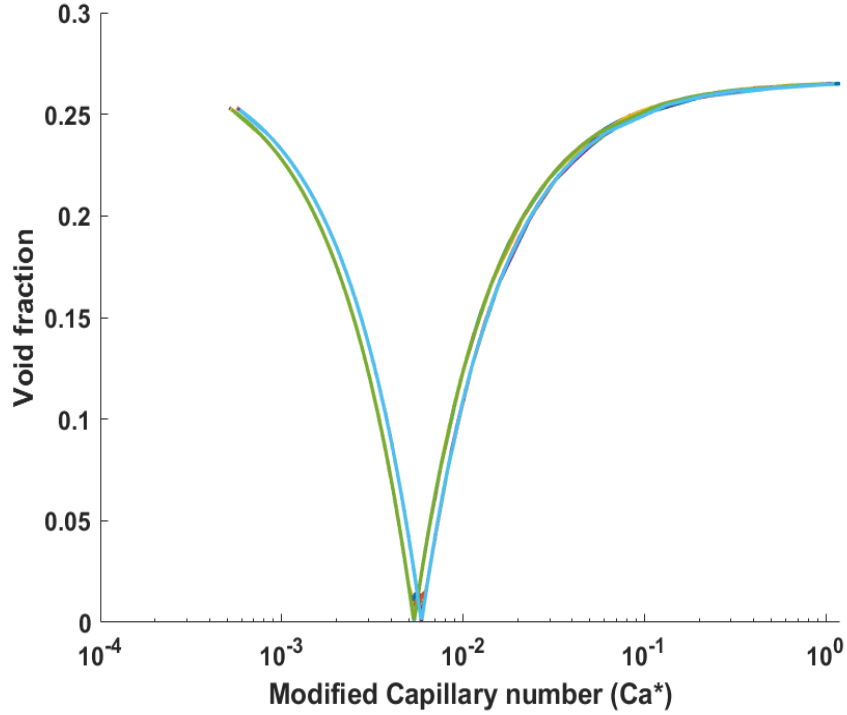


Figure 5.19: Effect of local variations in porosity of flax fiber preform on void formation

not an exact match to the predicted void contents. This is because the model implemented omitted the phenomenon of void transport, which greatly affects the prediction of final void content [52]. It is the reason why the void content near the inlet had lower void contents (around 1%). The air bubbles formed near the inlet might have been transported along the flow. However, the void content is highest at the end of the plate which is usually the case when the transported voids get lodged at the bottom of the plate. This is in agreement with the studies in literature [54, 67]. Another factor that this model lacks is the void migration from tow to channel. Figures 5.24-5.27 present different voids the manufactured plates. In Figure 5.24, it can be observed that the voids in the tows are transported out of the tows and entering the channel indicating the phenomenon of void migration. The void content observed before the optimal capillary number were mostly tow voids (see Figure 5.21, 5.22), whereas in the downstream, the contribution to the total void content was by channel voids (Figure 5.26). These results are however contradicting to the results presented by Pucci et al. [167] in the literature where the authors stated that when flax fiber preforms were infused with a bio-based resin, almost zero channel voids were observed. On the other hand, Shah et al. [195] observed that during LCM of jute preforms at low fibre content, due to low tow permeability but high macroscopic preform permeability, the global void content is dominated by tow contribution whereas, at higher fiber volume fractions, capillary flow in the yarn dominated the flow leading to

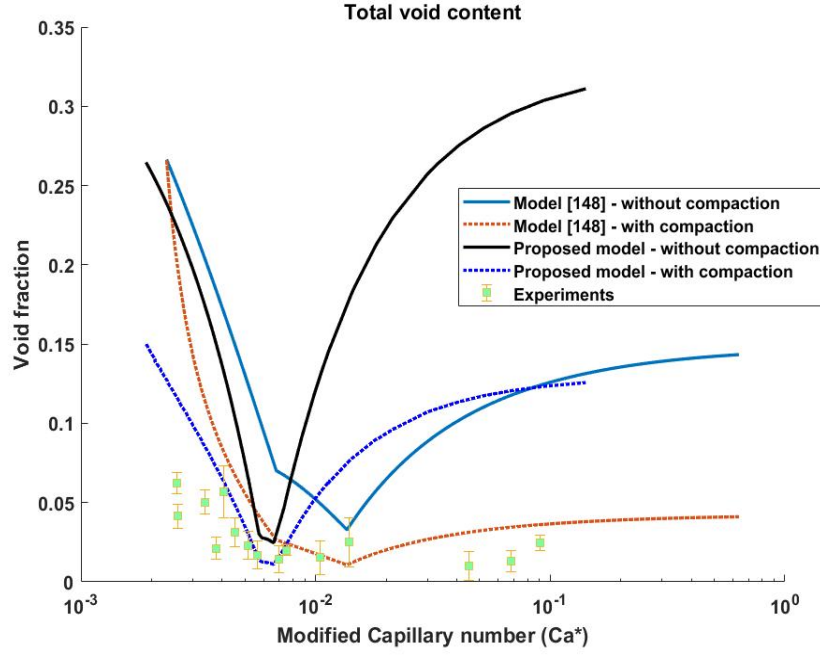


Figure 5.20: Comparison between expected and experimental void content

a higher content of channel voids. In this current study, the global fiber volume fraction is maintained constant therefore, this phenomenon cannot be observed.

Parameter	Value
Macropore permeability (K_M)	$6.85e-11m^2$
Fiber volume fraction of preform (V_f)	0.43
Single tow length (L_T)	6mm
Fiber diameter (D_f)	$15\mu m$
Fiber volume fraction of tow ($V_{f,T}$)	0.63
Void shape factor in channel(h_{ch})	0.7
Void shape factor in tow(h_{tow})	0.7

Table 5.3: Preform properties used for void formation and compaction modeling in Figure 5.20

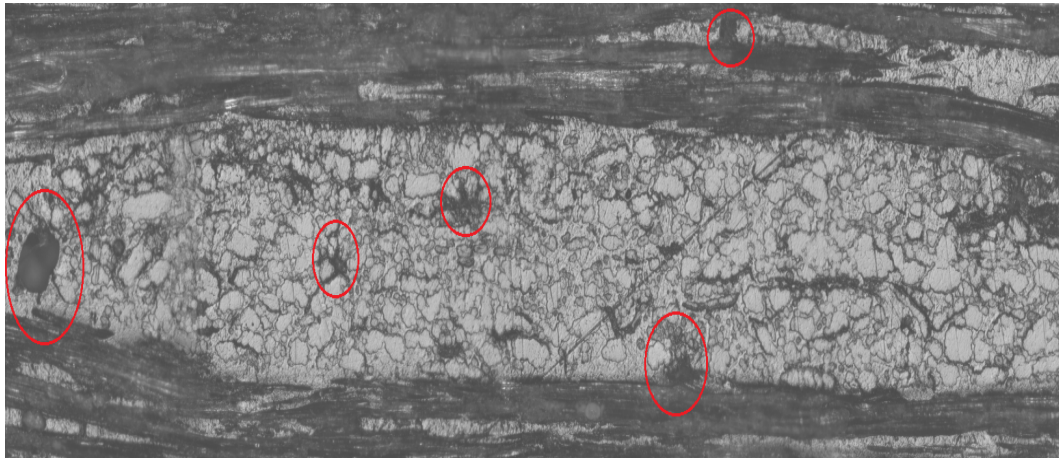


Figure 5.21: Tow voids near the inlet of the plate manufactured with 2 bar injection pressure

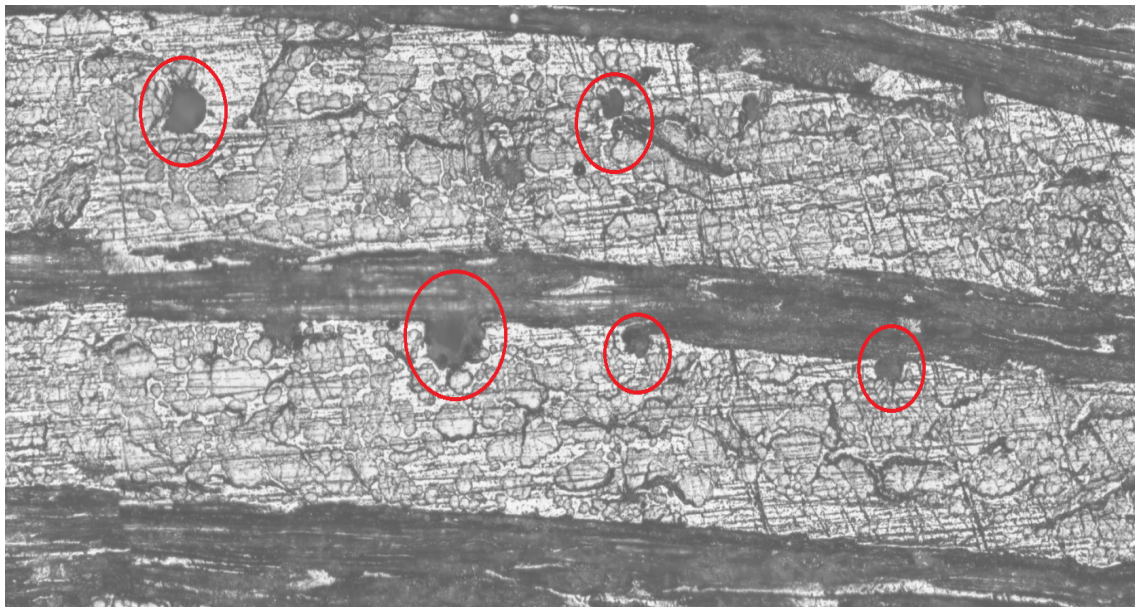


Figure 5.22: Tow voids near the inlet of the plate manufactured with 1.5 bar injection pressure

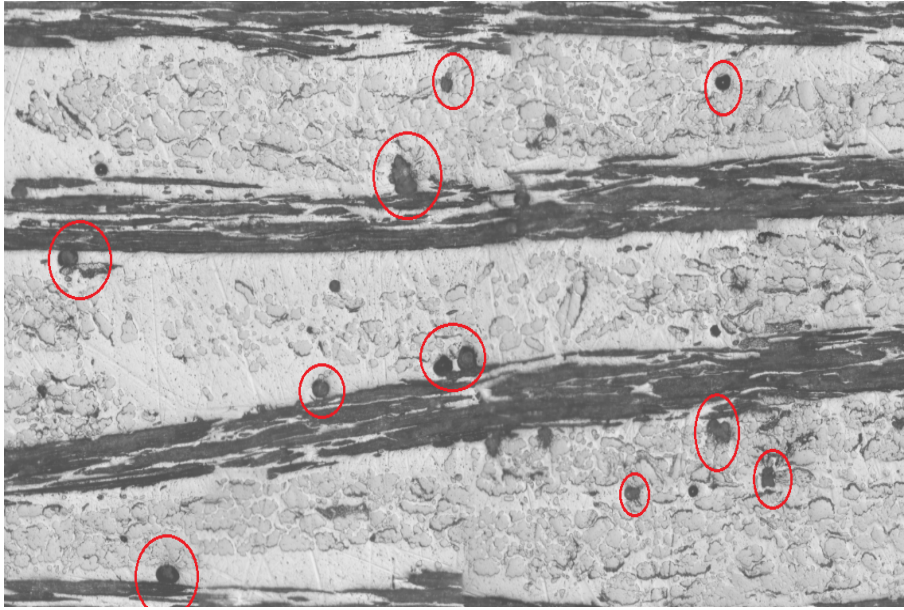


Figure 5.23: Channel voids observed at the central section of plate manufactured with 1.5 bar injection pressure

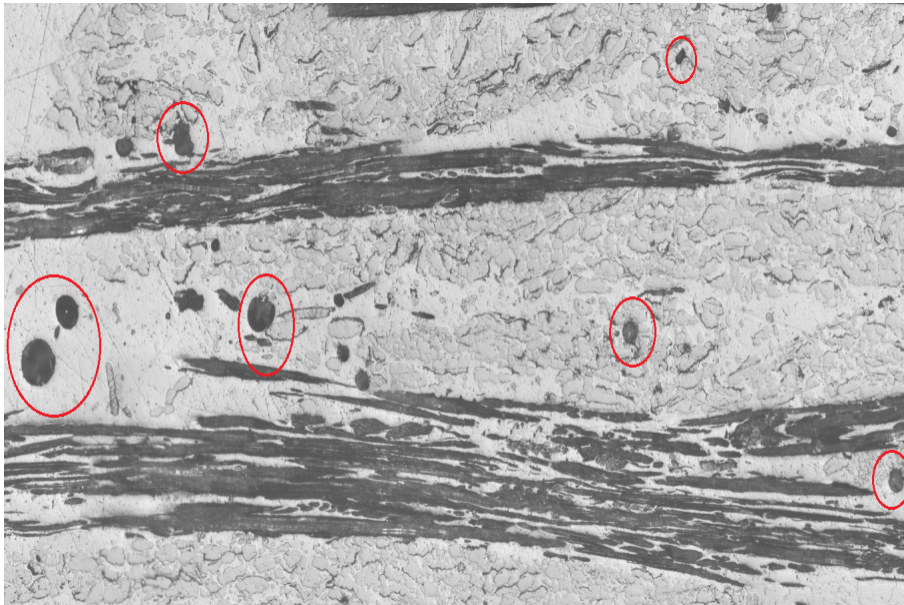


Figure 5.24: Channel and tow voids observed at the central section of plate manufactured with 1 bar injection pressure in weft direction

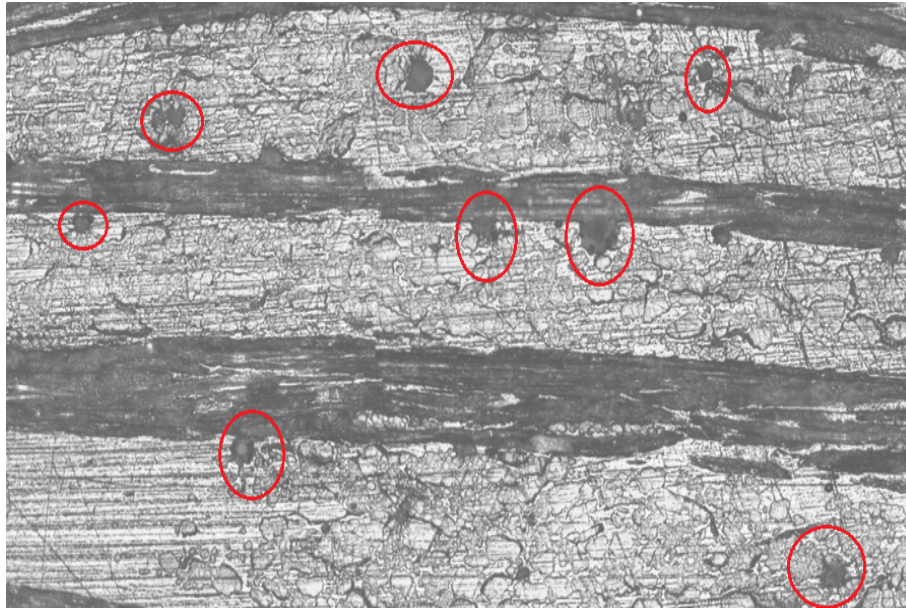


Figure 5.25: Channel voids observed at the central section of plate manufactured with 1bar injection pressure



Figure 5.26: Large voids near the vent

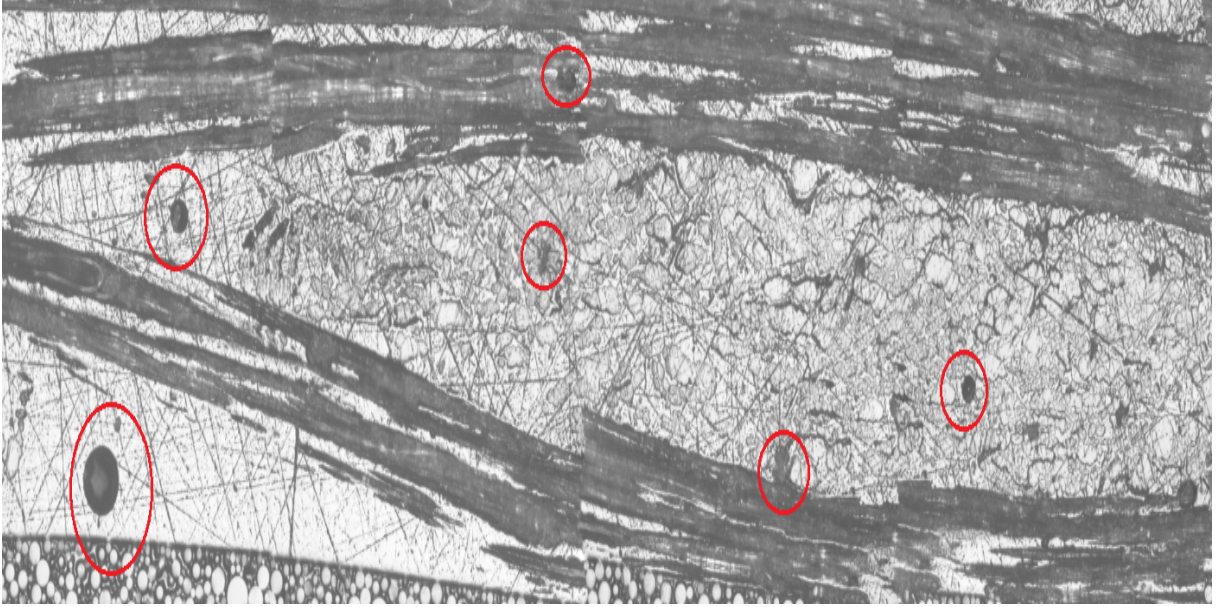


Figure 5.27: Voids near the inlet

5.4 Conclusions

In this chapter, it has been proven that the classical approach for tow permeability can be rarely used because the experimental and analytical results do not match. However, numerical tools can be helpful to predict the tow permeability in the case of flax fibers. A model was suggested based on the numerical simulations, and it was showed that there is a decent match between the model and experimental results. Only in the case of high fiber volume fraction, the model deviates from the experimental results, which were attributed to the phenomenon of liquid absorption. In order to consider this effect, a numerical model should be considered where fibers act as resin mass sinks. In the second part of this chapter, modeling of void formation and compression in flax fiber preforms was discussed. The influence on the variability in local porosities and tow fill time on void content was discussed. Finally, an overall void prediction curve was compared with the experimental results and was found that the observations localized near to the injection point did not match the model, but the model was in agreement with the observations which were far from the inlet indicating the phenomenon of void transport. Thus the next step would be adding a void transport module to the existing numerical setup to understand accurately predict the void content in the final part.

Chapter 6

In-service behaviour of flax fiber composites

6.1 Introduction

The investigation of the evolution of both mechanical and physical characteristics of composite material in real-life conditions helps in providing a final verdict into their implementation as a structural part for commercial use. The physical evolution during aging of composites can be linked to the dimensional variations, the creation and propagation of the micro-cracks and the swelling of both resin and fibers. In the case of carbon or glass fiber reinforced composites, the matrix is the only susceptible component to humidity, and it absorbs water causing volumetric expansion, i.e., swelling which results in an increase of stress at the interface leading to debonding of fiber and matrix [196–198]. It is said that these changes could be either temporary or permanent depending on the aging duration and the exposure to humidity [199]. The combination of these mechanisms can lead to the degradation of mechanical performance of the composite. It was also observed that the repetitive cycles of absorption-desorption cause a change in the diffusion coefficient and the saturation limit. In the case of carbon/epoxy composites, after three cycles of absorption-desorption, the saturation limit was increased by 28%, and the diffusion coefficient was increased by 100% [199]. It was stated that this was caused by the permanent damage of matrix due to repeated expansion and shrinking [197].

The moisture uptake by composite materials usually involves two steps. First, the water infiltrates the polymer matrix and then by capillarity along the micro-cracks and crevices around the fiber-matrix interface. The latter is the phenomenon which degrades the fiber-matrix interface [200]. Generally, in the case of glass or carbon fiber reinforced composites, the critical parameters during accelerated aging are the temperature and humidity. Temperature helps in faster diffusion of moisture into the composite whereas

the humidity content sets the maximum absorption value. This is applicable to both the cases where the composite specimen is either submerged in a water bath or placed in a conditioning chamber. Constant monitoring of the water uptake by these composites provides an insight into the kinetics of diffusion of water which can later influence the mechanical or physio-chemical behavior of composites. During the water diffusion into the composite, two phenomena are likely to occur [201]. An irreversible phenomenon which is usually referred to as the physicochemical behavior and a reversible phenomenon where the properties can be recovered by drying the material. Regazzi et al. [201] also stated that there is a limit of conditioning time to make the property reversible. Once the conditioning time exceeds this threshold, the material starts to degrade permanently.

Understanding aging mechanisms and the development of their descriptive models are needed for the use of natural fiber composites. Unlike synthetic fiber-reinforced composites, natural fiber composites have two components viz. fibers and matrix, which are susceptible to moisture. Therefore, it is necessary to consider both the constituents during the prediction of the strength of these materials in the presence of moisture [202]. Of course, this is not easy because the degradation rates of these constituents are not the same, and the models should take into account such differences [203]. The difficulties are multiple because it is not only a matter of identifying the mechanisms of degradation specific to natural fibers in a humid environment but also a need to take into account the possible effects of the environment on these fibers according to their chemical constituents [204]. Chilali et al. [205] recently presented a numerical work investigating the swelling of natural fiber composites using a mesoscale RVE where they showed that at complete saturation, the internal stresses in the RVE are higher than that of the interfacial strength. Moisture diffusion into thermosets, notably epoxy resins has been widely studied in the literature [206–208]. It was stated that the diffusion coefficients are dependent of factors like temperature, cure degree, chemical composition, environment, etc. It was stated that the presence of fillers in epoxy also affects the diffusion behavior [208]. In case of epoxies, many diffusion models were applied among which Fick’s law of diffusion was the most common to describe this phenomenon. In the following section, a detailed description on the mechanisms of diffusion is presented.

6.2 Kinetics of diffusion

The progression of water molecules into polymer matrix governs the moisture uptake by composite materials into the empty spaces of polymer with hydrogen bonding [209]. These hydrogen bonds are stated to be continuously broken as the water molecules progress through the polymer’s free space. This process continues until the concentration of water

molecules is equal to that of the surroundings of the composite. The speed of diffusion of water molecules in a polymer depends on its diffusion coefficient (D), which is determined by the factors such as free space in polymer and the temperature of the surrounding atmosphere. There exist several analytical models in the literature which describe the moisture diffusion. Among these existing models, Fick's laws of diffusion and Langmuir are the most commonly used. Studies by [125, 205, 210] showed that the Fickian behavior could be used to explain the diffusion kinetics in flax/epoxy composites. Thus, in this study, we consider only the Fickian behavior, which is explained below.

6.2.1 Fick's law of diffusion

Adolph Fick in 1855 proposed a model to represent the diffusion of water molecules in a polymer network [211] by using two parameters diffusivity D and moisture concentration c , which can also be applied to the diffusion of water molecules in a polymer;

$$\frac{\partial c}{\partial t} = \text{div}(D \overline{\text{grad} c}) \quad (6.1)$$

Equation 6.1 cannot be analytically solved for a general cases. As in most studies however, considering a rectangular test specimen, the equation can be expressed in the Cartesian form as:

$$\frac{\partial c}{\partial t} = D_x \frac{\partial^2 c}{\partial x^2} + D_y \frac{\partial^2 c}{\partial y^2} + D_z \frac{\partial^2 c}{\partial z^2} \quad (6.2)$$

where D_i is the diffusion coefficient in x, y, z directions respectively. Crank in his study [212] has suggested various models for moisture diffusion.

$$\frac{C(t)}{C_\infty} = 1 - \frac{8}{\pi^2} \sum_{i=1}^{\infty} \sum_{j=1}^{\infty} \sum_{k=1}^{\infty} \frac{\exp(-\pi^2 t (D_x (\frac{(2i+1)^2}{l}) + (D_y (\frac{(2j+1)^2}{b}) + (D_z (\frac{(2k+1)^2}{h}))))}{((2i+1)(2j+1)(2k+1))} \quad (6.3)$$

where, l, b, h are length, width and thickness of the plate respectively, and $C(t)$, C_∞ are the moisture content at time t and at complete saturation. It was found in his works that the diffusion of moisture happens in the smallest dimension which is usually the thickness. Therefore, Equation 6.3 can be reduced to Equation 6.4.

$$\frac{C(t)}{C_\infty} = 1 - \frac{8}{\pi^2} \sum_{k=1}^{\infty} \frac{\exp(-\pi^2 t (D_z (\frac{(2k+1)^2}{h})))}{(2k+1)^2} \quad (6.4)$$

A solution for Equation 6.4 can be graphically represented in Figure 6.1 [curve Linear Fickian (LF)]. Curve A represents the case where the specimen never attains an equilibrium value which can be represented using the Langmuir model. Curve B represents a dual Fickian diffusion. Curve C can be fitted to a polymeric material which is induced to damage or with high void content. Curve D represents the characteristics of materials

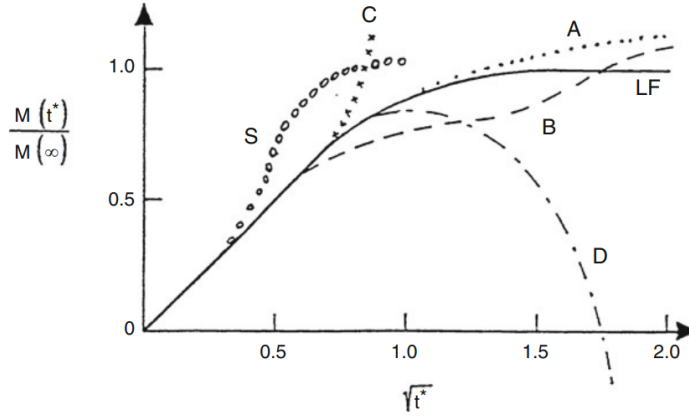


Figure 6.1: Typical diffusion behaviours of non fickian weight gain absorption [213]

exhibiting both absorption and desorption, which is caused by leaching or hydrolysis of polymeric chains in composites [213].

In order to identify the diffusion parameters, one should determine the unknowns in equation 6.4. C_∞ can be considered as C_{max} and D_x can be obtained by least square method by following the evolution of $C(t)$ obtained by experimental measurement [214]. This holds true in case of both pure polymers and reinforced polymers. The moisture content in the surrounding also affects the diffusion coefficient and maximum uptake by the material [199, 215] especially in case of natural fiber composites as natural fibers act as absorbents [111, 201, 205, 216].

Along with hygrothermal aging of composites, the influence of operating temperature on the performance of composites should also be investigated. In the case of thermoplastic composites, this dependency on temperature stands out as the matrix becomes rubbery and can no further carry the loads. Several investigations on this subject were carried out for glass fiber, and carbon fiber reinforced composites in terms of flexural, tensile and impact tests [197, 199, 217, 218]. For these composites, the main factor of influence was the matrix. An increase in the operating temperature greater than the T_g of matrix leads to a loss in stiffness of the material and its mechanical performance. On the other hand, natural fiber composites, are not just limited by the matrix properties but also by the thermal properties of the reinforcement. Natural fibers like flax fibers start to degrade around 220°C, except for basalt fibers whose degradation temperature is similar to that of glass fibers [219]. This issue calls for possible solutions which can circumvent this low degradation temperature. One option is to coat the fibers with a flame retardant coating like Ammonium PolyPhosphate (APP), which shifts the degradation temperature from 220 °C to 250°C [220, 221]. A study by Rajaei et al. [222] added APP to epoxy instead of fibers, to investigate its influence on the high-temperature performance of the

composite. They stated that the thermal degradation onset was lower for composites with APP compared to composites without APP, which resulted in lower flexural performance. Studies by Tejvedi et al. [223] and Dhakal et al. [217] showed that if the T_g of the matrix is low, the composites start to lose their mechanical properties with increase in operating temperature. There are a handful of studies which made a comparison for different reinforcement types, additives to the matrix and hybridization of composites, but, a study on biosourced thermoset composites at different operating temperatures was scarcely addressed in the literature. Thus, as a part of this study, an investigation on mechanical performance of flax fiber composites under extreme conditions will be carried out. Moreover, a comparison will be made on two sets of flax fiber composites, one based on conventional epoxy system and another, based on bio-sourced benzaoxazine resin.

6.3 Manufacturing of composite specimens

Composite specimens were manufactured with a 2x2 twill weave flax fabric (Flipts & Dobbels) with an areal weight of 260 g/m². A commercial epoxy, PRIME-27(Gurit®) and, the benzoxazine resin which was developed within the project BIOCOMPAL are used as matrix. Composite plates are manufactured using hand-layup followed by compression molding. The manufacturing cycle is presented in Figure 6.2. In the case of benzoxazine based composites, the composites are manufactured following a slightly different procedure. First, the fabrics are dried in an oven at 70°C overnight, and then the resin is evenly distributed on these fabrics to obtain preregs. This step is carried out because the benzoxazine resin is quite reactive at a prescribed processing temperature (150°C). During melting and cross-linking, the resin produces gases which led to the high residual porosity. Hence, a degassing step is adopted to avoid high void content. Later, the preregs are transferred onto a preheated press (150°C) and are subjected to consolidation for 4 hours under 5 bar pressure. A post-curing step is carried out in an oven at 180°C for 2 hours to complete the curing cycle. Two plates are manufactured for each composite to obtain 25 rectangular specimens of size 75x25x2mm³ for aging tests.

6.4 Hygrothermal aging

In order to understand the effect of temperature and humidity content on composites with different matrix systems, the composites are subjected to hygrothermal aging in a conditioning chamber (see Figure 6.3) at 50°C with a relative humidity of 90% for a period of 40 days (see Figure 6.4). The temperature and humidity are maintained constant with an error of 1%. The composite specimens are monitored systematically until a saturation

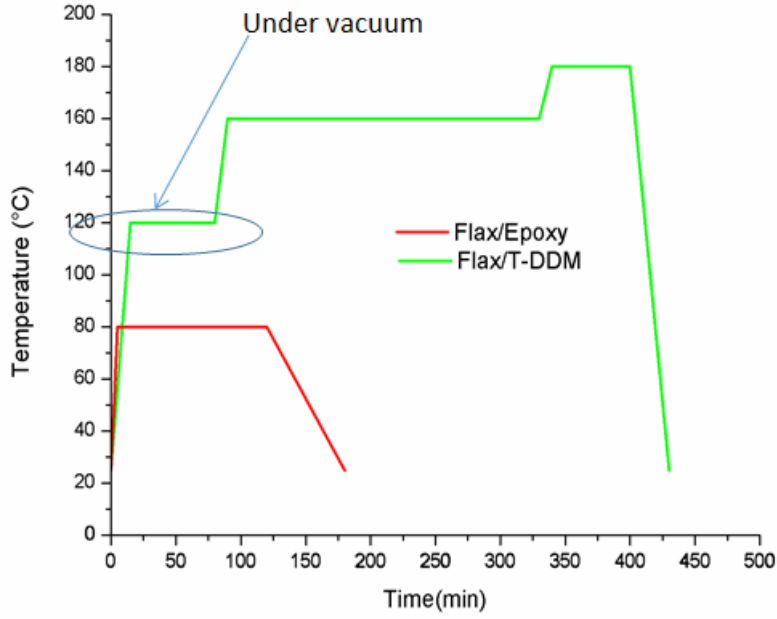


Figure 6.2: Manufacturing cycle for two composites: flax/epoxy and flax/benzaoxazine

plateau is observed. At each time interval, five samples of pure resin and composite are taken from the aging chamber to measure the change in thickness and mass. Thickness is measured using vernier calipers, whereas the mass of the specimens is measured with an electronic balance with an accuracy of $10^{-4}g$. Once the composites and resin specimens reached a saturation point, they are placed in a desiccator at room temperature to study the desorption behavior. This is repeated until a 40 days period is completed.

The mass gain (%) was calculated as follows:

$$M(\%) = \frac{M(t) - M_i}{M_i} \times 100 \quad (6.5)$$

where $M(t)$ is the mass at time t , M_i is the initial mass of the specimen. Absorption ratio of water into a composite specimen can be characterized into two zones. The first is a linear region which is followed by a plateau (see Figure 6.1, Curve LF). Shen et al. [214] proposed that during the initial part of the curve (i.e., $M/M^\infty < 0.6$, the diffusion coefficient can be determined using the following equation:

$$\frac{M - M_i}{M^\infty - M_i} = \frac{4}{h} \sqrt{\left(\frac{Dt}{\pi}\right)} \quad (6.6)$$

where h is the thickness of the specimen, M^∞ is the saturated mass of the specimen and D is the diffusion coefficient. This equation is a simplified form of Equation 6.4. The second half of the curve can be represented by the following approximation:

$$\frac{M - M_i}{M^\infty - M_i} = 1 - \exp\left[-7.3\left(\frac{Dt}{h^2}\right)^{0.75}\right] \quad (6.7)$$



Figure 6.3: Aging chamber

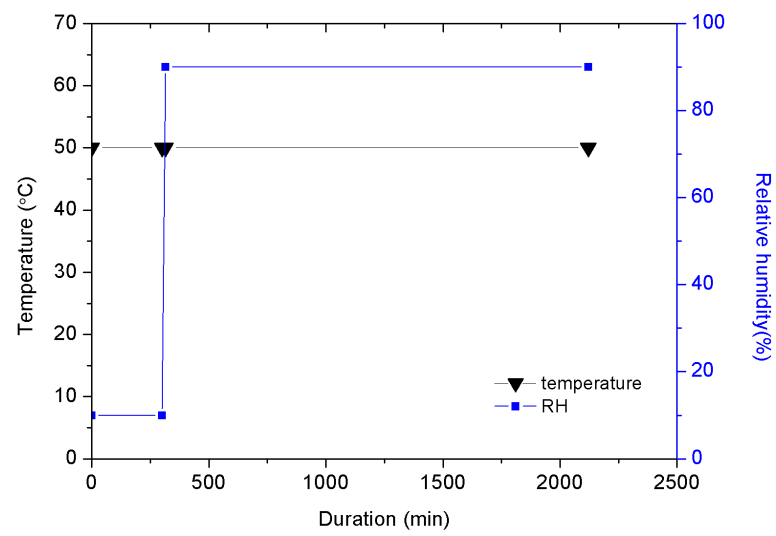


Figure 6.4: Imposed hygrothermal cycle on composite coupons

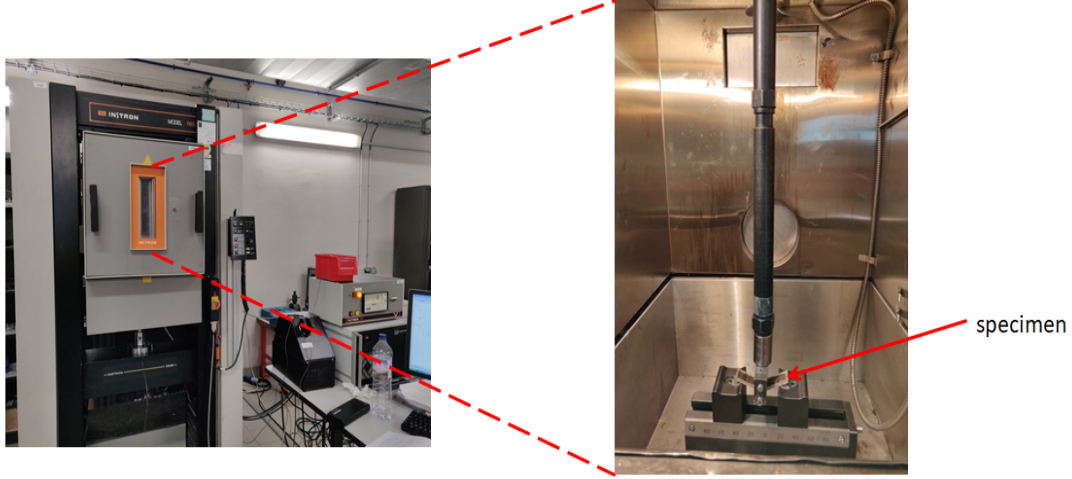


Figure 6.5: Experimental set up for high temperature tests

6.5 Mechanical tests

Flexural tests are conducted on specimens subjected to hygrothermal aging. Three-point bending tests are performed with a universal testing machine, Instron 1185. For these tests, the standard followed is ISO 14125 [224]. The specimens were of size 75mm in length and 25mm in width. The crosshead speed is 5mm/min and the load cell used is 1kN. In the case of elevated temperature tests, along with three-point bending tests, short beam shear (SBS) tests are selected to emphasize more on the matrix properties [225]. Elevated temperature tests are conducted using a heating chamber. All the specimens are heated in the chamber for at least 10-12 minutes so that the samples reach the same temperature (see Figure 6.5). This time is selected by monitoring the specimen temperature with a thermocouple. Three testing temperatures, i.e., 23°C, 60 °C and 120°C, are selected so that one of them is closer to the T_g of epoxy (72°C) and another higher than the normal service temperature of an exterior automobile part. Similar testing conditions are maintained for flexural tests and SBS tests; the cross-head speed of 1mm/min. The inter laminar shear strength (ILSS) is calculated using Equation 6.8

$$ILSS = \frac{3P_{max}}{4bh} \quad (6.8)$$

where P_{max} is the maximum load, b is the width of the sample and h is the thickness of the sample. At least, six specimens are tested for each condition to report an average value of flexural properties and for SBS tests, at least eight samples are tested to report the average values.

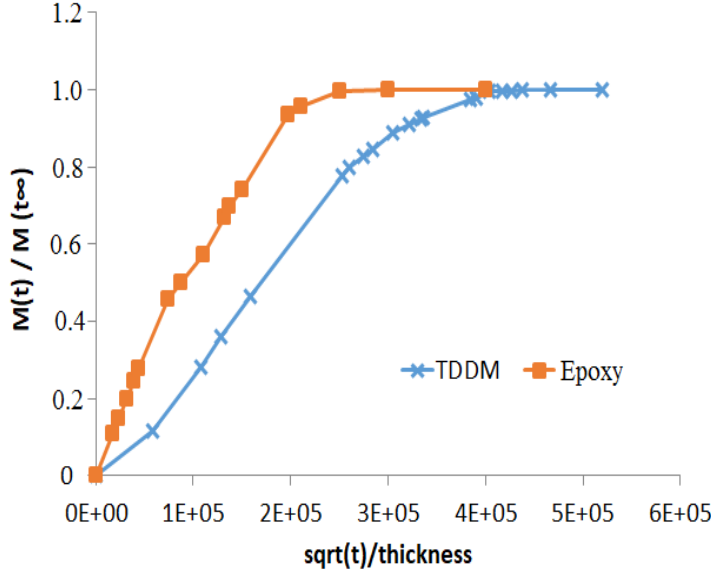


Figure 6.6: Moisture uptake for epoxy and benzaoxazine resin blocks

6.6 Water absorption of pure resin samples

In order to first understand the differences between epoxy and benzoxazine resins, pure resin blocks and composites specimens were aged. The resin blocks are around 3.8 mm thick for epoxy resin and 3mm thick for benzoxazine resin. Unfortunately, during the curing process of benzoxazine resin, air bubbles were trapped, leading to a residual porosity of 8-9%. Despite curing them in a vacuum chamber, these air bubbles were difficult to remove without external pressure. Due to this residual porosity, the moisture absorption is greater in the case of benzaoxazine resin than the values reported in the literature [226, 227]. The epoxy resin absorbed a maximum of 1.85% moisture content, compared to 2.77% for the benzoxazine resin. When the diffusion coefficients for both resin systems are compared, the benzoxazine resin has a diffusivity a very less of $3.83E - 13m^2/s$, while the epoxy has a value of $1.51E - 12m^2/s$. This difference even after trapping air bubbles shows that the benzoxazine resin may exhibit better hydrophobic properties than the commercial epoxy. Figure 6.6 shows the evolution of the moisture absorption over time for the two resins, where the difference in the absorption can be noticed. In Figure 6.7, the average normalized thickness of the epoxy blocks increase rapidly and reaches a plateau value after 0.6% of the M_∞ . The smoothness of the curve can be argued. Nevertheless, given the measurement method, these results seem to be valid. In order to obtain a further smooth curve, a micrometer should be utilized as suggested in [228]. The similar trend is observed for benzoxazine samples, and its thickness evolution is incoherent with the evolution of moisture uptake.

Concerning the moisture absorption of the composite samples, the flax/epoxy com-

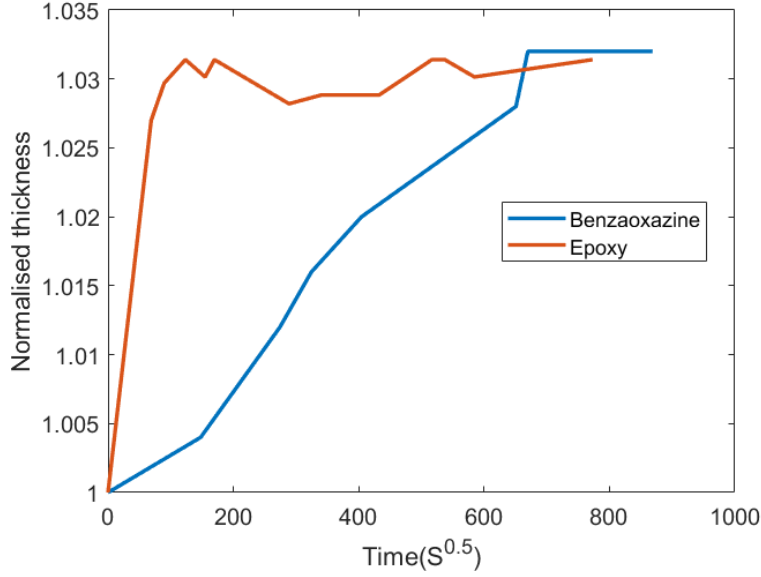


Figure 6.7: Evolution of thickness of resin blocks with time

posites had a moisture content greater than 7% moisture, and the flax/benzoxazine had a moisture content greater than 6% moisture (see Figure 6.8). The saturation value for flax/epoxy composites is found to be coherent with the values reported in the literature [2, 84, 205]. Similar to pure resin specimens, the flax/epoxy composite had a higher diffusion coefficient ($3E - 10m^2/s$) than the flax/benzoxazine composites, ($2.2E - 11m^2/s$). Similar to pure resins blocks, composite samples had residual porosities which influenced the maximum saturation plateau. For flax/epoxy composites, the residual porosity is 3.5%, and for flax/benzoxazine composites, the porosity content is higher around 7.5%. It is speculated that due to this high porosity content when the moisture content is plotted against time in Figure 6.8, the initial uptake behavior remains the same, but an evident difference in the saturation points can be observed. This tendency can also be linked to open edges of the specimen. If the specimen's edges are not sealed, the moisture can be absorbed through those open edges, as fibers are exposed to humidity [229]. Moreover, in our case, given that the fibers are hydrophilic, the similar behavior in moisture uptake can be explained. Also, it is also assumed that the penetration of the resin into cell walls also affects the maximum moisture content and diffusion rate. Therefore, it can be deduced from the results that, even with a higher void content, the flax/benzoxazine composites had a slower diffusion than the flax/epoxy. This could be due to the excellent fiber-matrix interface or the hydrophobicity of benzoxazine, or both.

In addition to moisture absorption measurements, composite samples are also tested to evaluate the evolution of their mechanical properties with hygrothermal aging. At each time interval, ten samples are taken out of the climatic chamber, of which five samples

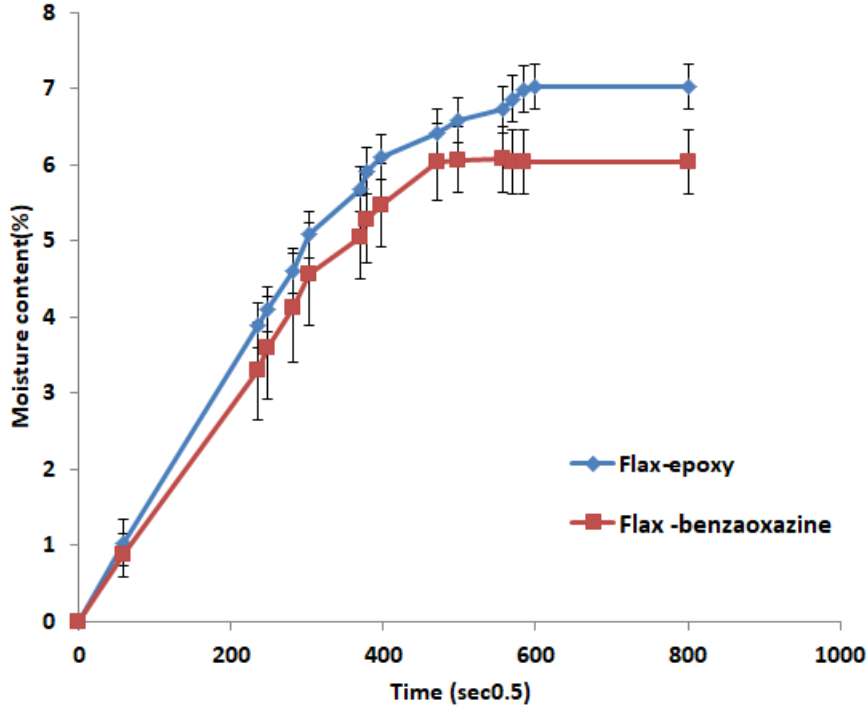


Figure 6.8: Moisture absorption of composite specimens

are placed in a drying chamber to remove all the moisture, and the others are tested immediately. This is done to investigate the influence of the duration of aging and the reversibility of aging effects on a composite sample. Figures 6.9 and 6.10 show that samples with moisture designated "wet" always exhibit lower mechanical performance than dried samples denoted as "Dried". The flexural modulus and strength of composites of "wet" specimens drop to 60% and 68%, respectively, of their original values after three consecutive days of aging and later attain a certain plateau at 64% and 72% for modulus and strength respectively.

On the other hand, when the composite specimens from the same batch are dried in a desiccator until they lose all the moisture, the composites regain a part of their lost mechanical properties. Almost complete recovery of mechanical properties is only observed for composites aged for three days. These composites have retained 92% of their original modulus and 98% of their strength. After three days, the flexural strength of the composites decreased continuously, whereas the flexural modulus had attained a pseudo-plateau (as a slight decrease is observed after 40 days of aging). These differences in "wet" and "dry" composites can be attributed to the damage mechanisms during hygrothermal aging of natural fiber composites. In Figure 6.11, a clear depiction of the deterioration of the fiber-matrix interface during the hygrothermal aging is presented. The loss of flexural properties can be explained using this figure. Due to the fiber swelling after water absorption, the internal stresses around the interface increases, leading to early

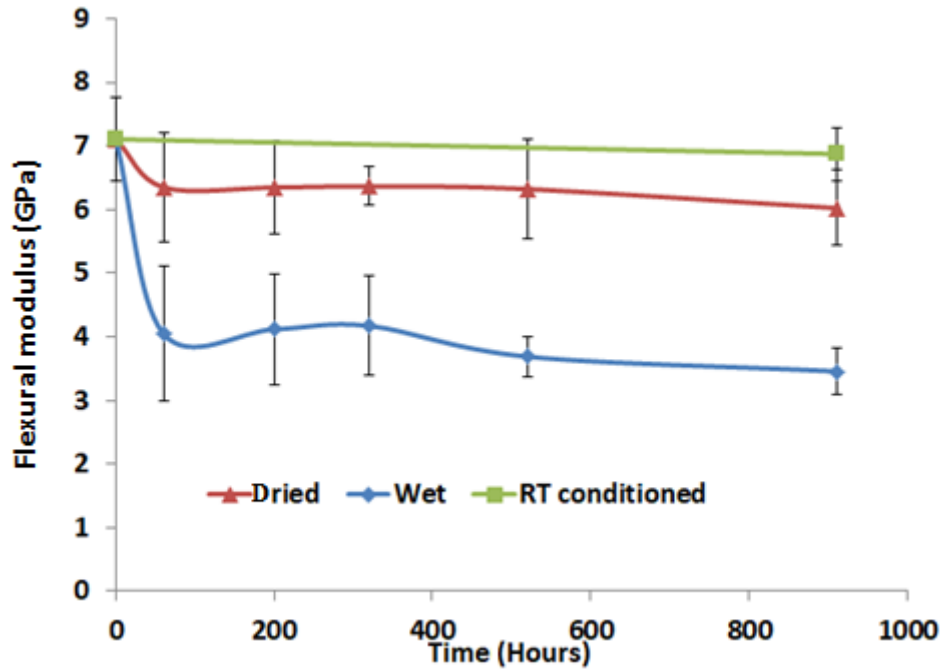


Figure 6.9: Evolution of flexural modulus of flax/epoxy composites during aging

initiation of damage. However, when the composite is dried, the removal of moisture decreases the internal stresses and returns to the original form.

Nevertheless, this reversal is not always complete because there is hysteresis during this phenomenon. Also, this hysteresis can be explained by the difference in hygroscopic swelling of the fibers, which is much larger than the expansion of the matrix. Thus, when the composites are dried and the fibers regain their initial diameter before water absorption, the interface between the matrix and the fibers is weakened, resulting in a poor stress transfer from matrix to the fibers leading to a continual decrease in strength of "dry" composites. Similar results were reported by Regazzi et al.[101] in the case of flax/PLA composites subjected to hygrothermal aging.

In the case of flax/benzoxazine composites, the evolution of flexural properties with a duration of hygrothermal aging is similar to that of the flax/epoxy composites (see Figure 6.12). The tests are carried out only for 30 days due to the machine issue. The only difference that stands out is the reversibility of the properties. With the duration of aging, the flexural strength of the composites decreases to a maximum of 78% of its original strength, and the flexural modulus decreased to a maximum of 85% of its original value. These results indicate two interesting features of the benzoxazine resin. Even when the composite absorbs water, the major contributors to this water uptake are flax fibers. The water diffusion does not plasticize the benzoxazine resin at 50°C. Secondly, due to an excellent interface between the flax fibers and matrix, there is a less chance of interfacial debonding (see Figure 6.13). Nevertheless, the influence of

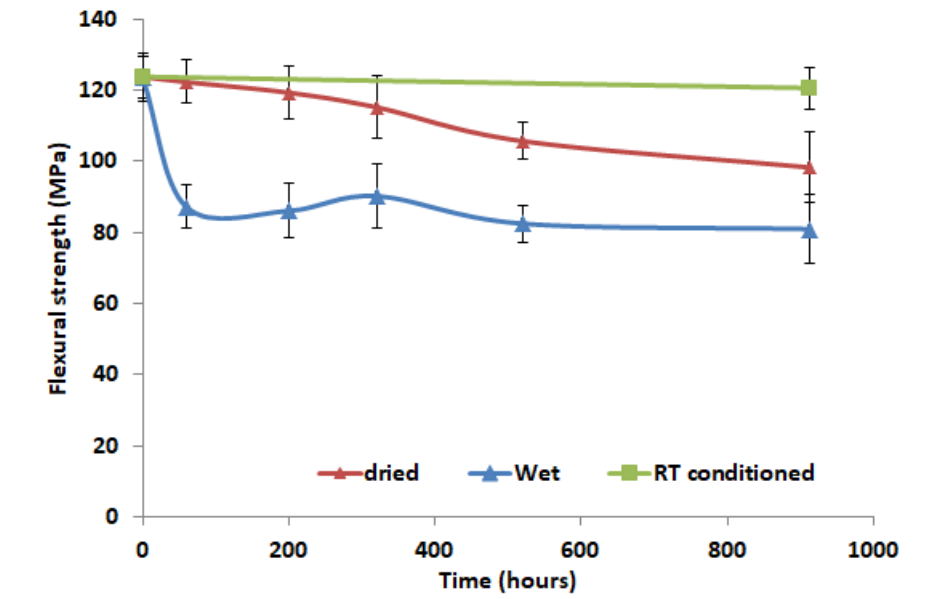


Figure 6.10: Evolution of flexural strength of flax/epoxy composites during aging

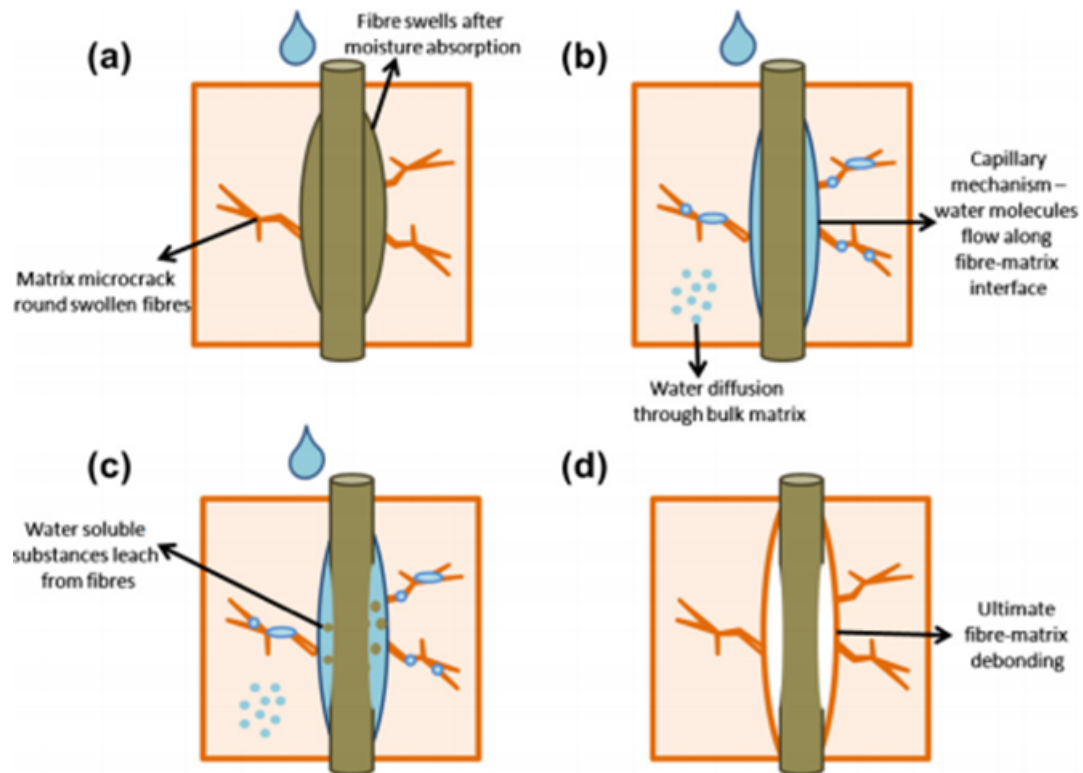


Figure 6.11: Schematic of effects of water absorption on natural fiber-matrix interface [230]

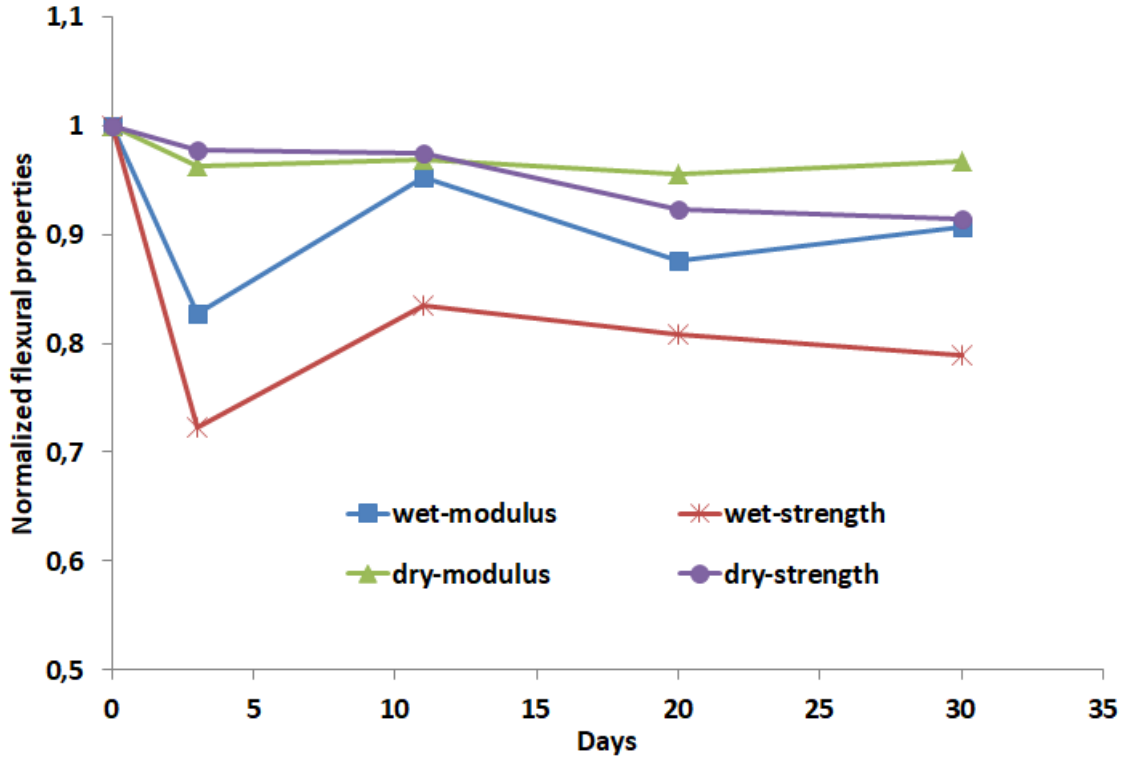


Figure 6.12: Normalized flexural properties of flax/benzoxazine composites during aging

swelling induced stress can be seen in Figure 6.12, where after 30 days of aging, the strength of the composite decreased by 10% of its original strength. Despite this decrease, flax/benzoxazine composites outperform flax/epoxy composites, proving them as an ideal candidate for applications where the effect of humidity and temperature is great. In addition, these tests are dominated by the matrix and fiber-matrix interface. Therefore, the influence from the fibers cannot be seen directly.

6.7 Influence of operating temperature

In this part of the study, we investigate the influence of operating temperature on the flexural and inter-laminar shear strength of the composites. Similar to the study in the previous section, a comparison is made between flax/epoxy and flax/benzoxazine composites. In the case of flax/epoxy composites, at 23°C, the composites exhibit a pseudo-ductile behavior with a clear breaking point (see Figure 6.14). When the temperature of the chamber reaches 60°C, the composites exhibit purely ductile behavior with large deformation. This is because as the operating temperature approaches the T_g range of the material, the operating temperature causes the composite to become rubbery, thus exhibiting ductility. When the operating temperature reaches 120°C, the specimen starts to deform under a constant load similar to that of creeping. This proves that these

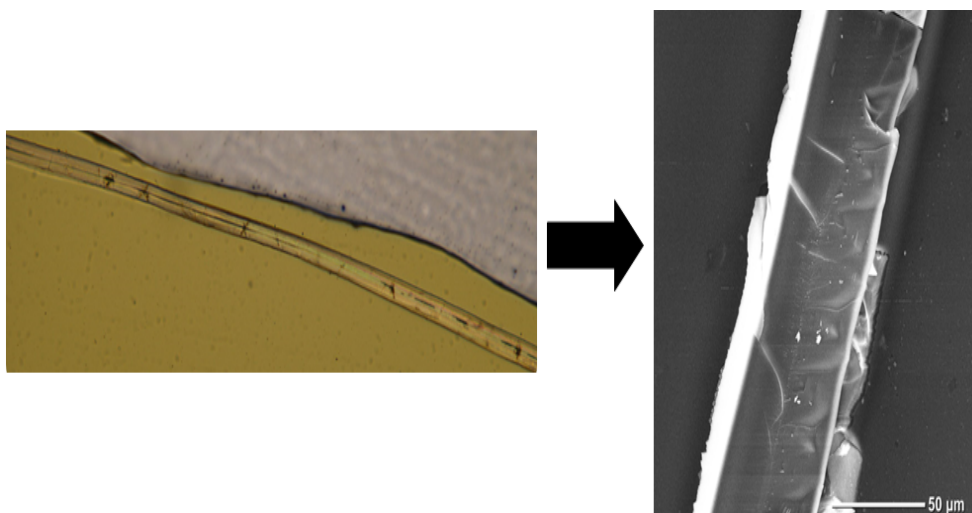


Figure 6.13: Micrographs of flax/benzaoxazine (left) single fiber cured in a pool of benzaoxazine resin; (right) SEM image of fiber surface indicating the presence of resin residue after shearing from resin.

flax/epoxy composites are not suitable for temperatures over 50°C. When similar temperatures are imposed on flax/benzoxazine composites, their mechanical behavior does not change with change in temperature (see Figure 6.15). The force-displacement curves at all three temperatures are similar to the flax/epoxy composites at 23°C. This can easily be explained by pointing out that the T_g of these composites is around 158°C. This also means that the composite properties should remain unaltered at these temperatures. In Figure 6.16, the flexural strengths of both composites are plotted against different operating temperatures. The flax/benzoxazine composites maintain their properties until 60°C. At 120°C however, there is a slight drop in their strength. In reality, this is an anomaly as there should be no decrease in the strengths as the operating temperature is well within the limits of T_g of the composite. The only reason that can explain this decrease is the high local porosity content, which accounted for 6.2% instead of the previously reported value of 5.5%.

Similarly, in the case of SBS tests, the determination of ILSS of flax epoxy composites above 23°C is challenging because the samples show no failure point. Even if there is one, it is caused by slippage of the sample between the supports which cannot be considered when calculating the ILSS. Therefore, these values are not reported. Nevertheless, the ILSS of flax/benzoxazine composites, show consistent results with a change in operating temperature, as shown in Table 6.1. The temperature has very less influence on the ILSS of flax/benzaoxazine composites. This could be due to the excellent fiber-matrix bonding between flax and benzaoxazine resin as shown in Figure 6.13.

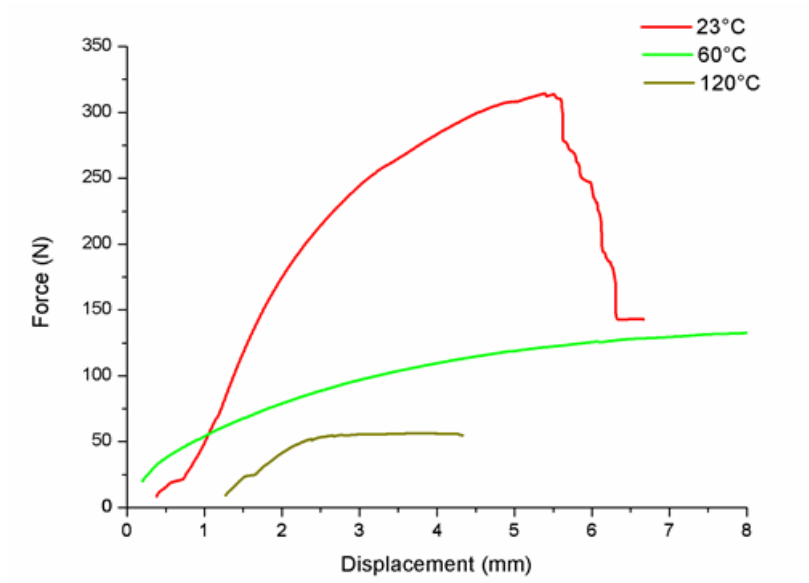


Figure 6.14: Force displacement curves of flax/epoxy composites at different temperatures

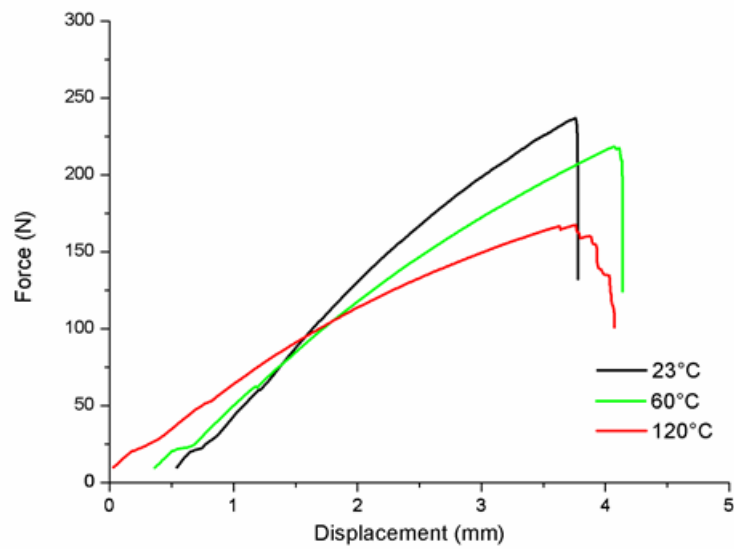


Figure 6.15: Force-displacement curves of flax/benzaoxazine composites at different temperatures

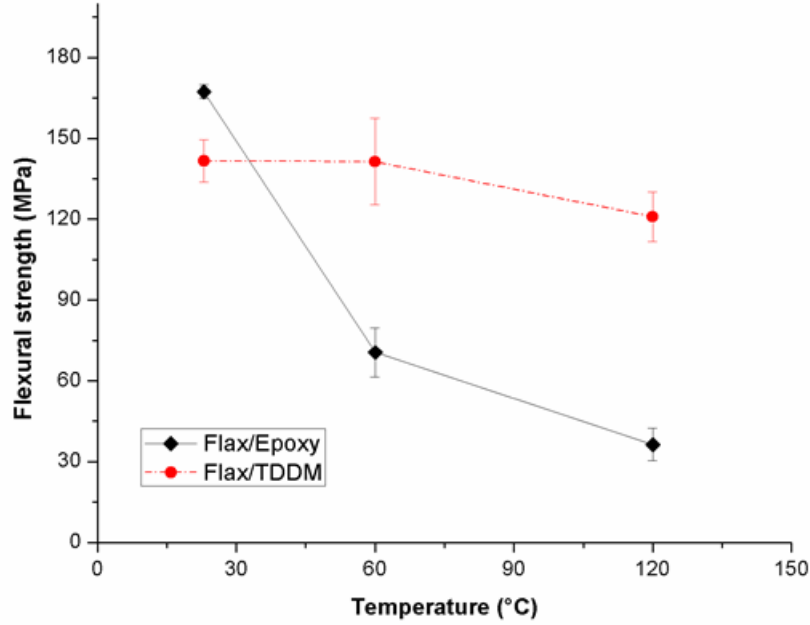


Figure 6.16: Flexural strength of composites at different operating temperatures

Temperature (°C)	Flax/Epoxy	Flax/Benzoxazine
23	15.1 ± 2.5	19.2 ± 2.5
60	NA	18.7 ± 1.85
120	NA	17.6 ± 3.2

Table 6.1: Inter laminar shear strengths of composites at different operating temperatures

6.8 Conclusions

In this study, the investigation on the hygrothermal aging and influence of operating temperature of flax fiber-reinforced composites were presented. Hygrothermal aging was carried out on flax composites with two different resin systems; epoxy and benzoxazine. It was observed that due to the hydrophobic nature of benzoxazine resin, their corresponding composites had diffusion coefficients lower than flax epoxy composites. Even in terms of mechanical properties, flax/benzoxazine composites outperformed flax/epoxy composites. In fact, when these composites were dried and tested, they retained about 90% of their initial properties. When the same composites were exposed to high operating temperatures, above 60°C, flax/epoxy composites started to lose their mechanical properties. Conversely, even at 150°C, flax/benzoxazine composites exhibit excellent mechanical properties. These two studies indicate the advantages of bio-based benzoxazine resin. In order to thoroughly understand the mechanical properties of flax/benzoxazine composites, fatigue and creep tests also should be conducted.

Chapter 7

Conclusions and Perspectives

Conclusion

This dissertation analyzed the influence of manufacturing parameters on the mechanical properties of the composites. The study addressed these issues from the point of view of liquid composite molding.

An investigation about the influence of processing conditions on flax fiber thermoset composites was presented. It was pointed out that the mechanical properties of the flax fiber composites were highly dependent on the resin cure cycle. At high curing temperatures, due to the phenomenon of resin penetration into fibers, it was found that the tensile properties of the UD composites were improved significantly. Also, this work points out the importance of considering the resin penetration phenomenon on the estimation of flax fiber tensile properties using the IGBT method.

The wettability of flax fibers was investigated based on wicking tests. A mathematical model was developed as a part of this work, which took into account both the fiber swell and liquid absorption. A statistical approach was employed to estimate the hydraulic radius of the fiber bundle. The model was then compared to the experimental results, which showed a good fit. Also, wicking tests with water showed that the maximum swell ratio of fibers in free space and fibers inside the mold is not the same due to the limited space caused by fiber-fiber interaction.

The study of variation of fiber diameter on tow permeability showed that the classic tow permeability models could not be adopted to estimate the permeability of flax fiber tows. Furthermore, the numerical simulations pointed out the difference in permeability values of RVEs with constant and variable diameters. Then, the void content prediction in flax fiber preforms was presented. An effort was made to compare the model prediction with experimental results. Although the model is limited, it does provide an idea of void formation and compaction in flax fiber preforms.

Finally, an investigation on the flax fiber composites in an hot and humid environment is presented in Chapter 6. A comparison was made between benzoxazine and epoxy composites which pointed out the advantages of benzoxazine composites in an extreme environment. The resistance to both hygrothermal aging and high temperatures makes flax/benzoxazine composites suitable for high-performance applications.

Perspectives

In order to understand the resin penetration depth into the flax fibers based on the curing temperature, nano-indentation tests can be carried out near the fiber-matrix interface. Also, it may be interesting to conduct similar tests on flax fibers subjected to different chemical treatments because the interaction of flax fibers with the resin is dependent on the fiber surface treatment.

Furthermore, to extend the work in the chapter of tow permeability, it would be interesting to generate several hundred micro structures exhibiting a gradient of packing fractions, to represent the real scenario. Longitudinal and transverse flow simulations, preferably saturated flow simulations, then can be carried out on those RVEs to understand the influence of local variations of fiber volume fractions. This large set of simulations will serve as a data-driven model instead of being dependent on an analytical model that may or may not predict the exact value. For natural fibers, the longitudinal permeability of the generated RVEs should be estimated based on the generated RVEs. The irregularity of fiber length should be considered while estimating the transverse permeability of the RVE. This may increase the size of the computational domain massively, but given the current computational means, this should not be an issue. Further tests should be conducted using specialized test benches to understand the void formation mechanisms in flax fiber preforms. Given that the rate of tow saturation is not the same as the synthetic fiber tows like glass or carbon, it would be interesting to experimentally investigate the tow saturation by using dielectric sensors or advanced in-situ tests using X-ray tomography.

In the case of hygrothermal aging of flax thermoset composites, it would be interesting to test these composites under fatigue or multiple load-unload cycles to study their evolution of damage in the material at different stages of aging. This would give an in-depth understanding of the feasibility of the application of the flax/benzoxazine composites.

Bibliography

- [1] M. Bodaghi, C. Cristóvão, R. Gomes, and N. C. Correia. Experimental characterization of voids in high fibre volume fraction composites processed by high injection pressure RTM. *Composites Part A: Applied Science and Manufacturing*, 82:88–99, mar 2016.
- [2] Van Hau Nguyen, Mylène Deléglise-Lagardère, and Chung Hae Park. Modeling of resin flow in natural fiber reinforcement for liquid composite molding processes. *Composites Science and Technology*, 113:38–45, 2015.
- [3] Gaston Francucci, Abdul Moudood, Mainul Islam, Anisur Rahman, and Andreas Öchsner. Flax fiber and its composites: An overview of water and moisture absorption impact on their performance. *Journal of Reinforced Plastics and Composites*, page 073168441881889, dec 2018.
- [4] John Summerscales, Nilmini P.J. Dissanayake, Amandeep S. Virk, and Wayne Hall. A review of bast fibres and their composites. Part 1 – Fibres as reinforcements. *Composites Part A: Applied Science and Manufacturing*, 41(10):1329–1335, oct 2010.
- [5] Caroline Baillie. *Green Composites*. CRC Press, mar 2005.
- [6] Libo Yan, Nawawi Chouw, and Krishnan Jayaraman. Lateral crushing of empty and polyurethane-foam filled natural flax fabric reinforced epoxy composite tubes. *Composites Part B: Engineering*, 63:15–26, 2014.
- [7] The Barometer of european flax/linen 2015. Technical report.
- [8] Claudine Morvan, Christine Andème-Onzighi, Raynald Girault, David S. Himmelsbach, Azeddine Driouich, and Danny E. Akin. Building flax fibres: more than one brick in the walls. *Plant Physiology and Biochemistry*, 41(11):935–944, 2003.
- [9] Nicolas Martin, Peter Davies, and Christophe Baley. Comparison of the properties of scutched flax and flax tow for composite material reinforcement. *Industrial Crops & Products*, 61:284–292, 2014.

- [10] K. Charlet, C. Baley, C. Morvan, J.P. P Jernot, M. Gomina, and J. Bréard. Characteristics of Herm{è}s flax fibres as a function of their location in the stem and properties of the derived unidirectional composites. *Composites Part A: Applied Science and Manufacturing*, 38(8):1912–1921, 2007.
- [11] A. Bourmaud, G. Ausias, G. Lebrun, M.-L. Tachon, and C. Baley. Observation of the structure of a composite polypropylene/flax and damage mechanisms under stress. *Industrial Crops and Products*, 43:225–236, may 2013.
- [12] Antoine Le Duigou, Peter Davies, and Christophe Baley. Environmental Impact Analysis of the Production of Flax Fibres to be Used as Composite Material Reinforcement. *Journal of Biobased Materials and Bioenergy*, 5(1):153–165, mar 2011.
- [13] T. Gurunathan, Smita Mohanty, and Sanjay K. Nayak. A review of the recent developments in biocomposites based on natural fibres and their application perspectives. *Composites Part A: Applied Science and Manufacturing*, 77:1–25, 2015.
- [14] C. Baley. Analysis of the flax fibres tensile behaviour and analysis of the tensile stiffness increase. *Composites - Part A: Applied Science and Manufacturing*, 33(7):939–948, 2002.
- [15] Anaële Lefeuvre, Alain Bourmaud, and Christophe Baley. Optimization of the mechanical performance of UD flax/epoxy composites by selection of fibres along the stem. *Composites Part A: Applied Science and Manufacturing*, 77:204–208, oct 2015.
- [16] M. Truong, W. Zhong, S. Boyko, and M. Alcock. A comparative study on natural fibre density measurement. *Journal of the Textile Institute*, 100(6):525–529, aug 2009.
- [17] Noa Brezinka, Zach Triplett, Mercedes Alcock, Ali Amiri, Chad A. Ulven, and Augusto Moreira. Standard density measurement method development for flax fiber. *Industrial Crops and Products*, 96:196–202, 2016.
- [18] F Ilczyszyn, A Cherouat, and G Montay. Effect of the fibre morphology on the mechanical properties of hemp fibres: Digital imaging treatments coupled to 3D computational analysis. In *ECCM-15, European Conference on Composite Materials*, Venice, 2012.
- [19] John Summerscales. Fibre Area Correction Factors (Facf) For The Extended Rules-Of-Mixtures For Natural Fibre Reinforced Composites. In *International Conference on Natural fibers (ICNF-4)*, Porto, 2019.

- [20] Vincent Placet, Frédérique Trivaudey, Ousseynou Cisse, Violaine Gucheret-Retel, and M Lamine Boubakar. Diameter dependence of the apparent tensile modulus of hemp fibres: A morphological, structural or ultrastructural effect? *Composites Part A: Applied Science and Manufacturing*, 43(2):275–287, 2012.
- [21] Guillaume Coroller, Anaële Lefeuvre, Antoine Le Duigou, Alain Bourmaud, Gilles Ausias, Thierry Gaudry, and Christophe Baley. Effect of flax fibres individualisation on tensile failure of flax/epoxy unidirectional composite. *Composites Part A: Applied Science and Manufacturing*, 51:62–70, 2013.
- [22] K. Charlet, J.P. Jernot, M. Gomina, J. Bréard, C. Morvan, and C. Baley. Influence of an Agatha flax fibre location in a stem on its mechanical, chemical and morphological properties. *Composites Science and Technology*, 69(9):1399–1403, 2009.
- [23] Katharina Haag, Justine Padovani, Sergio Fita, Jean-Paul Trouvé, Christophe Pineau, Simon Hawkins, Hein De Jong, Michael K. Deyholos, Brigitte Chabbert, Jörg Müssig, and Johnny Beaugrand. Influence of flax fibre variety and year-to-year variability on composite properties. *Industrial Crops and Products*, 98:1–9, apr 2017.
- [24] NF T25-501-3 - Mars 2015 and NF T25-501-2. Fibres de renfort - Fibres de lin pour composites plastiques - Partie 2 : détermination des propriétés en traction des fibres élémentaires. *AFNOR standards*, 2015.
- [25] Bo Madsen, Mustafa Aslan, and Hans Lilholt. Fractographic observations of the microstructural characteristics of flax fibre composites. *Composites Science and Technology*, 123:151–162, feb 2016.
- [26] Xin Ning and Hatsuo Ishida. Phenolic materials via ring-opening polymerization: Synthesis and characterization of bisphenol-A based benzoxazines and their polymers. *Journal of Polymer Science Part A: Polymer Chemistry*, 32(6):1121–1129, apr 1994.
- [27] Andrey Chernykh, Tarek Agag, and Hatsuo Ishida. Effect of polymerizing diacetylene groups on the lowering of polymerization temperature of benzoxazine groups in the highly thermally stable, main-chain-type polybenzoxazines. *Macromolecules*, 42(14):5121–5127, jul 2009.
- [28] N. N. Ghosh, B. Kiskan, and Y. Yagci. Polybenzoxazines-New high performance thermosetting resins: Synthesis and properties. *Progress in Polymer Science*, 32(11):1344–1391, nov 2007.

- [29] David M. Pereira, Patrícia Valentão, José A. Pereira, and Paula B. Andrade. Phenolics: From chemistry to biology. *Molecules*, 14(6):2202–2211, jun 2009.
- [30] Cédric Pupin, Annie Ross, Charles Dubois, Jean-Christophe Rietsch, Nicolas Vernet, and Edu Ruiz. Formation and suppression of volatile-induced porosities in an RTM epoxy resin. *Composites Part A: Applied Science and Manufacturing*, 94:146–157, mar 2017.
- [31] Cédric Pupin, Annie Ross, Charles Dubois, Jean Christophe Rietsch, and Edu Ruiz. Predicting porosity formation in phenolic resins for RTM manufacturing: The porosity map. *Composites Part A: Applied Science and Manufacturing*, 100:294–304, sep 2017.
- [32] M. Anders, J. Lo, T. Centea, and S. R. Nutt. Eliminating volatile-induced surface porosity during resin transfer molding of a benzoxazine/epoxy blend. *Composites Part A: Applied Science and Manufacturing*, 84:442–454, may 2016.
- [33] Henry Darcy. Les fontaines publiques de la vile de Dijon. Paris: Dalmont. 1856.
- [34] R. Arbter, J. M. Beraud, C. Binetruy, L. Bizet, J. Bréard, S. Comas-Cardona, C. Demaria, A. Endruweit, P. Ermanni, F. Gommer, S. Hasanovic, P. Henrat, F. Klunker, B. Laine, S. Lavanchy, S. V. Lomov, A. Long, V. Michaud, G. Morren, E. Ruiz, H. Sol, F. Trochu, B. Verleye, M. Wietgreffe, W. Wu, and G. Ziegmann. Experimental determination of the permeability of textiles: A benchmark exercise. *Composites Part A: Applied Science and Manufacturing*, 42(9):1157–1168, 2011.
- [35] N Vernet and F Trochu. In-plane and through-thickness permeability models for three-dimensional Interlock fabrics. *Journal of Composite Materials*, 50(14):1951–1969, jun 2016.
- [36] Chung-Hae Park and Woo Il Lee. Modeling void formation and unsaturated flow in liquid composite molding processes: a survey and review. *Journal of Reinforced Plastics and Composites*, 30(11):957–977, jun 2011.
- [37] N. Vernet, E. Ruiz, S. Advani, J.B. Alms, M. Aubert, M. Barburski, B. Barari, J.M. Beraud, D.C. Berg, N. Correia, M. Danzi, T. Delavière, M. Dickert, C. Di Fratta, A. Endruweit, P. Ermanni, G. Francucci, J.A. Garcia, A. George, C. Hahn, F. Klunker, S.V. Lomov, A. Long, B. Louis, J. Maldonado, R. Meier, V. Michaud, H. Perrin, K. Pillai, E. Rodriguez, F. Trochu, S. Verheyden, M. Wietgreffe, W. Xiong, S. Zaremba, and G. Ziegmann. Experimental determination of the permeability of engineering textiles: Benchmark II. *Composites Part A: Applied Science and Manufacturing*, 61:172–184, 2014.

- [38] Krishna M. Pillai. Modeling the Unsaturated Flow in Liquid Composite Molding Processes: A Review and Some Thoughts. *Journal of Composite Materials*, 38(23):2097–2118, dec 2004.
- [39] Joël Bréard, Yann Henzel, François Trochu, and Raymond Gauvin. Analysis of dynamic flows through porous media. Part I: Comparison between saturated and unsaturated flows in fibrous reinforcements. *Polymer Composites*, 24(3):391–408, jun 2003.
- [40] Chung Hae Park and Patricia Krawczak. Unsaturated and Saturated Permeabilities of Fiber Reinforcement: Critics and Suggestions. *Frontiers in Materials*, 2:38, apr 2015.
- [41] Sung H Kim, Jae W Jung, Mei X Li, Sung W Choi, Woo I Lee, and Chung H Park. Unsaturated flow behavior in double-scale porous reinforcement for liquid composite molding processes. *Journal of Reinforced Plastics and Composites*, 36(2):85–97, jan 2017.
- [42] P.C. Carman. Fluid flow through granular beds. *Chemical Engineering Research and Design*, 75:S32–S48, dec 1997.
- [43] Gastón Francucci, Exequiel S. Rodríguez, and Analía Vázquez. Experimental study of the compaction response of jute fabrics in liquid composite molding processes. *Journal of Composite Materials*, 46(2):155–167, jan 2012.
- [44] Van Hau Nguyen, Mylène Lagardère, Chung Hae Park, and Stéphane Panier. Permeability of natural fiber reinforcement for liquid composite molding processes. *Journal of Materials Science*, 49(18):6449–6458, sep 2014.
- [45] Monica Francesca Pucci, Pierre-Jacques Liotier, and Sylvain Drapier. Tensiometric method to reliably assess wetting properties of single fibers with resins: Validation on cellulosic reinforcements for composites. *Colloids and Surfaces A: Physicochemical and Engineering Aspects*, 512:26–33, 2017.
- [46] Hua Tan and Krishna M. Pillai. Multiscale modeling of unsaturated flow in dual-scale fiber preforms of liquid composite molding III: Reactive flows. *Composites Part A: Applied Science and Manufacturing*, 43(1):29–44, jan 2012.
- [47] Boris Gourichon, Mylène Deléglise, Christophe Binetruy, and Patricia Krawczak. Dynamic void content prediction during radial injection in liquid composite molding. *Composites Part A: Applied Science and Manufacturing*, 39(1):46–55, jan 2008.

- [48] Arthur Babeau, Sébastien Comas-Cardona, Christophe Binetruy, and Gilles Orange. Modeling of heat transfer and unsaturated flow in woven fiber reinforcements during direct injection-pultrusion process of thermoplastic composites. *Composites Part A: Applied Science and Manufacturing*, 77:310–318, oct 2015.
- [49] Gastón Francucci, Exequiel S. Rodríguez, and Analía Vázquez. Study of saturated and unsaturated permeability in natural fiber fabrics. *Composites Part A: Applied Science and Manufacturing*, 41(1):16–21, 2010.
- [50] R. Masoodi, K. M. Pillai, N. Grahl, and H. Tan. Numerical simulation of LCM mold-filling during the manufacture of natural fiber composites. *Journal of Reinforced Plastics and Composites*, 31(6):363–378, mar 2012.
- [51] David R Schuchardtl and John C Berg. Wood and fiber science.
- [52] A Javadi, KM Pillai, and R Sabo. An experimental estimation of liquid absorption coefficient for cellulose nanofiber films. In *11th International Conference on Flow Processess in Composite Materials (FPCM11)*, pages 9–12, Auckland, 2012.
- [53] Chung Hae Park, Aurélie Lebel, Abdelghani Saouab, Joël Bréard, and Woo Il Lee. Modeling and simulation of voids and saturation in liquid composite molding processes. *Composites Part A: Applied Science and Manufacturing*, 42(6):658–668, jun 2011.
- [54] Youssef K. Hamidi, Levent Aktas, and M. Cengiz Altan. Formation of Microscopic Voids in Resin Transfer Molded Composites. *Journal of Engineering Materials and Technology*, 126(4):420, oct 2004.
- [55] T.S. Lundstrom, B.R. Gebart, and C.Y. Lundemo. Void Formation in RTM. *Journal of Reinforced Plastics and Composites*, 12(12):1339–1349, dec 1993.
- [56] T. Staffan Lundström and B. Rikard Gebart. Influence from process parameters on void formation in resin transfer molding. *Polymer Composites*, 15(1):25–33, feb 1994.
- [57] V. Rohatgi, N. Patel, and L. James Lee. Experimental investigation of flow-induced microvoids during impregnation of unidirectional stitched fiberglass mat. *Polymer Composites*, 17(2):161–170, apr 1996.
- [58] N. Patel, V. Rohatgi, and L. James Lee. Micro scale flow behavior and void formation mechanism during impregnation through a unidirectional stitched fiberglass mat. *Polymer Engineering and Science*, 35(10):837–851, may 1995.

- [59] N. Patel and L. James Lee. Modeling of void formation and removal in liquid composite molding. Part I: Wettability analysis. *Polymer Composites*, 17(1):96–103, feb 1996.
- [60] Jean Sébastien Leclerc and Edu Ruiz. Porosity reduction using optimized flow velocity in Resin Transfer Molding. *Composites Part A: Applied Science and Manufacturing*, 39(12):1859–1868, 2008.
- [61] C. Ravey, E. Ruiz, and F. Trochu. Determination of the optimal impregnation velocity in Resin Transfer Molding by capillary rise experiments and infrared thermography. *Composites Science and Technology*, 99:96–102, jul 2014.
- [62] B. Gourichon, C. Binetruy, and P. Krawczak. A new numerical procedure to predict dynamic void content in liquid composite molding. *Composites Part A: Applied Science and Manufacturing*, 37(11):1961–1969, nov 2006.
- [63] Baris Caglar, Cem Tekin, Feyza Karasu, and Véronique Michaud. Assessment of Capillary Phenomena in Liquid Composite Molding. *Composites Part A: Applied Science and Manufacturing*, feb 2019.
- [64] Philippe Causse, Christophe Ravey, François Trochu, Philippe Causse, Christophe Ravey, and François Trochu. Capillary Characterization of Fibrous Reinforcement and Optimization of Injection Strategy in Resin Transfer Molding. *Journal of Composites Science*, 2(2):19, mar 2018.
- [65] François LeBel, Amir Ershad Fanaei, Eduardo Ruiz, and François Trochu. Experimental characterization by fluorescence of capillary flows in dual-scale engineering fabrics. *Textile Research Journal*, 83(15):1634–1659, sep 2013.
- [66] Moon Koo Kang, Woo Il Lee, and H.Thomas Hahn. Formation of microvoids during resin-transfer molding process. *Composites Science and Technology*, 60(12-13):2427–2434, sep 2000.
- [67] E. Ruiz, V. Achim, S. Soukane, F. Trochu, and J. Bréard. Optimization of injection flow rate to minimize micro/macro-voids formation in resin transfer molded composites. *Composites Science and Technology*, 66(3-4):475–486, mar 2006.
- [68] L. Zingraff, V. Michaud, P.-E. Bourban, and J.-A.E. Månson. Resin transfer moulding of anionically polymerised polyamide 12. *Composites Part A: Applied Science and Manufacturing*, 36(12):1675–1686, dec 2005.

- [69] Sébastien Gueroult, Aurélie Lebel-Lavacry, Chung Hae Park, Laurent Bizet, Abdelghani Saouab, and Joël Bréard. Analytical modeling and in situ measurement of void formation in liquid composite molding processes. *Advanced Composite Materials*, 23(1):31–42, jan 2013.
- [70] Bouchra Aaboud, Abdelghani Saouab, and Yasir Nawab. Simulation of air bubble’s creation, compression, and transport phenomena in resin transfer moulding. *Journal of Composite Materials*, 51(29):4115–4127, dec 2017.
- [71] Ryosuke Matsuzaki, Daigo Seto, Akira Todoroki, and Yoshihiro Mizutani. Void formation in geometry–anisotropic woven fabrics in resin transfer molding. *Advanced Composite Materials*, 23(2):99–114, mar 2014.
- [72] Maxime Villière, Sébastien Guérout, Vincent Sobotka, Nicolas Boyard, Joël Bréard, and Didier Delaunay. Dynamic saturation curve measurement in liquid composite molding by heat transfer analysis. *Composites Part A: Applied Science and Manufacturing*, 69:255–265, feb 2015.
- [73] Ryosuke Matuzaki, Daigo Seto, Masaki Naito, Akira Todoroki, and Yoshihiro Mizutani. Analytical prediction of void formation in geometrically anisotropic woven fabrics during resin transfer molding. *Composites Science and Technology*, 107:154–161, feb 2015.
- [74] Joaquim Vilà, Federico Sket, Fabian Wilde, Guillermo Requena, Carlos González, and Javier LLorca. An in situ investigation of microscopic infusion and void transport during vacuum-assisted infiltration by means of X-ray computed tomography. *Composites Science and Technology*, 119:12–19, nov 2015.
- [75] Natalie M. Larson and Frank W. Zok. Insights from in-situ X-ray computed tomography during axial impregnation of unidirectional fiber beds. *Composites Part A: Applied Science and Manufacturing*, 107:124–134, 2018.
- [76] F. Gommer, A. Endruweit, and A.C. Long. Quantification of micro-scale variability in fibre bundles. *Composites Part A: Applied Science and Manufacturing*, 87:131–137, aug 2016.
- [77] Si Hwan Kim and Chung Hae Park. Direct impregnation of thermoplastic melt into flax textile reinforcement for semi-structural composite parts. *Industrial Crops and Products*, 95:651–663, 2017.

- [78] Mahoor Mehdikhani, Larissa Gorbatiikh, Ignaas Verpoest, and Stepan V Lomov. Voids in fiber-reinforced polymer composites: A review on their formation, characteristics, and effects on mechanical performance. *Journal of Composite Materials*, 53(12):1579–1669, may 2019.
- [79] Yuri Nikishkov, Luca Airoidi, and Andrew Makeev. Measurement of voids in composites by x-ray computed tomography. *Composites Science and Technology*, 89:89 – 97, 2013.
- [80] Lut Pil, Farida Bensadoun, Julie Pariset, and Ignaas Verpoest. Why are designers fascinated by flax and hemp fibre composites? *Composites Part A: Applied Science and Manufacturing*, 83:193–205, 2016.
- [81] Michaël Berges, Romain Léger, Vincent Placet, Véronique Person, Stéphane Corn, Xavier Gabrion, Jérôme Rousseau, Emmanuel Ramasso, Patrick Ienny, and Stéphane Fontaine. Influence of moisture uptake on the static, cyclic and dynamic behaviour of unidirectional flax fibre-reinforced epoxy laminates. *Composites Part A: Applied Science and Manufacturing*, 88:165–177, sep 2016.
- [82] Gábor Romhány, József Karger-Kocsis, and Tibor Czigány. Tensile fracture and failure behavior of thermoplastic starch with unidirectional and cross-ply flax fiber reinforcements. *Macromolecular Materials and Engineering*, 288(9):699–707, sep 2003.
- [83] Christophe Baley, Yves Perrot, Frederic Busnel, Herve Guezenoc, and Peter Davies. Transverse tensile behaviour of unidirectional plies reinforced with flax fibres. *Materials Letters*, 60(24):2984–2987, oct 2006.
- [84] Ihab El Sawi, Zouheir Fawaz, Redouane Zitoune, and Habiba Bougherara. An investigation of the damage mechanisms and fatigue life diagrams of flax fiber-reinforced polymer laminates. *Journal of Materials Science*, 49(5):2338–2346, mar 2014.
- [85] Malika Kersani, Stepan V Lomov, Aart Willem Van Vuure, Ahcène Bouabdallah, and Ignaas Verpoest. Damage in flax/epoxy quasi-unidirectional woven laminates under quasi-static tension. *Journal of Composite Materials*, 49(4):403–413, feb 2015.
- [86] Zia Mahboob and Habiba Bougherara. Fatigue of flax-epoxy and other plant fibre composites: Critical review and analysis. *Composites Part A: Applied Science and Manufacturing*, 109:440–462, jun 2018.

- [87] Bo Madsen, Preben Hoffmeyer, and Hans Lilholt. Hemp yarn reinforced composites – II. Tensile properties. *Composites Part A: Applied Science and Manufacturing*, 38(10):2204–2215, oct 2007.
- [88] A. K. Mohanty, M. Misra, and L. T. Drzal. Surface modifications of natural fibers and performance of the resulting biocomposites: An overview. *Composite Interfaces*, 8(5):313–343, jan 2001.
- [89] Justin Merotte, Antoine Le Duigou, Antoine Kervoelen, Alain Bourmaud, Karim Behlouli, Olivier Sire, and Christophe Baley. Flax and hemp nonwoven composites: The contribution of interfacial bonding to improving tensile properties. *Polymer Testing*, 66:303–311, apr 2018.
- [90] Nina Graupner, Joraine Rößler, Gerhard Ziegmann, and Jörg Müssig. Fibre/matrix adhesion of cellulose fibres in PLA, PP and MAPP: A critical review of pull-out test, microbond test and single fibre fragmentation test results. *Composites Part A: Applied Science and Manufacturing*, 63:133–148, 2014.
- [91] Yonghui Zhou, Mizi Fan, and Lihui Chen. Interface and bonding mechanisms of plant fibre composites: An overview. *Composites Part B: Engineering*, 101:31–45, sep 2016.
- [92] Mustafa Aslan, Gary Chinga-Carrasco, Bent F. Sørensen, and Bo Madsen. Strength variability of single flax fibres. In *Journal of Materials Science*, volume 46, pages 6344–6354. Springer US, oct 2011.
- [93] K.L. Pickering, M.G. Aruan Efendy, and T.M. Le. A review of recent developments in natural fibre composites and their mechanical performance. *Composites Part A: Applied Science and Manufacturing*, 83:98–112, 2016.
- [94] Gaston Francucci, Stuart Palmer, and Wayne Hall. External compaction pressure over vacuum-bagged composite parts: Effect on the quality of flax fiber/epoxy laminates. *Journal of Composite Materials*, page 002199831770199, mar 2017.
- [95] Justin Merotte, Antoine Le Duigou, Alain Bourmaud, Karim Behlouli, and Christophe Baley. Mechanical and acoustic behaviour of porosity controlled randomly dispersed flax/PP biocomposite. *Polymer Testing*, 51:174–180, 2016.
- [96] H. Santamala, R. Livingston, H. Sixta, M. Hummel, M. Skrifvars, and O. Saarela. Advantages of regenerated cellulose fibres as compared to flax fibres in the processability and mechanical performance of thermoset composites. *Composites Part A: Applied Science and Manufacturing*, 84:377–385, may 2016.

- [97] Yan Li and Bing Xue. Hydrothermal ageing mechanisms of unidirectional flax fabric reinforced epoxy composites. *Polymer Degradation and Stability*, 126:144–158, apr 2016.
- [98] Behnaz Baghaei, Mikael Skrifvars, and Lena Berglin. Manufacture and characterisation of thermoplastic composites made from PLA/hemp co-wrapped hybrid yarn prepregs. *Composites Part A: Applied Science and Manufacturing*, 50:93–101, jul 2013.
- [99] J. Schuster, Q. Govignon, and S. Bickerton. Processability of Biobased Thermoset Resins and Flax Fibres Reinforcements Using Vacuum Assisted Resin Transfer Moulding. *Open Journal of Composite Materials*, 04(01):1–11, jan 2014.
- [100] Arnaud Regazzi, Stéphane Corn, Patrick Ienny, and Anne Bergeret. Coupled hydro-mechanical aging of short flax fiber reinforced composites. *Polymer Degradation and Stability*, 130:300–306, aug 2016.
- [101] Arnaud Regazzi, Stéphane Corn, Patrick Ienny, Jean-Charles Bénézet, and Anne Bergeret. Reversible and irreversible changes in physical and mechanical properties of biocomposites during hydrothermal aging. *Industrial Crops and Products*, 84:358–365, jun 2016.
- [102] Monica Francesca Pucci, Pierre-Jacques Liotier, David Seveno, Carlos Fuentes, Aart Van Vuure, and Sylvain Drapier. Wetting and swelling property modifications of elementary flax fibres and their effects on the Liquid Composite Molding process. *Composites Part A: Applied Science and Manufacturing*, 97:31–40, jun 2017.
- [103] Monica Francesca Pucci, Pierre Jacques Liotier, and Sylvain Drapier. Capillary wicking in flax fabrics - Effects of swelling in water. *Colloids and Surfaces A: Physicochemical and Engineering Aspects*, 498:176–184, 2016.
- [104] Yan Li, Qian Li, and Hao Ma. The voids formation mechanisms and their effects on the mechanical properties of flax fiber reinforced epoxy composites. *Composites Part A: Applied Science and Manufacturing*, 72:40–48, 2015.
- [105] Thomas Cadu, Michael Berges, Olivier Sicot, Véronique Person, Benoit Piezel, Laetitia Van Schoors, Vincent Placet, Stéphane Corn, Romain Léger, Loïc Divet, Patrick Ienny, and Stéphane Fontaine. What are the key parameters to produce a high-grade bio-based composite? Application to flax/epoxy UD laminates produced by thermocompression. *Composites Part B: Engineering*, 150:36–46, 2018.

- [106] Farida Bensadoun, Ignaas Verpoest, J Baets, J Müssig, Nina Graupner, Peter Davies, Moussa Gomina, Antoine Kervoelen, and Christophe Baley. Impregnated fibre bundle test for natural fibres used in composites. *Journal of Reinforced Plastics and Composites*, 36(13):942–957, jul 2017.
- [107] Xing Jin, Xie Chen, Qian Cheng, Naiwen Zhang, Shenyang Cai, and Jie Ren. Non-isothermal crystallization kinetics of ramie fiber-reinforced polylactic acid biocomposite.
- [108] F. Duc, P.E. Bourban, C.J.G. Plummer, and J.-A.E. Månson. Damping of thermoset and thermoplastic flax fibre composites. *Composites Part A: Applied Science and Manufacturing*, 64:115–123, 2014.
- [109] Jinchun Zhu, Huijun Zhu, James Njuguna, and Hrushikesh Abhyankar. Recent Development of Flax Fibres and Their Reinforced Composites Based on Different Polymeric Matrices. *Materials*, 6(11):5171–5198, nov 2013.
- [110] W V Srubar and S L Billington. A micromechanical model for moisture-induced deterioration in fully biorenewable wood–plastic composites. 50(Supplement C):81–92.
- [111] A. Le Duigou, P. Davies, and C. Baley. Seawater ageing of flax/poly(lactic acid) biocomposites. *Polymer Degradation and Stability*, 94(7):1151–1162, jul 2009.
- [112] T.S. Mesogitis, A.A. Skordos, and A.C. Long. Uncertainty in the manufacturing of fibrous thermosetting composites: A review. *Composites Part A: Applied Science and Manufacturing*, 57:67–75, feb 2014.
- [113] C. Baley, A. Le Duigou, A. Bourmaud, and P. Davies. Influence of drying on the mechanical behaviour of flax fibres and their unidirectional composites. *Composites Part A: Applied Science and Manufacturing*, 43(8):1226–1233, 2012.
- [114] Antoine le Duigou, Justin Merotte, Alain Bourmaud, Peter Davies, Karim Belhouli, and Christophe Baley. Hygroscopic expansion: A key point to describe natural fibre/polymer matrix interface bond strength. *Composites Science and Technology*, 151:228–233, oct 2017.
- [115] Monica Francesca Pucci, Pierre-Jacques Liotier, and Sylvain Drapier. Capillary wicking in a fibrous reinforcement – Orthotropic issues to determine the capillary pressure components. *Composites Part A: Applied Science and Manufacturing*, 77:133–141, 2015.

- [116] K D Potter. Understanding the origins of defects and variability in composites manufacture. In *International Conference on Composite Materials (ICCM)-17*, 2009.
- [117] Jiuping Rao, Yonghui Zhou, Mizi Fan, Jiuping Rao, Yonghui Zhou, and Mizi Fan. Revealing the Interface Structure and Bonding Mechanism of Coupling Agent Treated WPC. *Polymers*, 10(3):266, mar 2018.
- [118] Monica Francesca Pucci, Pierre-Jacques Jacques Liotier, and Sylvain Drapier. No Title. *Colloids and Surfaces A: Physicochemical and Engineering Aspects*, 498:176–184, 2016.
- [119] Christophe Baley, Frédéric Busnel, Yves Grohens, and Olivier Sire. Influence of chemical treatments on surface properties and adhesion of flax fibre-polyester resin. *Composites Part A: Applied Science and Manufacturing*, 37(10):1626–1637, 2006.
- [120] Guillermo Cantero, Aitor Arbelaiz, Rodrigo Llano-Ponte, and Iñaki Mondragon. Effects of fibre treatment on wettability and mechanical behaviour of flax/polypropylene composites. *Composites Science and Technology*, 63(9):1247–1254, jul 2003.
- [121] S. Rajkumar, Jimi Tjong, S.K. Nayak, and M. Sain. Permeability and mechanical property correlation of bio based epoxy reinforced with unidirectional sisal fiber mat through vacuum infusion molding technique. *Polymer Composites*, 38(10):2192–2200, oct 2017.
- [122] Huihui Zhang, Ruihao Ming, Gesheng Yang, Yuzeng Li, Qiao Li, and Huili Shao. Influence of alkali treatment on flax fiber for use as reinforcements in polylactide stereocomplex composites. *Polymer Engineering & Science*, 55(11):2553–2558, nov 2015.
- [123] Product Data Sheet. PrimeTM 27. pages 1–8.
- [124] Zhan-Sheng Guo, Shanyi Du, and Boming Zhang. Temperature field of thick thermoset composite laminates during cure process. *Composites Science and Technology*, 65(3-4):517–523, mar 2005.
- [125] Haomiao Yang. *Study of a unidirectional flax reinforcement for biobased composite*. PhD thesis, Normandie Université, 2017.
- [126] Charlotte Campana, Romain Leger, Rodolphe Sonnier, Laurent Ferry, and Patrick Ienny. Effect of post curing temperature on mechanical properties of a flax fiber reinforced epoxy composite. *Composites Part A: Applied Science and Manufacturing*, 107:171–179, apr.

- [127] R. J. Crowson and R. G. C. Arridge. The elastic properties in bulk and shear of a glass bead-reinforced epoxy resin composite. *Journal of Materials Science*, 12(11):2154–2164, nov 1977.
- [128] Dipa Ray, B.K. Sarkar, S. Das, and A.K. Rana. Dynamic mechanical and thermal analysis of vinylester-resin-matrix composites reinforced with untreated and alkali-treated jute fibres. *Composites Science and Technology*, 62(7-8):911–917, jun 2002.
- [129] Daiane Romanzini, Alessandra Lavoratti, Heitor L. Ornaghi, Sandro C. Amico, and Ademir J. Zattera. Influence of fiber content on the mechanical and dynamic mechanical properties of glass/ramie polymer composites. *Materials & Design*, 47:9–15, may 2013.
- [130] J Acera Fernandez, N Le Moigne, AS Caro-Bretelle, R El Hage, A Le Duc, M Lozachemur, P Bono, and Anne Bergeret. Role of flax cell wall components on the microstructure and transverse mechanical behaviour of flax fabrics reinforced epoxy biocomposites. *Industrial Crops and Products*, 85:93–108, jul 2016.
- [131] B.S. Rao and Aruna Palanisamy. Synthesis of bio based low temperature curable liquid epoxy, benzoxazine monomer system from cardanol: Thermal and viscoelastic properties. *European Polymer Journal*, 49(8):2365–2376, aug 2013.
- [132] Antoine Le Duigou, Antoine Kervoelen, Adélaïde Le Grand, Michel Nardin, and Christophe Baley. Interfacial properties of flax fibre–epoxy resin systems: Existence of a complex interphase. *Composites Science and Technology*, 100:152–157, aug 2014.
- [133] Min Li, Chao Yuan, Shao Kai Wang, Yi Zhuo Gu, Kevin Potter, and Zuo Guang Zhang. Evolution of the wettability between carbon fiber and epoxy as a function of temperature and resin curing. *Journal of Applied Polymer Science*, 128(6):4095–4101, jun 2013.
- [134] Pierre-Jacques Liotier, Monica Francesca Pucci, and Sylvain Drapier. Evaluation by wicking tests of capillary pressure as function of temperature for uncured resins. In *The 14th international conference on flow processing in composite materials*, Lulea, 2018.
- [135] F. Bensadoun, K.A.M. Vallons, L.B. Lessard, I. Verpoest, and A.W. Van Vuure. Fatigue behaviour assessment of flax–epoxy composites. *Composites Part A: Applied Science and Manufacturing*, 82:253–266, mar 2016.

- [136] Farida Bensadoun. *In-service behaviour of flax fiber reinforced composites for high performance applications*. PhD thesis, 2016.
- [137] Rachel Koh and Bo Madsen. Strength failure criteria analysis for a flax fibre reinforced composite. *Mechanics of Materials*, 124:26–32, sep 2018.
- [138] K. Oksman. High Quality Flax Fibre Composites Manufactured by the Resin Transfer Moulding Process. *Journal of Reinforced Plastics and Composites*, 20(7):621–627, may 2001.
- [139] J. Verrey, V. Michaud, and J.-A.E. Månson. Dynamic capillary effects in liquid composite moulding with non-crimp fabrics. *Composites Part A: Applied Science and Manufacturing*, 37(1):92–102, 2006.
- [140] A Mortensen, C San Marchi, and V J Michaud. Capillarity in infiltration processing: a review of principles and their extension to reactive infiltration. In *Proceedings international conference high temperature capillarity, Cracow, Poland*, pages 249–261, 1997.
- [141] Véronique Michaud, Markus Nordlund, Staffan Lundström, and J E Månsson. Capillary phenomena in liquid composite moulding. In *International Conference on Composite Materials: 08/07/2007-13/07/2007*, 2007.
- [142] T. Young. An Essay on the Cohesion of Fluids. *Philosophical Transactions of the Royal Society of London*, 95(0):65–87, jan 1805.
- [143] C N C Lam, R Wu, D Li, M L Hair, and A W Neumann. Study of the advancing and receding contact angles: liquid sorption as a cause of contact angle hysteresis. *Advances in colloid and interface science*, 96(1):169–191, 2002.
- [144] A. B. D. Cassie and S. Baxter. Wettability of porous surfaces. *Transactions of the Faraday Society*, 40(0):546, 1944.
- [145] José Bico. *Mécanismes d’imprégnation : Surfaces texturées, Bigouttes, Poreux*. PhD thesis, Université de Paris VI, 2000.
- [146] Robert N. Wenzel. RESISTANCE OF SOLID SURFACES TO WETTING BY WATER. *Industrial & Engineering Chemistry*, 28(8):988–994, aug 1936.
- [147] J. F. Joanny and P. G. de Gennes. A model for contact angle hysteresis. *The Journal of Chemical Physics*, 81(1):552–562, jul 1984.

- [148] Jacco H. Snoeijer and Bruno Andreotti. Moving Contact Lines: Scales, Regimes, and Dynamical Transitions. *Annual Review of Fluid Mechanics*, 45(1):269–292, jan 2013.
- [149] Daniel Bonn, Jens Eggers, Joseph Indekeu, Jacques Meunier, and Etienne Rolley. Wetting and spreading. *Rev. Mod. Phys.*, 81(2):739–805, 2009.
- [150] Mohamed Amine Ben Abdelwahed. Mécanismes d’imprégnation en milieux fibreux: Modélisation et application à la mise en oeuvre des matériaux composites à fibres longues, 2011.
- [151] Yulii D Shikhmurzaev. Singularities at the moving contact line. Mathematical, physical and computational aspects. *Physica D: Nonlinear Phenomena*, 217(2):121–133, 2006.
- [152] Weiqing Ren and Weinan E. Boundary conditions for the moving contact line problem. *Physics of Fluids*, 19(2):022101, feb 2007.
- [153] Yuehua Yuan and T. Randall Lee. Contact Angle and Wetting Properties. pages 3–34. Springer Berlin Heidelberg, 2013.
- [154] F R Milot, G Lebrun, and F Brouillette. WETTABILITY EVALUATION OF ACETYLATED FLAX AND KRAFT FIBERS USING THE DROP SHAPE METHOD. In *ICCM-19*, Montreal, Canada, 2013.
- [155] A. W. Neumann and R. J. Good. Techniques of Measuring Contact Angles. In *Surface and Colloid Science*, pages 31–91. Springer US, Boston, MA, 1979.
- [156] David Quéré and Jean-Marc Di Meglio. The meniscus on a fibre. *Advances in Colloid and Interface Science*, 48:141–150, apr 1994.
- [157] David F James. The meniscus on the outside of a small circular cylinder. *Journal of Fluid Mechanics*, 63(4):657–664, 1974.
- [158] Daniel Hansen, Niels Bomholt, Jonas Camillus Jeppesen, and Adam Cohen Simonson. Contact angle goniometry on single micron-scale fibers for composites. *Applied Surface Science*, 392:181–188, 2017.
- [159] Camille Goudenhoofft, Alain Bourmaud, and Christophe Baley. Varietal selection of flax over time: Evolution of plant architecture related to influence on the mechanical properties of fibers. *Industrial Crops and Products*, 97:56–64, 2017.

- [160] G. Van Gansen, D. Perremans, C.A. Fuentes, A.W. Van Vuure and D. Seveno. Surface characterization of natural fibers. do's and don'ts. In *In Fall 2014 Fiber Society Conference*, 2014.
- [161] Reza Masoodi, Krishna M. Pillai, and Padma Prabodh Varanasi. Role of Hydraulic and Capillary Radii in Improving the Effectiveness of Capillary Model in Wicking. In *Volume 1: Symposia, Parts A and B*, pages 251–259. ASME, 2008.
- [162] Edward W. Washburn. The Dynamics of Capillary Flow. *Physical Review*, 17(3):273–283, mar 1921.
- [163] C.H. Bosanquet. On the flow of liquids into capillary tubes. *Philosophical Magazine Series 6*, 45(267):525–531, mar 1923.
- [164] N. Fries and M. Dreyer. The transition from inertial to viscous flow in capillary rise. *Journal of Colloid and Interface Science*, 327(1):125–128, 2008.
- [165] N. Fries and M. Dreyer. An analytic solution of capillary rise restrained by gravity. *Journal of Colloid and Interface Science*, 320(1):259–263, 2008.
- [166] Reza Masoodi and Krishna M Pillai. Darcy's law-based model for wicking in paper-like swelling porous media. *AIChE journal*, 56(9):2257–2267, 2010.
- [167] Monica Francesca Pucci, Pierre-Jacques Jacques Liotier, and Sylvain Drapier. No Title. *Composites Part A: Applied Science and Manufacturing*, 77:257–265, 2015.
- [168] Ibon Aranberri-Askargorta, Thomas Lampke, and Alexander Bismarck. Wetting behavior of flax fibers as reinforcement for polypropylene. *Journal of Colloid and Interface Science*, 263(2):580–589, 2003.
- [169] T. Stuart, R.D. McCall, H.S.S. Sharma, and G. Lyons. Modelling of wicking and moisture interactions of flax and viscose fibres. *Carbohydrate Polymers*, 123:359–368, 2015.
- [170] F. C. Blake. The Resistance of Packing to Fluid Flow. *American Institute of Chemical Engineers*, 14:415–421, 1922.
- [171] K. Charlet, J.P. Jernot, S. Eve, M. Gomina, and J. Bréard. Multi-scale morphological characterisation of flax: From the stem to the fibrils. *Carbohydrate Polymers*, 82(1):54–61, 2010.
- [172] C.A. Fuentes, L.Q.N. Tran, C. Dupont-Gillain, W. Vanderlinden, S. De Feyter, A.W. Van Vuure, and I. Verpoest. Wetting behaviour and surface properties of

- technical bamboo fibres. *Colloids and Surfaces A: Physicochemical and Engineering Aspects*, 380(1-3):89–99, may 2011.
- [173] Hua Tan and Krishna M. Pillai. Finite element implementation of stress-jump and stress-continuity conditions at porous-medium, clear-fluid interface. *Computers and Fluids*, 38(6):1118–1131, jun 2009.
 - [174] Hua Tan and Krishna M. Pillai. Multiscale modeling of unsaturated flow of dual-scale fiber preform in liquid composite molding II: Non-isothermal flows. *Composites Part A: Applied Science and Manufacturing*, 43(1):14–28, jan 2012.
 - [175] M. Amin F. Zarandi, Salvador Arroyo, and Krishna M. Pillai. Longitudinal and Transverse Flows in Fiber Tows: Evaluation of Theoretical Permeability Models through Numerical Predictions and Experimental Measurements. *Composites Part A: Applied Science and Manufacturing*, jan 2019.
 - [176] B.R. Gebart. Permeability of Unidirectional Reinforcements for RTM. *Journal of Composite Materials*, 26(8):1100–1133, aug 1992.
 - [177] Mayur G. Godbole, Rahul Purandare, Rahul Harshe, Avinash Hood, Suhasini Gururaja, Makarand Joshi, and Suresh Advani. Influence of filament distribution on transverse tow permeability: Model predictions and experimental validation. *Composites Part A: Applied Science and Manufacturing*, 118:150–161, mar 2019.
 - [178] Alexander L. Berdichevsky and Zhong Cai. Preform permeability predictions by self-consistent method and finite element simulation. *Polymer Composites*, 14(2):132–143, apr 1993.
 - [179] Sinzi Kuwabara. The Forces experienced by Randomly Distributed Parallel Circular Cylinders or Spheres in a Viscous Flow at Small Reynolds Numbers. *Journal of the Physical Society of Japan*, 14(4):527–532, apr 1959.
 - [180] Ali Tamayol and Majid Bahrami. Transverse permeability of fibrous porous media. *Physical Review E - Statistical, Nonlinear, and Soft Matter Physics*, 83(4):046314, apr 2011.
 - [181] Josias Van Der Westhuizen and J. Prieur Du Plessis. An attempt to quantify fibre bed permeability utilizing the phase average Navier-Stokes equation. *Composites Part A: Applied Science and Manufacturing*, 27(4 PART A):263–269, jan 1996.
 - [182] Mark A. Knackstedt and J. Prieur Duplessis. Simple permeability model for natural granular media. *Geophysical Research Letters*, 23(13):1609–1612, jun 1996.

- [183] Y Liu, D Vasiukov, and Stephane Panier. A numerical approach to reconstruct mesoscopic yarn section of textile composites based upon X-ray. In *23ème Congrès Français de Mécanique*, pages 1–9, Lille, 2017.
- [184] Comsol. Introduction to COMSOL Multiphysics. Technical report, 2017.
- [185] Masoud Bodaghi, Giuseppe Catalanotti, and Nuno Correia. On the statistics of transverse permeability of randomly distributed fibers. *Composite Structures*, 158:323–332, dec 2016.
- [186] Frank Gommer, Andreas Endruweit, and Andrew C Long. Influence of the microstructure on saturated transverse flow in fibre arrays. *Journal of Composite Materials*, 52(18):2463–2475, aug 2018.
- [187] Xiaoming Chen and Thanasis D. Papathanasiou. On the variability of the Kozeny constant for saturated flow across unidirectional disordered fiber arrays. *Composites Part A: Applied Science and Manufacturing*, 37(6):836–846, jun 2006.
- [188] K. Yazdchi, S. Srivastava, and S. Luding. Micro–macro relations for flow through random arrays of cylinders. *Composites Part A: Applied Science and Manufacturing*, 43(11):2007–2020, nov 2012.
- [189] Meriem El Boustani, Gilbert Lebrun, François Brouillette, and Ahmed Belfkira. Effect of a solvent-free acetylation treatment on reinforcements permeability and tensile behaviour of flax/epoxy and flax/wood fibre/epoxy composites. *The Canadian Journal of Chemical Engineering*, 95(6):1082–1092, jun 2017.
- [190] Ehsan Ameri, Gilbert Lebrun, and Luc Laperrière. In-plane permeability characterization of a unidirectional flax/paper reinforcement for liquid composite molding processes. *Composites Part A: Applied Science and Manufacturing*, 85:52–64, 2016.
- [191] Michael Ehresmann, Ali Amiri, and Chad Ulven. The effect of different variables on in-plane radial permeability of natural fiber mats. *Journal of Reinforced Plastics and Composites*, page 073168441664645, apr 2016.
- [192] Johannes Schindelin, Ignacio Arganda-Carreras, Erwin Frise, Verena Kaynig, Mark Longair, Tobias Pietzsch, Stephan Preibisch, Curtis Rueden, Stephan Saalfeld, Benjamin Schmid, Jean-Yves Tinevez, Daniel James White, Volker Hartenstein, Kevin Eliceiri, Pavel Tomancak, and Albert Cardona. Fiji: an open-source platform for biological-image analysis. *Nature Methods*, 9(7):676–682, jul 2012.

- [193] A. Endruweit, F. Gommer, and A. C. Long. Stochastic analysis of fibre volume fraction and permeability in fibre bundles with random filament arrangement. *Composites Part A: Applied Science and Manufacturing*, 49:109–118, jun 2013.
- [194] Van-Hau Nguyen. *Characterization and modeling of flax fiber reinforced composites manufacturing by resin transfer molding process*. PhD thesis, 2014. Université de Lille 1.
- [195] Darshil U. Shah and Mike J. Clifford. Compaction, Permeability and Flow Simulation for Liquid Composite Moulding of Natural Fibre Composites. In *Manufacturing of Natural Fibre Reinforced Polymer Composites*, pages 65–99. Springer International Publishing, Cham, 2015.
- [196] I.B.C.M. Rocha, S. Raijmaekers, R.P.L. Nijssen, F.P. van der Meer, and L.J. Sluys. Hygrothermal ageing behaviour of a glass/epoxy composite used in wind turbine blades. *Composite Structures*, 174:110–122, aug 2017.
- [197] Y.I. Tsai, E.J. Bosze, E. Barjasteh, and S.R. Nutt. Influence of hygrothermal environment on thermal and mechanical properties of carbon fiber/fiberglass hybrid composites. *Composites Science and Technology*, 69(3-4):432–437, mar 2009.
- [198] Sabina Alessi, Giuseppe Pitarresi, and Giuseppe Spadaro. Effect of hydrothermal ageing on the thermal and delamination fracture behaviour of CFRP composites. *Composites Part B: Engineering*, 67:145–153, dec 2014.
- [199] Pei Sun, Yan Zhao, Yunfeng Luo, and Lili Sun. Effect of temperature and cyclic hygrothermal aging on the interlaminar shear strength of carbon fiber/bismaleimide (BMI) composite. *Materials & Design*, 32(8-9):4341–4347, sep 2011.
- [200] Andrea Toscano, Giuseppe Pitarresi, Michele Scafidi, Maria Di Filippo, Giuseppe Spadaro, and Sabina Alessi. Water diffusion and swelling stresses in highly crosslinked epoxy matrices. *Polymer Degradation and Stability*, 133:255–263, nov 2016.
- [201] Arnaud Regazzi, Romain Léger, Stéphane Corn, and Patrick Ienny. Modeling of hydrothermal aging of short flax fiber reinforced composites. *Composites Part A: Applied Science and Manufacturing*, 90:559–566, 2016.
- [202] Fang Tian, Zheng Zhong, and Yihui Pan. Modeling of natural fiber reinforced composites under hygrothermal ageing. *Composite Structures*, 200:144–152, sep 2018.

- [203] Yihui Pan and Zheng Zhong. A micromechanical model for the mechanical degradation of natural fiber reinforced composites induced by moisture absorption. *Mechanics of Materials*, 85:7–15, 2015.
- [204] Amandine Céline, Sylvain Fréour, Frédéric Jacquemin, and Pascal Casari. Characterization and modeling of the moisture diffusion behavior of natural fibers. *Journal of Applied Polymer Science*, 130(1):297–306, oct 2013.
- [205] Abderrazak Chilali, Wajdi Zouari, Mustapha Assarar, Hocine Kebir, and Rezak Ayad. Effect of water ageing on the load-unload cyclic behaviour of flax fibre-reinforced thermoplastic and thermosetting composites. *Composite Structures*, 183:309–319, jan 2018.
- [206] S. G. Prolongo, M. R. Gude, and A. Ureña. Water uptake of epoxy composites reinforced with carbon nanofillers. *Composites Part A: Applied Science and Manufacturing*, 43(12):2169–2175, dec 2012.
- [207] Hongxia Zhao and Robert K Y Li. Effect of water absorption on the mechanical and dielectric properties of nano-alumina filled epoxy nanocomposites. *Composites Part A: Applied Science and Manufacturing*, 39(4):602–611, apr 2008.
- [208] G.Z. Xiao and M.E.R. Shanahan. Swelling of DGEBA/DDA epoxy resin during hygrothermal ageing. *Polymer*, 39(14):3253–3260, jun 1998.
- [209] T. Peret, A. Clement, S. Freour, and F. Jacquemin. Effect of mechanical states on water diffusion based on the free volume theory: Numerical study of polymers and laminates used in marine application. *Composites Part B: Engineering*, 118:54–66, jun 2017.
- [210] Y. El Assami, M. Drissi Habti, V. Raman, and A. Pisupati. Improving delamination strength through CNTs reinforcement: Numerical simulation. In *ECCM 2016 - Proceeding of the 17th European Conference on Composite Materials*, 2016.
- [211] Adolph Fick. On liquid diffusion -reprinted. *Journal of Membrane Science*, 100(1):33–38, mar 1995.
- [212] J Crank. *The mathematics of diffusion*. Clarendon Press, 1975.
- [213] Y. Jack Weitsman. *Fluid Effects in Polymers and Polymeric Composites*. Mechanical Engineering Series. Springer US, Boston, MA, 2012.
- [214] Chi-Hung Shen and George S. Springer. Moisture Absorption and Desorption of Composite Materials. *Journal of Composite Materials*, 10(1):2–20, jan 1976.

- [215] J. Jedidi, F. Jacquemin, and A. Vautrin. Accelerated hygrothermal cyclical tests for carbon/epoxy laminates. *Composites Part A: Applied Science and Manufacturing*, 37(4):636–645, apr 2006.
- [216] Daniel Scida, Mustapha Assarar, Christophe Poilâne, and Rezak Ayad. Influence of hygrothermal ageing on the damage mechanisms of flax-fibre reinforced epoxy composite. *Composites Part B: Engineering*, 48:51–58, may 2013.
- [217] H. N. Dhakal, V. Arumugam, A. Aswinraj, C. Santulli, Z. Y. Zhang, and A. Lopez-Arraiza. Influence of temperature and impact velocity on the impact response of jute/UP composites. *Polymer Testing*, 35:10–19, may 2014.
- [218] H.N. Dhakal, Z.Y. Zhang, and N. Bennett. Influence of fibre treatment and glass fibre hybridisation on thermal degradation and surface energy characteristics of hemp/unsaturated polyester composites. *Composites Part B: Engineering*, 43(7):2757–2761, oct 2012.
- [219] V. Fiore, G. Di Bella, and A. Valenza. The effect of alkaline treatment on mechanical properties of kenaf fibers and their epoxy composites. *Composites Part B: Engineering*, 68:14–21, 2015.
- [220] Rodolphe Sonnier, Belkacem Otazaghine, Amandine Viretto, Guilherme Apolinario, and Patrick Ienny. Improving the flame retardancy of flax fabrics by radiation grafting of phosphorus compounds. *European Polymer Journal*, 68:313–325, jul 2015.
- [221] Raymond Hajj, Roland El Hage, Rodolphe Sonnier, Belkacem Otazaghine, Benjamin Gallard, Sophie Rouif, Michel Nakhl, and José-Marie Lopez-Cuesta. Grafting of phosphorus flame retardants on flax fabrics: Comparison between two routes. *Polymer Degradation and Stability*, 147:25–34, jan 2018.
- [222] M. Rajaei, N. K. Kim, and D. Bhattacharyya. Effects of heat-induced damage on impact performance of epoxy laminates with glass and flax fibres. *Composite Structures*, 185:515–523, feb 2018.
- [223] Mehdi Tajvidi, Nazanin Motie, Ghonche Rassam, Robert H. Falk, and Colin Felton. Mechanical performance of hemp fiber polypropylene composites at different operating temperatures. *Journal of Reinforced Plastics and Composites*, 29(5):664–674, mar 2010.
- [224] International Organisation for Standardisation. Fibre-reinforced plastic composites - Determination of flexural properties - (ISO 14125:1998), 2017.

- [225] International Standards Organization. ISO 14130:1997 Fibre-reinforced plastic composites – Determination of apparent interlaminar shear strength by short-beam method, 2012.
- [226] Ludovic Dumas, Leïla Bonnaud, Marjorie Olivier, Marc Poorteman, and Philippe Dubois. High performance bio-based benzoxazine networks from resorcinol and hydroquinone. *European Polymer Journal*, 75:486–494, feb 2016.
- [227] Ludovic Dumas, Leïla Bonnaud, Marjorie Olivier, Marc Poorteman, and Philippe Dubois. Eugenol-based benzoxazine: from straight synthesis to taming of the network properties. *Journal of Materials Chemistry A*, 3(11):6012–6018, 2015.
- [228] Mael Péron, Amandine Céline, Mickael Castro, Frédéric Jacquemin, and Antoine Le Duigou. Study of hygroscopic stresses in asymmetric biocomposite laminates. *Composites Science and Technology*, 169:7–15, jan 2019.
- [229] El Hadi Saidane, Daniel Scida, Mustapha Assarar, and Rezak Ayad. Assessment of 3D moisture diffusion parameters on flax/epoxy composites. *Composites Part A: Applied Science and Manufacturing*, 80:53–60, jan 2016.
- [230] Z. N. Azwa, B. F. Yousif, A. C. Manalo, and W. Karunasena. A review on the degradability of polymeric composites based on natural fibres, may 2013.

Abstract

This dissertation presents insights into flax fiber-based thermoset composites from two standpoints; manufacturing the composites by resin transfer molding and their mechanical characterization. In particular, two thermoset matrices have been investigated, i.e. conventional epoxy and bio-based benzoxazine. The influence of the intrinsic properties of flax fibers such as variability, fiber swelling and liquid absorption on the manufacturing of composite parts is investigated. By considering fiber swell and liquid absorption, a mathematical model for the capillary rise of liquid in flax fibers is proposed. As classical tow permeability models cannot be adopted for flax fibers due to their irregularities in cross-section and fiber diameter, this study resorts to numerical simulations to statistically estimate the permeability. The influence of injection pressure during resin transfer molding on void content in flax/epoxy plates is characterized and modeled to understand the differences in void formation from glass fiber composites. The effect of cure cycle on the mechanical properties of composites is investigated by tensile tests of unidirectional flax composites to emphasize the evolution of the mechanical locking at fiber/matrix interface caused by resin penetration into elementary fibers with increase in processing temperature. Finally, the long-term behavior of composites is examined for flax/epoxy composites and flax/benzoxazine composites, by hygrothermal aging test.

Keywords: Composite materials, Natural fibers, Wettability, Permeability, Aging

Résumé

Cette thèse présente un aperçu des composites thermodurcissables à base de fibres de lin de deux points de vue: fabrication par moulage par injection de résine et caractérisation mécanique. En particulier, deux matrices thermodurcissables ont été étudiées, à savoir l'époxy classique et la benzoxazine biosourcée. L'influence des propriétés intrinsèques des fibres de lin tels que la variabilité, le gonflement de la fibre et de l'absorption de liquide sur la fabrication de pièces composites est étudiée. En considérant le gonflement des fibres et l'absorption des liquides, un modèle mathématique pour l'ascension capillaire des liquides dans les fibres de lin est proposé. Les modèles classiques de perméabilité ne pouvant être adoptés pour les fibres de lin en raison de leurs irrégularités de section et des diamètres de fibres, cette étude a recours à des simulations numériques pour estimer statistiquement la perméabilité. L'influence de la pression d'injection lors du moulage par transfert de résine sur la teneur en vides dans les plaques de lin/époxy est caractérisée et modélisée afin de comprendre les différences entre la formation de vides dans les composites renforcés par fibres de verre et fibres de lin. L'effet du cycle de polymérisation sur les propriétés mécaniques des composites est étudié par des tests de traction de composites de lin unidirectionnels afin de souligner l'évolution d'accroche mécanique à l'interface fibre/matrice provoquée par la pénétration de la résine dans les fibres élémentaires avec l'augmentation de la température de traitement. Enfin, le comportement à long terme des composites est examiné pour les composites lin/époxy et les composites lin/benzoxazine, par test de vieillissement hygrothermique.

Mots-clés: Matériaux composites, Fibres naturelles, Mouillabilité, Perméabilité, Vieillissement